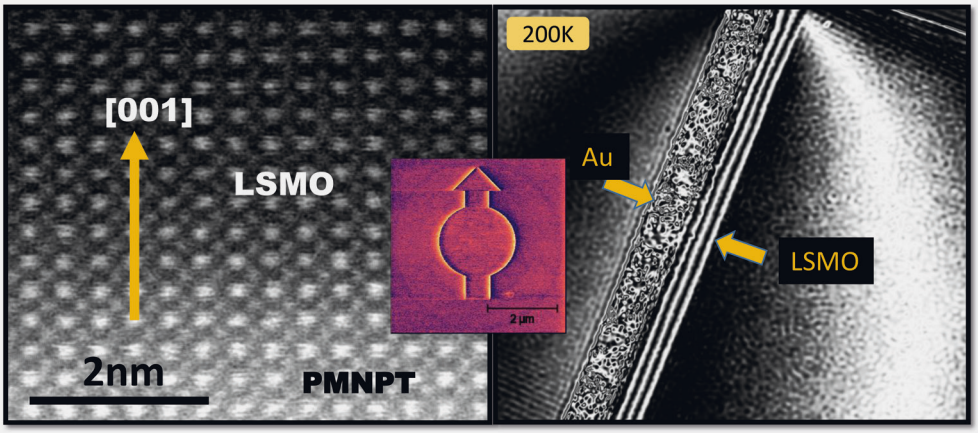

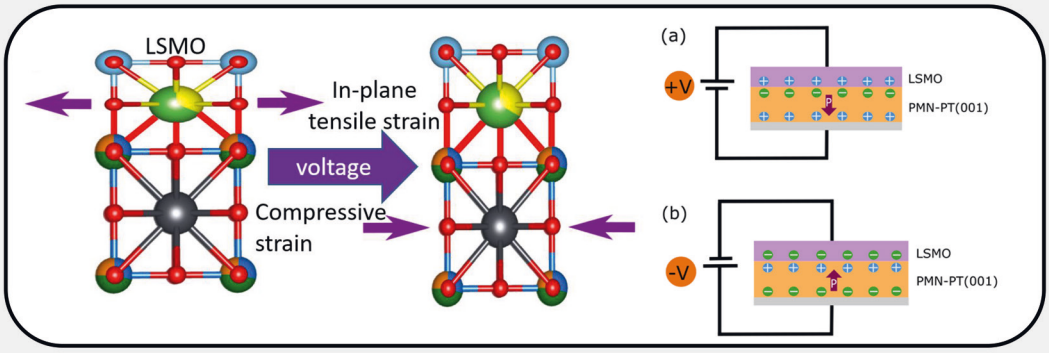

Resolving interface effects in voltage controlled magnetic heterostructures using advanced neutron scattering and electron microscopy methods

Tanvi Bhatnagar-Schöffmann

Schlüsseltechnologien / Key Technologies
Band / Volume 251
ISBN 978-3-95806-604-5

Mitglied der Helmholtz-Gemeinschaft

JÜLICH
Forschungszentrum

Schriften des Forschungszentrums Jülich
Reihe Schlüsseltechnologien / Key Technologies Band / Volume 251

Forschungszentrum Jülich GmbH
Jülich Centre for Neutron Science (JCNS)
Quantenmaterialien und kollektive Phänomene (JCNS-2/PGI-4)

Resolving interface effects in voltage controlled magnetic heterostructures using advanced neutron scattering and electron microscopy methods

Tanvi Bhatnagar-Schöffmann

Schriften des Forschungszentrums Jülich
Reihe Schlüsseltechnologien / Key Technologies Band / Volume 251

ISSN 1866-1807 ISBN 978-3-95806-604-5

Bibliografische Information der Deutschen Nationalbibliothek.
Die Deutsche Nationalbibliothek verzeichnet diese Publikation in der
Deutschen Nationalbibliografie; detaillierte Bibliografische Daten
sind im Internet über http://dnb.d-nb.de abrufbar.

Herausgeber und Vertrieb:	Forschungszentrum Jülich GmbH Zentralbibliothek, Verlag 52425 Jülich Tel.: +49 2461 61-5368 Fax: +49 2461 61-6103 zb-publikation@fz-juelich.de www.fz-juelich.de/zb
Umschlaggestaltung:	Grafische Medien, Forschungszentrum Jülich GmbH
Druck:	Grafische Medien, Forschungszentrum Jülich GmbH
Copyright:	Forschungszentrum Jülich 2021

Schriften des Forschungszentrums Jülich
Reihe Schlüsseltechnologien / Key Technologies, Band / Volume 251

D 82 (Diss. RWTH Aachen University, 2021)

ISSN 1866-1807
ISBN 978-3-95806-604-5

Vollständig frei verfügbar über das Publikationsportal des Forschungszentrums Jülich (JuSER)
unter www.fz-juelich.de/zb/openaccess.

Zusammenfassung

Einer der vielversprechensten Wege, um neuartige magnetische Datenspeicher und spintronische Geräte mit niedrigem Stromverbrauch zu entwickeln, ist die Manipulation von Magnetismus durch angelegte Spannung ("Voltage Control of Magentism", VCM). Eine Möglichkeit dies zu realisieren ist durch das Wachstum küntlicher multiferroischer Heterostrukturen mittels Oxidmolekularstrahlepitaxie. Die Heterotruktur in dieser Arbeit besteht aus einer ferromagnetischen $La_{0.7}Sr_{0.3}MnO_3$ (LSMO) Schicht und einem piezo-/ferroelektrischen Substrat $Pb(Mg_{1/3}Nb_{2/3})O_3$ - $PbTiO_3$ (PMN-PT). Die LSMO Schicht wird epitaktisch auf dem Substrat gewachsen. Diese Arbeit berichtet hauptsächlich darüber, wie die Art der magnetoelektrischen (ME) Kopplung in LSMO/PMN-PT(001) durch Veränderung von Temperatur und Magnetisierungsrichtung kontrolliert werden kann. In allen Messungen wird die Spannung entlang der [001]-Richtung angelegt. Die ME Kopplung wird duch zwei Effekte bedingt: Verspannung der Schicht durch den piezoelektrischen Effekt und Ladungskopplung durch die Änderung der ferroelektrischen Polarisierung des Subtrates. Der Einfluss beider Beiträge ist in allen Messungen sichtbar. Entlang der magnetischen harten Achse [100] der LSMO Schicht ist die Verspannung der Schicht hauptsächlich für die Kopplung verantwortlich, während entlang der magnetischen weichen Achse [110] die Ladungskopplung dominiert. Das durch polarisierte Neutronenreflektometrie (PNR) bestimmte magnetische Tiefenprofil mit angelegtem elektrischen Feld macht eine Zwischenschicht mit reduzierter nuklearer und magnetischer Streulängendichte sichtbar. Durch Rastertransmissionselektronenmikroskopie (STEM) und energiedispersive Röntgenspektroskopie (EDS) können ein Defizit von La und ein Überschuss von Mn sichtbar gemacht werden. Der Mn Überschuss bildet Ausscheidungen, mit einer im Schnittbild dreieckigen Strukturen, nahe des Substrat-Film Übergangs. Magnetisierungsmessungen der Proben zeigen einen Sprung der Magnetisierung nahe der Curie-Temperatur $T_C = 43\,K$ von Mn_3O_4. Dies zeigt, dass der Mn Überschuss als Ausscheidungen mit Mn_3O_4 Stöchiometrie wächst. Die in STEM sichtbaren Verspannung der LSMO Schicht in der Nähe des Substrates führt zu Defekten in der Kristallstruktur, welche das Wachstum der Mn_3O_4 Strukturen ermöglichen. Mit Hilfe von "off-axis" Elektronenholographie kann das Magnetfeld innerhalb der Proben in Abhängigkeit der Temperatur aufgelöst werden. Das Magnetfeld innerhalb der LSMO Schicht ist homogen und, da der magnetische Phasengradient mit zunehmender Temperatur abnimmt, nimmt auch das Magnetfeld innerhalb der Schicht ab.

Eine zweite Heterostruktur, $La_{0.7}Sr_{0.3}MnO_3$/ $BaTiO_3$/ Nb:$SrTiO_3$ (LSMO/BTO/Nb:STO (001)) wird durch eine Kombination von Molekularstrahlepitaxie und Hochdrucksputtern gewachsen. In diesem System ist LSMO weiterhin die ferromagnetische Schicht, BTO die ferroelektrische Schicht, und Nb:STO ein elek-

trisch leitendes Substrat. Die Wachstumsparameter für die BTO Schicht sind durch eine Wachstumsstudie optimiert. Die Heterostruktur zeigt hohe Kristalinität und gute magnetische und ferroelektrische Eigenschaften. In beiden Systemen ist die Remanenz der LSMO Schicht negativ.

Abstract

Voltage control of magnetism (VCM) shows a strong potential to impact the field of magnetic data storage and spintronic devices with low power consumption. With this as an aim, $La_{0.7}Sr_{0.3}MnO_3$/$Pb(Mg_{1/3}Nb_{2/3})O_3$ - $PbTiO_3$ (LSMO/PMN-PT (001)) heterostructure is deposited using oxide molecular beam epitaxy. LSMO is ferromagnetic at room temperature. Grown on a piezoelectric /ferroelectric substrate PMN-PT(001), it forms an *artificial multiferroic heterostructure*. This system was structurally characterized using different techniques revealing growth of epitaxial LSMO layers. The main part of this thesis focuses on the investigation of magnetoelectric coupling in LSMO/PMN-PT(001). The measurements show change in the nature of ME coupling, by varying different parameters like temperature and direction of magnetization. In all experiments the voltage is applied along [001] direction. The magnetoelectric coupling in LSMO/PMN-PT(001) arises due to strain and charge coupling. Since the substrate PMN-PT is piezoelectric and ferroelectric, both strain effect and switching of ferroelectric polarizations contribute to the ME coupling. Impact of both mechanism is visible in the measurements. Strain coupling is dominant along hard axis [100] of LSMO whereas charge coupling shows dominance along easy axis [110] of LSMO. Using polarized neutron reflectometry (PNR), the magnetic depth profile as a function of applied voltage reveals the presence of an interlayer with reduced nuclear scattering length density and magnetic scattering length density. Examining this interlayer with scanning transmission electron microscopy (STEM) and energy dispersive X-ray spectroscopy (EDS) shows La-deficiency and excess of Mn near the interface with the dark regions to be particles with a triangular cross-section. The stoichiometry of these particles is confirmed with field cooled-cooling (FCC) curve which shows a jump in magnetization near the Curie temperature $T_C = 43\,K$ of Mn_3O_4. The formation of these particles is favored when the LSMO films are strongly strained which leads to defects near the interface. STEM images shows the presence of defects near the interface. Real-space magnetic field mapping as a function of temperature is performed using off-axis electron holography on LSMO/PMN-PT(001) which demonstrates uniform magnetic field in the LSMO films. The magnetic phase gradient reduces with increasing temperature depicting reduction in the magnetic field in LSMO layer with temperature. Based on similar approach, a second heterostructure, $La_{0.7}Sr_{0.3}MnO_3$/ $BaTiO_3$/ Nb:$SrTiO_3$ (LSMO/BTO/Nb:STO (001)) is deposited using high oxygen pressure sputtering system and oxide molecular beam epitaxy. Here, LSMO is a ferromagnetic component, BTO layer is ferroelectric and Nb:STO is used a conductive substrate. The growth of this structure is a two-step process. The BTO layer is grown in the high oxygen pressure sputtering system using growth parameters optimized during a growth study. The LSMO layer is grown in the oxide molecular beam epitaxy system. This heterostructure shows good crystalline, magnetic, and ferroelectric

properties. In both systems, negative remanence is observed in the LSMO layer.

Table of contents

1 Introduction

The quest for high data storage density has pushed the semiconductor industry to find a new route to create energy efficient data storage devices. With this focus, the current spintronic devices have already delivered non-volatile magnetic random access memory (MRAM) [1]. These spintronic devices rely on ferromagnetic (FM) materials, where the magnetic moment is controlled by application of external magnetic field. The generation of the external magnetic field is costly in terms of power consumption and dissipation. These problems can be avoided by using multiferroic materials. Multiferroics are the material possessing coexistence of more than one ferroic order. A multiferroic possessing FM and ferroelectric (FE) orders enable the control the magnetization by an electric field, which is called magnetoelectic (ME) effect [2, 3]. The FE part of the envisaged material would guarantee the prevention of electric currents due its insulating nature, thereby decreasing the power consumption.

ME coupling has been demonstrated in single phase oxide materials [4, 5]. However, the single phase materials like Cr_2O_3 or $TbMnO_3$, are antiferromagnetic (AFM) in nature and exhibit large effects only below room temperature, which cannot be used for the device application. This makes the composite materials an interesting alternative to single phase materials. In a composite material, it is possible to combine FM and FE materials, creating an artificial multiferroic heterostucture, exhibiting multiferroic properties at room temperature or even higher. In such composite systems the ME coupling is strongly mediated via the interface between the materials and different mechanisms can be responsible for the coupling [6]. Thus, it becomes crucial to study the interface properties of such composite systems.

Transition metal oxides (TMO) are promising candidates as they display strong couplings between lattice, charge, spin and orbital degrees of freedom. Also, oxide thin films exhibit large screening length, thereby guaranteeing a strong electric field effect for voltage control of magnetism (VCM) [7]. Complex oxides with AMO_3 perovskite structure, where M is a 3d-transition metal, provide a fertile ground for many novel applications due to the nature of their electronic states arising from M-O-M hybridization and their bonding geometries [8]. Such complex magnetic oxides exhibit good coherence with FE oxides like $BaTiO_3$ (BTO), $Pb(Mg_{1/3}Nb_{2/3})O_3$ - $PbTiO_3$ (PMN-PT) and $Pb(Zr_{0.2}Ti_{0.8})O_3$ (PZT) with respect to crystal structure. Thus, it becomes possible to produce epitaxial FM/FE heterostructures [9]. There are different mechanisms involved in VCM based on the choice of magnetic and dielectric materials. Common mechanisms include: **Carrier Modulation** where the magnetic properties vary due to change in the carrier doping level as a function of applied voltage. This is known as charge-mediated ME coupling. **Strain coupling**

arises from transfer of strain from the FE layer/substrate to the FM layer due to the change in lattice or shape of FE component through an inverse piezoelectric effect, resulting in significant modulation in magnetic properties. **Exchange coupling** or exchange bias effect commonly observed in FM/AFM interfaces, reflected by the shift of magnetization hysteresis curve away from origin. This coupling can be manipulated via external voltage, thereby modulating magnetic performance. **Orbital reconstruction** results from the charge transfer and orbital hybridization occurring at the interface of FM/FE oxides. This can induce an interfacial covalent bond leading to series of novel electronic states and phenomena.

The work of this thesis studies represents mediation of ME coupling via carrier modulation and strain coupling. Two FM/FE composites have been studied : $La_{0.7}Sr_{0.3}MnO_3$ (LSMO)/PMN-PT(001) and LSMO/BTO/Nb:$SrTiO_3$ (001). The first heterostructure LSMO/PMN-PT(001) is grown using oxide molecular beam epitaxy (OMBE). Temperature dependent studies show dominance of strain-mediated ME coupling at 300 K and 80 K. However, the strain coupling behavior changes from butterfly loop at 300 K to linear at 80 K. On measuring the ME coupling in remanent magnetic field and along hard [100] and easy [110] axis of LSMO, strain coupling is found to be dominant along hard axis while charge coupling becomes dominant along the easy axis of LSMO at 300 K. A polarization hysteresis like loop is observed along easy axis. The magnetic depth profile is probed using polarized neutron reflectometry (PNR) as a function of voltage at 80 K which revealed presence of interlayer. This interlayer is examined by scanning transmission electron microscopy (STEM) and energy dispersive X-ray spectroscopy (EDS), which confirmed the excess of La-deficiency and Mn-excess near the interface. STEM results shows presence of Mn_3O_4 particles, the stoichiometry of which is confirmed by field cooled-cooling (FCC) curve which shows kink in magnetization near the $T_C = 43$ K of Mn_3O_4. Off-axis electron holography is performed on LSMO/PMN-PT(001) to study its remanent magnetization as a function of temperature which reveals presence of homogeneous magnetic field through LSMO. The second heterostructure, LSMO/BTO/Nb:STO(001) is deposited in two steps. First the growth parameters are calibrated to deposit FE BTO thin films in high oxygen pressure sputtering system (HOPSS). FE properties are probed using piezo force microscopy (PFM). After growing BTO layer, the sample is transferred to OMBE chamber for the deposition of LSMO. This heterostructure is checked for its structural, magnetic and FE properties which shows successful results. An interesting phenomena of negative remanence (NRM) is observed in LSMO layer for both systems, which requires a systematic study to understand its origin. These experiments and results give a comprehensive picture of VCM in LSMO/PMN-PT(001). With the successful growth of LSMO/BTO/Nb:STO(001), it is now possible to test this structure for ME coupling.

2 Theory

2.1 Strongly correlated electronic materials

Strongly correlated electronic (SCE) materials are the systems which show emergent phenomenona [10] arising due to correlation among different degrees of freedoms. The interactions between electronic spins, charges, orbitals and the lattice can produce novel functionalities, which are not characteristic of the individual elements but of the whole system [3]. Some of the typical examples of interesting emergent phenomena arising from SCE materials are high temperature superconductivity [11], colossal magnetoresistance [12], magnetocaloric effect [13], multiferroic effect [14], Metal-Insulator-Transitions (MIT) [15] and negative thermal expansion [16]. The SCE materials are found in perovskite structure containing a transition-metal ion inside an oxygen octahedral cage. The strong correlation between electrons produce a rich phase diagram which can be controlled by two fundamental parameters. Firstly, the hopping amplitude 't' which is responsible for the electron-hopping between the atoms and second is the density of charge carries [17]. These two parameters determine whether the system is ferromagnetic, antiferromagnetic, conducting or insulating. These parameters play an important role in complex oxides with the formula

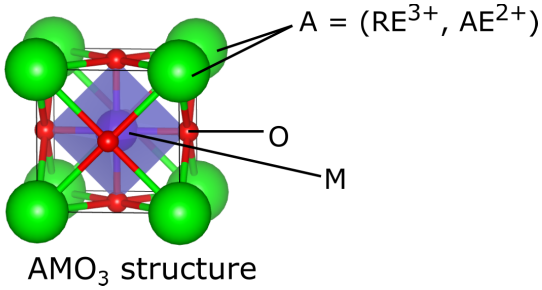

Figure 2.1: Ideal perovskite structure with formula AMO_3 inspired from [3] with Vesta [18]

of (RE,AE)MO_3 where RE is trivalent rare-earth ion, AE is divalent alkaline-earth ion and M is the transition metal ion. Fig. 2.1 shows ideal perovskite with simple cubic structure.

The A-site of the perovskite can be doped with electrons or holes in the form of solid solution ($RE_{1-x}AE_xMO_3$) thereby governing the increase or decrease in the density of charge carriers. Depending upon the amount of doping, the electron bandwidth W and the electronic concentration varies resulting in different phases of the system.

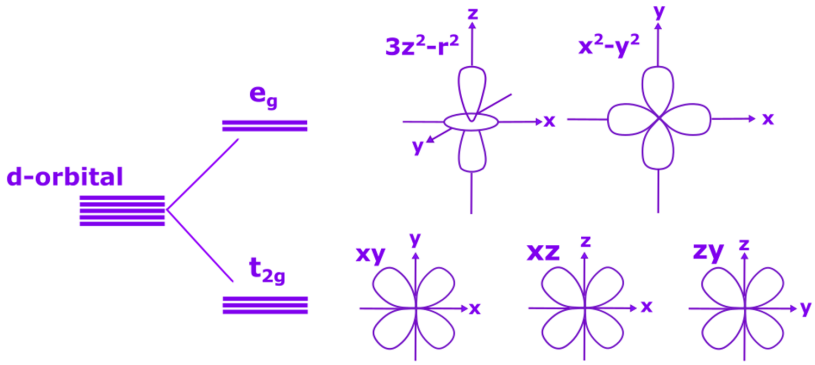

Figure 2.2: Crystal field splitting of d-orbitals in octahedral environment

These phases show interesting properties when subjected to a magnetic field, electric field or change of temperature. Since the transition-metal ion M is surrounded by negative oxygen ions O^{2-}, crystal field potential is created which lifts the degeneracy of the d-electron levels.

As one can see from the Fig.2.2, the e_g orbitals pointing towards O^{2-} have higher energy than t_{2g} orbitals which are pointing between the ions [3]. The crystal field effects arises due to the electrostatic repulsion from negatively charged electrons in the oxygen orbitals [19]. A variety of complex spin-orbital ordering can be achieved with the coupling of these degrees of freedom.

2.2 Ferroelectricity - $BaTiO_3$

A ferroelectric system is a non-centrosymmetric crystal structure possessing two or more switchable states of electric polarization in the absence of applied electric field [20]. They are insulating and dielectric in nature [21]. The onset of ferroelectricity in a material is due to the displacement of cations relative to the anions which results in polarization and this depends on the balance between long-range Coulomb forces which favors the ferroelectric state and short range repulsion caused by the electron clouds of the neighboring ions [22]. Cochran [23] and Anderson [24] could explain that the phase transitions and the lattice dynamical instability in ferroelectrics are based on soft mode theory. One can apply mechanical force or change the temperature causing distortion in crystal lattice which changes the strength of electric dipoles [25]. An electric dipole is made of two charges with opposite signs separated by a distance d and hence, a dipole moment can be defined as

$$\vec{p} \equiv q\vec{d} \tag{2.1}$$

A dipole vector always points parallel to distance from negative to positive charge as shown in Fig. 2.3.

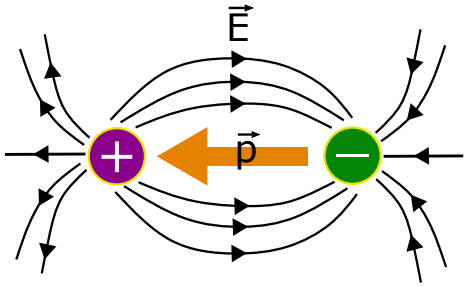

Figure 2.3: Electric dipole moment with separation of opposite charges and the electric field arising from the charges inspired from [26]

The primary characteristic of a ferroelectric material is ferroelectric hysteresis. Fig. 2.4 shows hysteresis loop of polarization versus electric field. On applying an electric field, the dipole moments start aligning themselves in the direction of applied field and the average polarization of the crystal starts increasing. At some point, the polarization reaches the saturation point due to the relative permittivity of the material and the extrapolation of this line to the abscissa gives saturation spontaneous polarization(P_S). Once reaching P_S, on reducing the electric field to zero, remanent polarization(P_R) is obtained, which is basically the polarization strength of the material retained after removal of electric field. A negative electric field is required to reduce the polarization to zero and this field is called Coercive field(E_C) and further increase in this negative field eventually reverses the saturation polarization to -P_S. When the field returns to zero, the polarization of the crystal is set to -P_R. In this way, one can again increase the electric field and switch the polarization to +P_R.

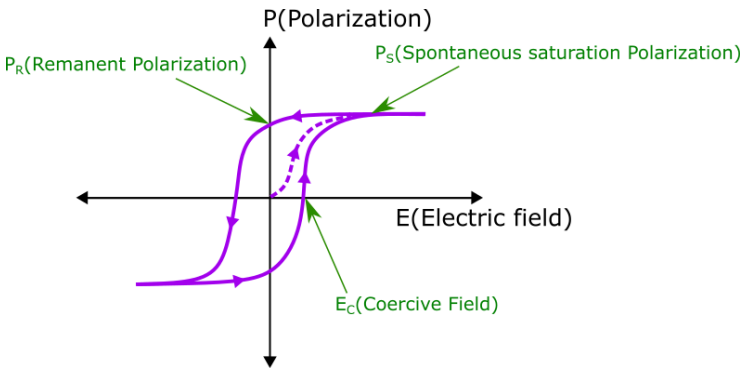

Figure 2.4: Ferroelectric hysteresis loop

Any crystal with a polar space group can possess a non-zero spontaneous polarization but for it to be ferroelectric, it is of utmost importance to have switchable states of electric polarization [20]. $BaTiO_3$ was the first perovskite compound found to be ferroelectric with tetragonal phase(P4mm) at 393 K. At 278 K the second ferroelectric phase transition takes place with orthorhombic symmetry(Amm2), followed by low temperature ferroelectric phase transition to rhombohedral(R3m) at 183 K.

Above 393 K, $BaTiO_3$ is in paraelectric cubic structure($Pm\bar{3}m$). Each transition is accompanied by atomic displacement of Ti^{4+} ion relative to O^{2-} octahedra along the $< 100 >$(T), $< 110 >$(O) and $< 111 >$(R) directions [20]. As the displacement of ions takes place, a double well structure is obtained in the energy which depends on the ferroelectric distortion amplitude in the system. In BTO, the long range dipole-dipole interaction causes the Ti^{4+} to deviate from its equilibrium position. For this ferroelectric distortion, the empty 3d-orbitals of Ti^{4+} ion hybridize with filled 2p-orbitals of O^{2-} making strong covalent bond and the Ba^{2+}-O^{2-} make ionic bond [27]. The hybridization between the two orbitals is strongly dependent on their energy difference and with ferroelectricity taking place, the respective participating orbitals are shifted.

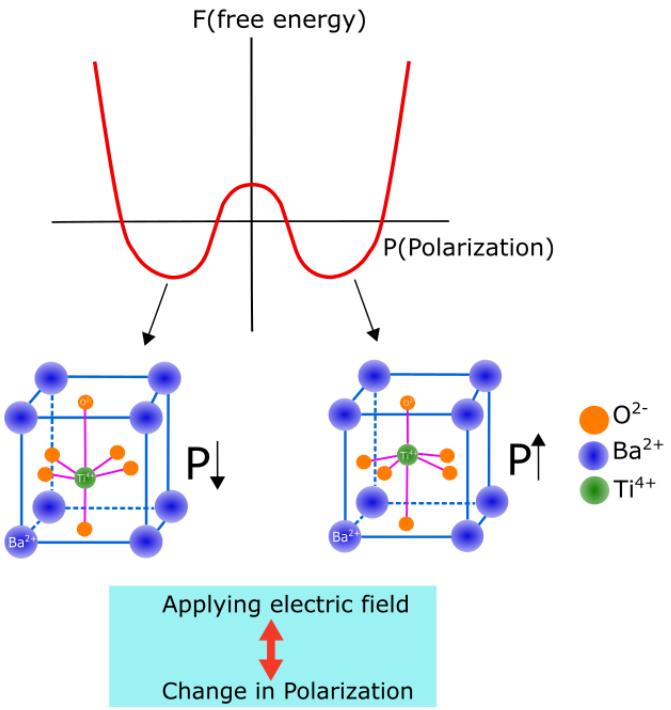

Figure 2.5: Change in polarization in $BaTiO_3$ on application of applied electric field with double well potential model for ferroelectric polarization

$BaTiO_3$ in cubic phase has lattice parameter of 4.01 Å with the measured polarizations of $33\mu C/cm^2$ for R-phase, $36\mu C/cm^2$ for O-phase and $27\mu C/cm^2$ for T-phase [28]. It experiences displacive type phase transition due to softening of phonons [23] and at low temperatures, near phase transition, the frequency of these soft phonons tend to become zero. $BaTiO_3$ in tetragonal phase can have two types of ferroelectric domains: a-type(90°) and c-type(180°). The domains oriented along a-axis(in-plane) of BTO are called a-type domains and domains oriented along c-axis(out-of-plane) are known as c-type domains.

2.3 Piezoelectricity and Relaxor Ferroelectrics (RFE)-PMNPT

Another effect which is observed in ferroelectric systems is 'piezoelectricity'. All ferroelectrics are piezoelectrics(PE) but not all piezoelectrics are ferroelectrics. When a crystal is subjected to some mechanical stress, an electric potential is developed across the crystal with accumulation of charges at its surfaces, known as 'direct piezoelectric effect'. On the otherhand, on applying voltage across a piezoelectric crystal, the crystal undergoes some deformation which is called 'inverse piezoelectric effect'. What is actually happening in a crystal is that, in an equilibrium state the electrical charges are perfectly balanced in the crystal and on application of mechanical stress or electrical pressure, some atoms are pushed together and some are pushed apart which changes the balance of electrical charges creating electric dipoles which do not cancel each other. As a result, positive and negative charges appear on the surfaces of a crystal [29]. This brings us to another class of ferroelectrics known as 'Relaxor Ferroelectrics (RFE)'. RFE are disordered ferroelectrics and exhibit high electrostriction, a ferroelectric response under high electric fields at low temperature and dielectric relaxation [30]. They are characterized by three temperatures: Burns temperature T_B at which polar nanoregions start appearing, intermediate temperature T_{im} when polar nanoregions become stable and permanent and T_C which is cubic to tetragonal phase transition [31]. The temperature dependence of permittivity of RFE follows a special quadratic law

$$1/\varepsilon \propto (T - T_0)^2 \tag{2.2}$$

Whereas the normal ferroelectrics follow Curie-Weiss law and T_0 is Curie-Weiss temperature,

$$1/\varepsilon \propto (T - T_0) \tag{2.3}$$

A typical example of RFE is $Pb(Mg_{1/3}Nb_{2/3})O_3$ (PMN) [32] in which B-site is shared by 2 cations: Mg^{2+} and Nb^{5+} making it A(B'B")O_3 structure. It exhibits excellent piezoelectric properties and possesses perovskite structure with cubic symmetry which is retained down to 5 K. On applying an electric field to such a crystal, the B-ions can displace easily without causing any distortion to the oxygen framework as described by 'rattling ion model'. Therefore, larger polarization can be expected for such systems [30]. Also, RFE's are known to have diffused phase transitions. At higher temperatures they exhibit paraelectric behaviour. It features nanoscale ordering of Mg^{2+} and Nb^{5+} ions. The local electric dipoles in PMN emerge as a result of offset arrangement of polarizable Pb and Nb cations from their centrosymmetric positions within the oxygen octahedra while Mg remains approximately central. But on average, all the cations maintain cubic symmetry. The displacement correlations in PMN are referred as polar nano-regions which are in nanometer size and are formed below Burns temperature $T_B = 620$ K. These polar nanoregions possess nonzero spontaneous polarization [33]. The displacement of both Pb and Nb takes place along $\langle 111 \rangle$ and the magnitude of Pb displacement enhances as the local Mg/Nb ratio increases. These polar nanoregions are the reason behind the relaxor behavior

of PMN.On reducing the temperature, the size of polar nanoregions increases and at freezing temperature $T_f = 230\,K$, they become frozen, which results in remarkable ferroelectricity and high remanent polarization at low temperatures [34]. These local polar nanoregions possess rhombohedral R3m symmetry. Pb^{2+} and Nb^{5+} cations form short but strong covalent bonds with oxygen via hybridization of their 6s and 4d states with O 2p states whereas due to lower ionic charge of Mg^{2+}, it is less covalently bonded with oxygen which leads to underbonded oxygen atoms. In order to satisfy the oxygen bonding requirements, larger Pb off-centering is needed [33]. Fig.2.6(a) shows the cation ordering in PMN with arrangement of alternating {111} planes occupied by Nb^{5+} and a 2:1 mix of Mg^{2+}/Nb^{5+}. Eremenko *et* al., reported in

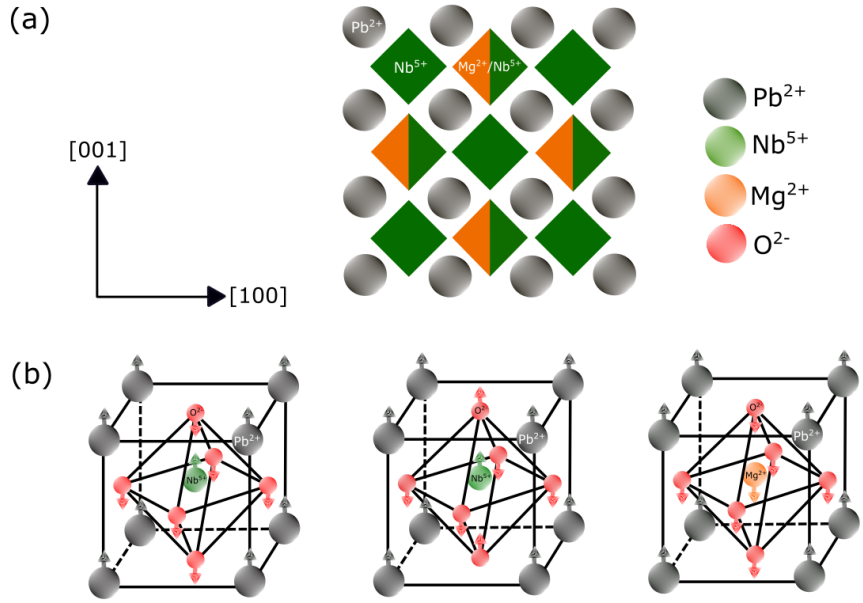

Figure 2.6: (a) chemical ordering in PMN, **(b)** cation-oxygen displacement modes (inspired from [33])

their paper that based on PDF analysis, Pb has stronger off-centering from Mg than from Nb and both Pb and Nb are displaced along ⟨111⟩ direction. Fig.2.6(b) demonstrates the displacement of cations with respect to oxygen. The Pb displacement is negative correlated with oxygen meaning: it moves opposite to oxygen which is similar to Nb displacement whereas, for Mg the displacement is positively correlated with oxygen. It was observed that on substitution of Ti^{4+} ions for Mg^{2+}/Nb^{5+} at B-site, the relaxor properties of PMN can be reduced in (1-x)PMN-(x)PT [35] and the Curie temperature can be increased above room temperature. With the substitution of $PbTiO_3$ (PT), a ferroelectric phase near morphotropic phase boundary (MPB - transition between the tetragonal and rhombohedral ferroelectric phases due to compositional variation) at $x \approx 0.33$ appears which separates the relaxor side (pseudocubic) and ferroelectric side (tetragonal) of the solid solution. The substitution of PT deteriorates the stability of the local rhombohedral symmetry in PMN. As a result, the system stays pseudocubic on average. The transition temperatures

for PMN and PT are 258 K and 763 K. In this thesis, 0.7PMN-0.3PT is used where PT substitution is near MPB. It was observed that at x = 0.3, with the increase in temperature the spontaneous polarization decreases but does not vanish completely which means that near the transition temperature the ferroelectric and paraelectric phase co-exist in micro-regions. Such a behavior is very typical for RFEs [36]. The black line in fig.2.7 represents lattice parameters as a function of temperature

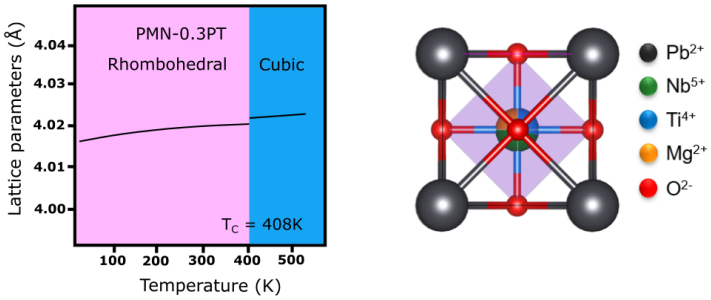

Figure 2.7: Phase diagram of PMN-0.3PT with lattice parameters as a function of temperature with T_C = 408 K inspired from [37] and crystal structure of PMN-0.3PT with Vesta [18].

for PMN-0.3PT. At 300 K PMN-0.3PT is rhombohedral with pseudocubic structure having $\alpha = \beta = \gamma$ =89.90°. It has lattice constant of a=4.02Å. PMN-0.3PT possesses 3 types of domain switching: 71°, 109° (ferroelastic) and 180° (ferroelectric) with 8 polarization orientations in ⟨111⟩ direction.

$$P^{total} = P_r^{Ti} x^{PT} + P_r^{PMN} x^{PMN}, \tag{2.4}$$

The equation 2.4 demostrates that the total polarization of PMN-PT is a sum of polarization arising from both phases P_r^{PMN} and P_r^{Ti} [34]. In PMN-PT, not only the B-sites are shifted but also the A-site is off-centered. This is due to the formation of strong covalent bond between Pb-O. Therefore, on application of electric field the cations on B-site and the O anions are displaced in same direction opposite to the electric field [38].

2.4 Ferromagnetism in $La_{0.7}Sr_{0.3}MnO_3$

In section 1.1, interesting emergent phenomenas were discussed arising from strongly correlated electronic (SCE) materials and one of them was colossal magnetoresistance (CMR). This section will talk about the SCE material $La_{0.7}Sr_{0.3}MnO_3$ (LSMO) which exhibits CMR. LSMO is derived from its parent system $LaMnO_3$ (LMO) which is an insulating antiferromagnet [39] whereas LSMO is an semi-metallic ferromagnet. The reason behind this change of magnetic ordering is the different kind of exchange interactions taking place for both systems. These exchange interactions arise due to overlapping of two or more electron wave functions resulting in anti-symmetric

wave function. One can describe the exchange interaction by a Heisenberg-Spin-Hamiltonian as

$$\hat{H} = -\sum_{ij} J_{ij}\vec{S_i} \cdot \vec{S_j}, \tag{2.5}$$

where $\vec{S_i}$ and $\vec{S_j}$ are quantum mechanical spin operators, J_{ij} is the exchange constant between the i^{th} and j^{th} spins [19]. If $J_{ij}<0$, antiferromagnetic alignment and for $J_{ij}>0$, a ferromagnetic alignment is favoured.In LMO, the antiferromagnetic ordering is due to superexchange interaction between the Mn^{3+} ions.

2.4.1 Superexchange Interaction

It is an indirect exchange interaction mediated via non-magnetic ion placed between magnetic ions. This type of kinetic exchange allows delocalization of electrons by minimizing the kinetic energy of the system. The superexchange interaction is a virtual hopping process derived from second-order perturbation theory. It is best explained by Goodenough-Kanamori [40] rules which states that the occupation of the metal orbitals and the angle between the metal atoms and the mediating oxygen atom are very crucial for magnetic superexchange. A virtual transfer between two half-filled metal orbitals with the metal atoms and oxygen atoms M-O-M having an angle of 180° is restricted by Pauli exclusion principle and therefore antiferromagnetic ordering is obtained. However, if exchange takes place between filled and empty metal orbitals with M-O-M of 180° and with M-O-M of 90° angle between filled metal orbitals, a ferromagnetic ordering is obtained.

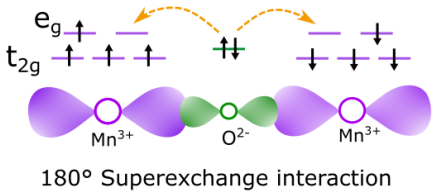

Figure 2.8: Superexchange interaction taking place in M-O-M which favours antiferromagnetic ordering

2.4.2 Crystal Field Splitting and J-T distortion

On doping LMO with Sr (x = 0.3), the A-site becomes a mixture of divalent (Sr^{2+}) and trivalent (La^{3+}) cations which leads to mixed valence of manganese ions: Mn^{3+} - $[Ar]3d^4$ and Mn^{4+} - $[Ar]3d^3$ [10]. There is a crucial parameter which is responsible for the structure of manganites known as tolerance factor t,

$$t = \frac{(r_A + r_O)}{\sqrt{2}(r_B + r_O)}, \tag{2.6}$$

The perovskite structures are stable for the range of 0.89<t<1.02, t =1 for an ideal cubic structure [12]. Due to the misfit between the ionic radii of the A (r_A) and B (r_B) ions, the corner shared oxygen octahedras are tilted leading to sizable distortions. Hence, rhombohedral or orthorhombic structure is obtained [10]. For manganites, the central Mn ion is surrounded by the oxygen octahedra which leads to crystal field splitting.

The electrostatic repulsion from the negatively charged electrons in the oxygen orbitals give rise to the crystal field [19]. Atomic physics tells us that a homogeneous electric field changes the energy levels of an atom, also known as the 'Stark effect'. Therefore, one can consider the crystal field theory (CFT) as a generalization of Stark effect for anisotropic charge distributions. The degeneracy of 2J+1 ground state levels in the atoms with unpaired electrons is lifted due to an interaction with anisotropic charge distribution. Thus, this crystal field splitting will result in an anisotropy for the local spin orientation because of spin-orbit interaction [10]. The electronegativity of oxygen atoms surrounding a metal ion pulls the charge away from the metal atom towards the oxygen atoms making the metal-oxygen bond partly covalent and partly ionic. In manganites, the octahedral surrounding of oxygen atoms around Mn ions lead to crystal field splitting. The 3d-orbitals $d_{3z^2-r^2}$ and $d_{x^2-y^2}$ point in the direction of negative point charges whereas the orbitals d_{zx}, d_{yz} and d_{xy} point in between the negative point charges. Thus, a 3d electron in orbitals d_{xz}, d_{yz} and d_{xy} experience a weaker Coulomb repulsion from the oxygen atoms. Therefore, a former five fold degenerate energy level splits into t_{2g} level with three fold and e_g level with two fold degeneracy. The lower t_{2g} level comprises of d_{xz}, d_{yz} and d_{xy} orbitals and the upper level e_g has $d_{3z^2-r^2}$ and $d_{x^2-y^2}$ orbitals as depicted in fig. 2.9.

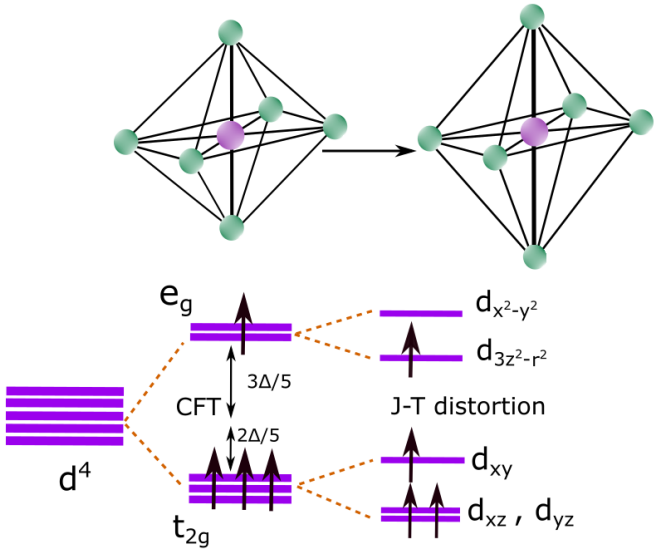

Figure 2.9: Crystal field splitting in a $3d^4$ ion in an octahedral. The 3d states split into lower t_{2g} level and upper e_g level. The Jahn-Teller effect lifts this orbital degeneracy by distorting the crystal lattice.

In MnO_6 octahedron, the lowest t_{2g} level and the highest e_g level have energy difference of $\Delta \sim 1.5\,\text{eV}$ and with Hund's first rule, the intra-atomic correlations favours parallel alignment of the electron spins for Mn^{3+} and Mn^{4+} ions. The corresponding exchange energy is about 2.5 eV and larger than the crystal field splitting yielding a weak field case with electron occupancy in Mn^{3+}: $t_{2g}^{3\uparrow}\, e_g^{\uparrow}$, S = 2 and Mn^{4+}: $t_{2g}^{3\uparrow}$, S = $\frac{3}{2}$ [12].

Another effect which is observed in LSMO depends on its magnetic properties which also influence the symmetry of local environment. This happens because sometimes a spontaneous distortion of the octahedron is energetically favorable as it balances the energy cost of increased elastic energy. This effect is known as **Jahn-Teller(J-T) distortion** [19]. This effect is evident in Mn^{3+} ions lowering its energy whereas Mn^{4+} does not show this effect. J-T distortion results in raising and lowering of energy of certain orbitals as shown in fig. 2.9.

2.4.3 Double exchange interaction

As discussed earlier that Sr-doping in LMO leads to mixed valence of Mn ions with different oxidation states: $Mn^{3+}[3d^4]$ and $Mn^{4+}[3d^3]$ and due to this the exchange interaction among these Mn ions result in ferromagnetic ordering. This type of exchange interaction is known as **double exchange interaction**. In double exchange (DE) interaction, a simultaneous electron hopping takes place: an e_g electron from Mn^{3+} hops into oxygen 2p orbital and at the same time a 2p electron of oxygen

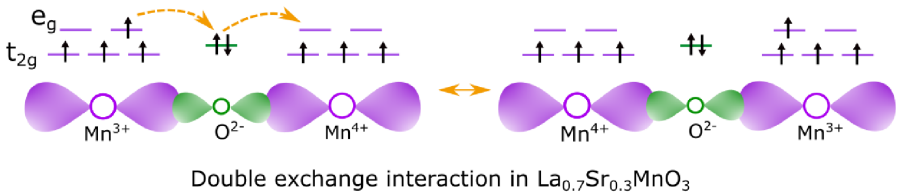

Figure 2.10: Double exchange interaction resulting in FM alignment in LSMO

hops onto Mn^{4+} site. This electron hopping is only possible if there is a vacancy of the same spin, since spin-flip of hopping electron is not allowed and if the electrons in t_{2g} level have parallel alignment. The hopping of e_g electron to a neighboring ion with anti-parallel alignment of t_{2g} spins is not energetically favorable. The ferromagnetic alignment arising from this electron hopping reduces the overall energy of the system and is also responsible for the conductivity on the material. Hence, the material becomes metallic [10, 19]. The Sr-doping at A-site generates holes on the

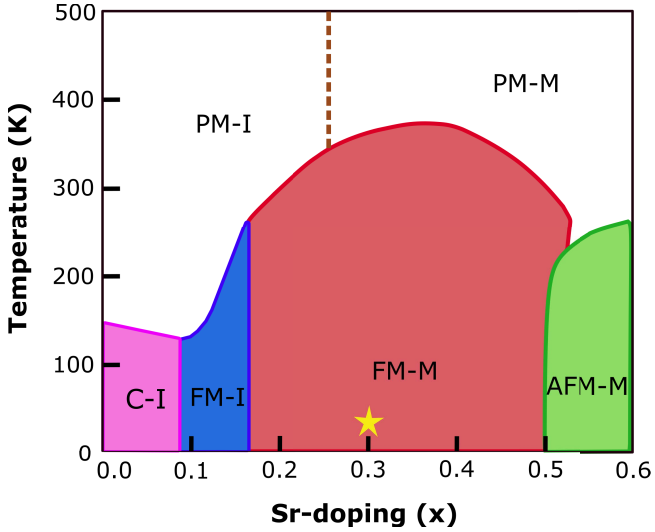

Figure 2.11: LSMO phase diagram with Sr-doping levels (Inspired by [41]). It comprises of various magnetic phases: C-I (spin-canted insulator), FM-I (ferromagnetic insulator), FM-M (ferromagnetic metal), AFM-M (antiferromagnetic metal), PM-I (paramagnetic insulator) and PM-M (paramagnetic metal). The yellow star indicates the Sr-doping used in this thesis work.

Mn-sites as seen above. This yields in a fraction of (1-x)Mn^{3+} ions and (x)Mn^{4+} ions. The t_{2g} electrons in Mn^{3+} ions are tightly bound whereas the e_g electron is itinerant which results in DE interaction. Therefore, on application of magnetic field, the core spins align thereby increasing the conductivity near $T_C = 370\,K$ for LSMO. Also, near T_C, LSMO shows a large magnetoresistive effect known as colossal magnetoresistance (CMR) which is an implication of metal-insulator transition

(MIT). Above T_C, the system is in paramagnetic state and the spin directions of t_{2g} electrons in the neighboring ions fluctuate, thereby suppressing the electron hopping and making the system insulating [19].

LSMO properties strongly depend on the Sr-doping level x at the A-site as it also leads to variation in Mn^{3+}/Mn^{4+} ratio which is responsible for magnetic ordering and the conduction of electrons. From Fig.2.11, one can infer the changes in the phases of LSMO with increasing Sr-doping (x). In this work, we are using LSMO with x=0.3 which is in FM-M state (marked with star).

2.5 Magnetoelectric effect

Magnetoelectric effect is defined as coupling between magnetization and electric polarization i.e., controlling magnetization by switching electric polarization or vice-versa. It is already known from Maxwell's equation that magnetic interaction and electric charge motion are intrinsically coupled. In 1960, Dzyaloshinskii [4] proposed that the occurrence of magnetoelectric effect is strongly dependent on the magnetic symmetry of the substance and predicted the magnetoelectric coupling in Cr_2O_3, which was later experimentally proven by Astrov [42,43]. However, the experimental proof of magnetoelectric(ME) effect in Cr_2O_3 showed presence of linear ME effect which is intrinsically small. Magnetoelectric coupling can be thermodynamically explained by expansion of free energy as a function of electric and magnetic fields [14]

$$F(E,H) = F_0 + \varepsilon E^2 + \mu H^2 - EP - MH - \alpha EH - \beta EH^2 - \delta E^2 H - \gamma E^2 H^2 + ... \quad (2.7)$$

The two most studied magnetoelectric couplings are bilinear coupling 'αEH', responsible for small ME coupling in Cr_2O_3, and biquadratic coupling '$\gamma E^2 H^2$' which can lead to bigger ME effects. Now, differentiating equation 2.7 with respect to electric field gives polarization

$$P(E,H) = \alpha H + \beta H^2 + 2\delta EH + 2\gamma EH^2 + ... \quad (2.8)$$

and magnetization by differentiating with respect to magnetic field

$$M(E,H) = \alpha E + 2\beta EH + \delta E^2 + 2\gamma E^2 H + ... \quad (2.9)$$

Then came new and interesting set of materials known as multiferroics where two or more ferroic orders are present. Multiferroics gave a whole new platform for studying ME coupling. Consider a multiferroic possessing a bilinearly coupled polarization P and magnetization M. In order, to achieve ME effect, the space inversion symmetry (due to dielectric polarization) and time inversion symmetry (due to magnetization) has to be broken simultaneously. This can be realized by Dzyaloshinskii-Moriya effect [4, 44] which arises due to an energy contribution to the Hamiltonian of a

crystal where the antiferromagnetically aligned spins can be canted and the amount of this spin canting is directly proportional to the size of an electric dipole in ME coupling. Mathematical description of Dzyaloshinskii-Moriya energy can expressed as

$$E_{DM} = \vec{D} \cdot \left[\vec{S}_1 \times \vec{S}_2\right] \tag{2.10}$$

This is the origin of bilinear magnetoelectric coupling. This coupling gives possibility for reversing the sign of magnetization as a function of voltage which is useful for memory devices. However, the magnetization arising from the spin canting is quite weak in single compound magnetoelectrics and therefore, one needs to find a way to obtain strong magnetism. Since devices are thin films, an artificial mutliferroic heterostructure can be integrated easily with industrial applications.

This boosted the research for composite systems by coupling a ferroelectric (FE)/ piezoelectric (PE) with ferromagnetic (FM) materials, thereby creating an artificial mutliferroic heterostructure. There are different ways of achieving the magnetoelectric coupling in artificial multiferroic structures like strain mediation, influence of ferroelectric polarization state on the electronic structure of a ferromagnet at the interface and the exchange interaction between a ferromagnet and a multiferroic. A ferromagnet possesses an easy direction of magnetization also known as 'easy axis' which is determined by the minimization of the total free magnetic energy F. F is calculated as the sum of magnetocrystalline energy F_{mc}, the demagnetization energy F_{demag} and the surface or interface magnetic energy $F_{surface}$ in the absence of internal field. Therefore, when a FM comes in contact with a FE, the term related to magnetoelastic energy has to be taken into account corresponding to the voltage induced strain effects on the magnetic properties. With this, one needs to keep in mind that the electronic effects at the interface cause $F_{surface}$ to depend on the voltage. By application of voltage, it is possible to change the direction of magnetic easy axis due to generation of large magnetoelastic energy [45].

2.5.1 Strain-mediated ME

The magnetoelectric coupling through strain-mediation can result in remarkable modulation of magnetic properties. The basic idea behind this is coupling between electrostriction and magnetostriction. **Electrostriction** refers to change in the shape of the material under the application of electric field and **magnetostriction** corresponds to expansion or contraction of a ferromagnetic material in response to an applied magnetic field [3]. This can be achieved by the transfer of strain from a ferroelectric layer placed in proximity to a ferromagnetic layer. On applying the voltage across the system, the coupling between electrostriction and magnetostriction results in strain-mediated ME. Therefore, when the voltage is applied across a FE+FM heterostructure, the FE material deforms due to inverse piezoelectric effect and generates strain which is transferred to the deposited FM layer. This strain transfer can result in change of the coercive field (H_C) and magnetic anisotropy [9].

The total strain in the system is a collective contribution from elastic deformation and ferroelectric/ferroelastic switching. The elastic deformation shifts the entire

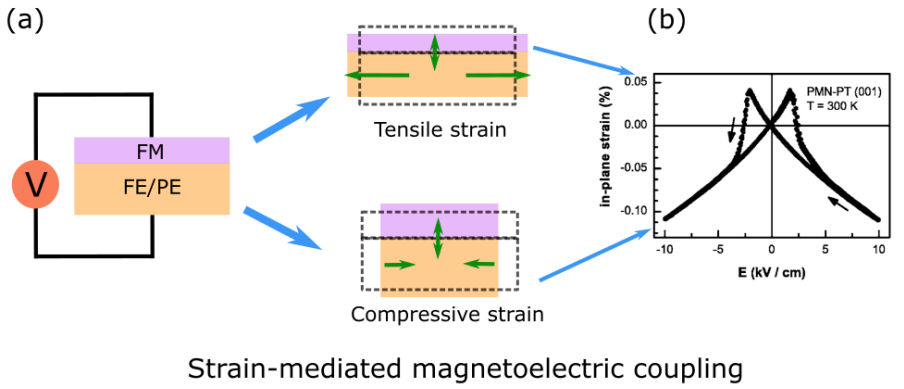

Figure 2.12: **(a)** Schematic of strain coupling in a FE and FM heterostructure **(b)** butterfly-shaped curve characteristic of in-plane piezoelectric strain vs electric field taken from [46] with E||[001] along PMN-PT(001).

strain-electric field curve downwards and the switching contribution becomes significant at higher stress levels resulting in the increase of H_C. This leads to switching of 71° rhombohedral or 90° tetragonal polarizations in the material and they retain their switched state until sufficient electric field is applied to overcome the applied stress state and switch back the polarizations [47]. Fig.2.12 shows how the strain coupling can result in tensile strain and compressive strain. The corresponding butterfly curve is characteristic for strain vs electric field and Fig.2.12b depicts the measurement of LSMO/PMN-PT(001) system from [46]. The tensile strain is always positive and compressive strain is negative. The strain mediated ME coupling is volatile effect and thus cannot be used for switching devices.

2.5.2 Charge-mediated ME

Charge-mediated coupling is an interface effect which is a result of modulation of charge carrier density at the interface between FM and FE layer. The bound charges at the ferroelectric interface vary the charge carrier density in the ferromagnetic layer. This type of magnetoelectric coupling is limited by the Thomas-Fermi screening length in the ferromagnetic material and varies from few Angström to $\approx 1\,\text{nm}$. One can observe radical changes if a complex ferromagnetic oxide like LSMO is coupled with a ferroelectric as the ferroelectric field effect will lead to charge accumulation at the interface thereby altering the charge doping in LSMO [48]. The charge-mediated magnetoelectric coupling gives rise to non-volatile effects due to the presence of remanent polarization of ferroelectric layer yielding change in magnetization which remains stable even after removing the applied electric field. The first charge-mediated ME was observed in PZT/LSMO heterostructure [49].

The charge-mediated voltage control of magnetism can lead to 3 types of effects, **first**: modification of magnetic moments due to enhanced spin imbalance under

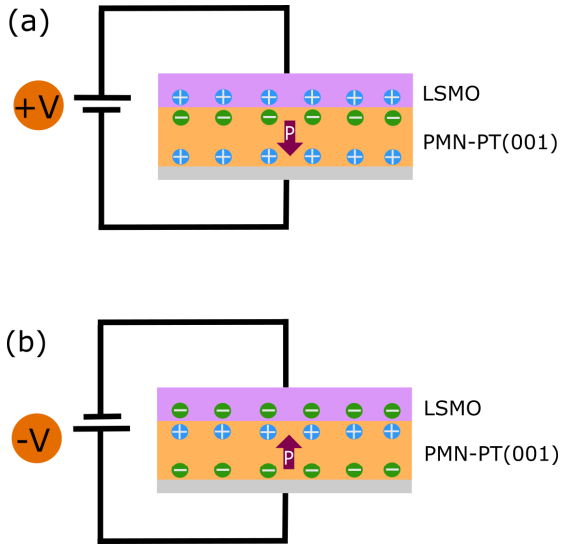

Figure 2.13: Schematic of a charge-mediated coupling taking place in LSMO/PMNPT(001).

applied electric field [50], **second**: alteration of the electronic phase of the magnetic layer (ferromagnet to paramagnet or ferromagnet to antiferromagnet) [51, 52] and **third**: change in magnetic anisotropy arising from different density of states near the Fermi-level under different polarizations [53, 54]. Fig.2.13 depicts the charge-mediated ME taking place in LSMO/PMN-PT(001) heterostructure showing the accumulation of charges at he interface. This will be discussed in detail in the further section of this thesis.

3 Scattering Theory

The basic idea behind scattering theory is that to understand the properties of an object of interest, you throw something at it and analyze whatever bounces back from that object. Scattering can be best understood in terms of interference phenomenon of the radiation waves. The techniques based on scattering provides a non-destructive means to investigate the chemical, electronic and magnetic properties of a material. Different probes like X-rays, neutrons and electrons have been used to study the systems under investigation in this work. This section will give an introduction on the basic concept behind scattering and the characterization methods based on it. This section follows [55], [56] and [57].

3.1 Elementary scattering theory

From de-Broglie and Einstein, it is known that electrons exhibit a wave-particle duality and the wavelength (λ) of a particle wave is dependent on the momentum of the particle by relation

$$\lambda = \frac{h}{p} \tag{3.1}$$

with Planck's constant h and the absolute particle momentum p. Therefore, these particles with different wavelengths can be employed for scattering experiments to probe the system. A simple scattering process is depicted in fig.3.1

For the scattering experiment we take into account the Fraunhofer approximation where the size of the sample is much smaller than the distance between the sample and the source and the distance between the sample and the detector. In addition we assume that the source emits monochromatic radiation with the plane wave having wave vector $\vec{k}$ incident on the sample. The plane wave emitted from the sample and incident on the detector is described with wave vector $\vec{k'}$. Now, considering the case of elastic scattering:

$$k = |\vec{k}| = |\vec{k'}| = \frac{2\pi}{\lambda} \tag{3.2}$$

where λ is the wavelength of the incident and the scattered beam. The scattering vector $\vec{Q}$ can be defined as:

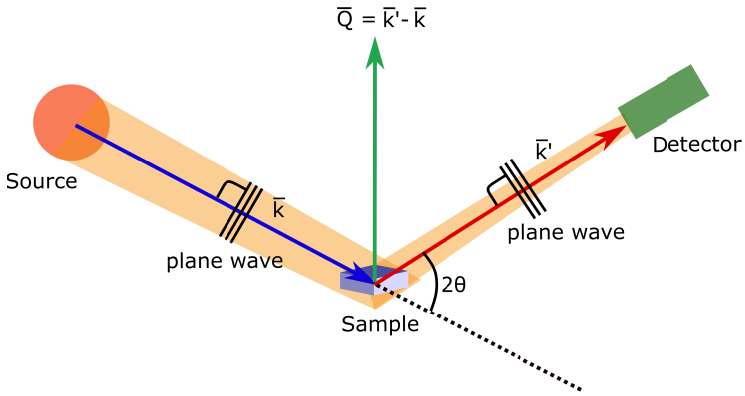

Figure 3.1: Scattering process for a monochromatic radiation under the Fraunhofer approximation.

$$\vec{Q} = \vec{k'} - \vec{k} \tag{3.3}$$

According to de-Broglie, the particle corresponding to the incident wave possesses a momentum of $\vec{p} = \hbar\vec{k}$ and after scattering the momentum transfer occurs which is represented by $\hbar\vec{Q}$ with scattering vector $\vec{Q}$. With wavelength λ and the scattering angle 2θ, one can determine the magnitude of $\vec{Q}$ as follows:

$$Q = |\vec{Q}| = \sqrt{k^2 + k'^2 - 2kk'cos2\theta} \Rightarrow Q = \frac{4\pi}{\lambda} sin\theta \tag{3.4}$$

During scattering experiment the intensity distribution is measured as a function of the scattering vector I($\vec{Q}$) which is proportional to the cross-section which is also known as 'scattering cross section'. The scattering cross section is defined by Fig.3.2 which is based on the probability for an interaction between the incident particle and the sample matter.

The scattered intensity measured by the detector covers the solid angle defined by the active detector area dS and the distance between the scattering event and the detector r, therefore solid angle is

$$d\Omega = \frac{dS}{r^2} \tag{3.5}$$

Now considering the number of particles measured by the detector to be dn from the incoming flux J, scattered from the solid angle $d\Omega$, then the differential cross-section can be defined as

$$\frac{d\sigma}{d\Omega} = \frac{dn}{Jd\Omega} \tag{3.6}$$

Therefore, to determine the total scattering cross section which would give us the scattering probability independent of energy change and scattering angle, one needs to integrate to

$$\sigma = \int_0^{4\pi} \frac{d\sigma}{d\Omega} d\Omega \tag{3.7}$$

By now, we know that the measured scattered intensity is the differential cross section which can be defined as the number of particles dn scattered into a solid angle $d\Omega$ in the detector located at a distance r. For determining the differential cross-section, it becomes important to look into the quantum mechanical description. The quantum mechanics treats neutrons as particle wave fields using Schrödinger equation:

$$H\psi = \left(\frac{\hbar^2}{2m}\Delta + V\right)\psi = i\hbar\frac{\partial}{\partial t}\psi \tag{3.8}$$

where ψ is the probability density amplitude and V is the interaction potential. Now, considering the case of elastic scattering (E = E'), the time-dependent factor can be described as $e^{\left(-i\frac{E}{\hbar}t\right)}$ which leads to a wave equation for the spatial part of the probability density amplitude ψ as

$$\Delta\psi + k^2(\vec{r})\psi = \frac{2m}{\hbar^2}V\psi \tag{3.9}$$

with spatially varying wave vector

$$k^2(\vec{r}) = \frac{2m}{\hbar^2}\left(E - V(\vec{r})\right) \tag{3.10}$$

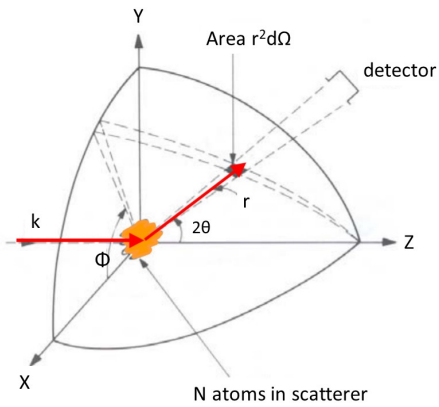

Figure 3.2: Definition of scattering cross section. Adapted from [57]

In vacuum ($V(\vec{r}) = 0$), the solution of this wave equation is given by plane waves $\psi = \psi_0 e^{\left[i\left(\vec{k}\vec{r} - \frac{E}{\hbar}t\right)\right]}$ with energy $E = \frac{\hbar^2 k^2}{2m}$. For an inhomogeneous ($V(\vec{r}) \neq 0$) solution, when the wave packet reaches the region which is under the influence of the potential $V(\vec{r})$, its wave function is then obtained from the superposition of the plane wave e^{ikr} and a scattered wave. The structure of this scattered wave is dependent on the potential $V(\vec{r})$. However, its asymptotic form is simple. The scattered wave in a given direction (θ, ϕ) will have a radial dependence in the form of $\frac{e^{ikr}}{r}$. It is an outgoing wave which will have same energy as the incident wave and the factor $\frac{1}{r}$ results from the fact that there are 3 spatial dimensions:

$$(\Delta + k^2)\frac{e^{ikr}}{r} = 0 \tag{3.11}$$

for r $\geq r_0$, where r_0 is any positive distance. Since scattering is isotropic, the amplitude of the outgoing wave will depend on the direction (θ, ϕ). Therefore, the wave function $\psi^{(scatt)}(\vec{r})$ associated with the stationary scattering state in its asymptotic form is:

$$\psi^{(scatt)}(\vec{r}) \underset{r\to\infty}{\sim} e^{i\vec{k}\vec{r}} + f(\theta, \phi)\frac{e^{i\vec{k}\vec{r}}}{r} \tag{3.12}$$

In this equation, the function $f(\theta, \phi)$ is called *scattering amplitude*, which depends on the potential $V(\vec{r})$. The differential cross-section is simply the square of the modulus of the scattering amplitude:

$$\frac{d\sigma}{d\Omega} = |f(\theta, \phi)|^2 \tag{3.13}$$

The scattering amplitude $f(\theta, \phi)$ can be determined by introducing an integral scattering equation, whose solutions are precisely these stationary scattering state wave functions. Suppose, there exists a function $G(\vec{r})$ such that:

$$(\Delta + k^2)G(\vec{r}) = \delta(\vec{r}) \tag{3.14}$$

[$G(\vec{r})$ is the "Green's function" of the operator $\Delta + k^2$]. Then any function $\psi(\vec{r})$ which satisfies:

$$\psi(\vec{r}) = \psi_0(\vec{r}) + \int d^3r' G(\vec{r} - \vec{r'})V(\vec{r'})\psi(\vec{r'}) \tag{3.15}$$

where $\psi_0(\vec{r})$ is a solution of the homogeneous equation:

$$(\Delta + k^2)\psi_0(\vec{r}) = 0 \tag{3.16}$$

The equation 3.12 suggests the choice of incident plane wave $e^{i\vec{k}\vec{r}}$ for $\psi_0(\vec{r})$ and with Green's function $G(\vec{r})$, the integral scattering equation can be written as:

$$\psi^{(scatt)}(\vec{r}) = e^{i\vec{k}\vec{r}} + \int d^3r' G(\vec{r} - \vec{r'})V(\vec{r'})\psi^{(scatt)}(\vec{r'}) \tag{3.17}$$

whose solutions represent the asymptotic behaviour given by eq. 3.12. Now,

$$G(\vec{r}-\vec{r'}) = -\frac{1}{4\pi}\frac{e^{ik|\vec{r}-\vec{r'}|}}{|\vec{r}-\vec{r'}|} \underset{r\to\infty}{\sim} -\frac{1}{4\pi}\frac{e^{ikr}}{r}e^{-i\vec{k'}\vec{r'}} \tag{3.18}$$

where $\vec{k'}$ is the scattered wave vector in the direction (θ, ϕ). Using eq. 3.18 in eq. 3.17, we get

$$\psi^{(scatt)}(\vec{r}) \underset{r\to\infty}{\sim} e^{i\vec{k}\vec{r}} - \frac{1}{4\pi}\frac{e^{i\vec{k}\vec{r}}}{r}\int d^3r' e^{-i\vec{k'}\vec{r'}}V(\vec{r'})\psi^{(scatt)}(\vec{r'}) \tag{3.19}$$

Thus, scattering amplitude becomes:

$$f(\theta,\phi) = -\frac{1}{4\pi}\int d^3r' e^{-i\vec{k'}\vec{r'}}V(\vec{r'})\psi^{(scatt)}(\vec{r'}) \tag{3.20}$$

Now, defining the incident wave vector $\vec{k}$ as the vector modulus of k such that, $e^{ikr} = e^{i\vec{k}\cdot\vec{r}}$ and the scattering wave vector $\vec{Q} = \vec{k'} - \vec{k}$ and substituting $\psi^{(scatt)}(\vec{r'}) = e^{i\vec{k}\vec{r'}}$ in eq. 3.20, we obtain Born expansion of scattering amplitude. Taking $f(\theta,\phi) = f(\vec{Q})$ and limiting to the first order of **First Born approximation**, we get

$$\begin{aligned} f(\vec{Q}) &= -\frac{1}{4\pi}\int d^3r' e^{-i\vec{k'}\vec{r'}}V(\vec{r'})e^{i\vec{k}\vec{r'}} \\ &= -\frac{1}{4\pi}\int d^3r' e^{-i(\vec{k'}-\vec{k})\cdot\vec{r'}}V(\vec{r'}) \\ &= -\frac{1}{4\pi}\int d^3r' e^{-i\vec{Q}\cdot\vec{r'}}V(\vec{r'}) \end{aligned} \tag{3.21}$$

The Born approximation can be explained on the basis of an assumption that an incoming wave scatters only once inside the target potential before forming a scattered wave. The scattering cross-section in Born approximation is thus simplified to its Fourier transform of potential. Therefore, from the relation between scattering cross-section and scattering amplitude, it becomes

$$\frac{d\sigma}{d\Omega} = \frac{m^2}{4\pi^2\hbar^4}|d^3\vec{r}e^{-i\vec{Q}\cdot\vec{r'}}V(\vec{r'})|^2 \tag{3.22}$$

From the framework of Born approximation, one sees how studying the variation of the differential cross-section in terms of scattering direction and incident energy can give us information about the potential V($\vec{r}$).

3.2 Atomic form factors

X-ray scattering length relies on the number of orbital electrons which is equal to the number of protons in a neutral atom. The nature of form factor $f(\vec{Q})$ depends

on the element and is defined as the normalized amplitude of scattering from within one particle. It describes the form of the particle.

$$f(\vec{Q}) = \int \rho(\vec{r}) e^{(i\vec{Q}\vec{r})} d^3\vec{r} \tag{3.23}$$

where $\rho(\vec{r})$ is the spatial density of the scatterer about its center of mass ($\vec{r} = 0$) and $\vec{Q}$ is the momentum transfer. Therefore, the broader the distribution of the scatterer in the real space, the narrower will be the distribution of $f(\vec{Q})$ leading to faster decay of the form factor. Since, X-rays interact only with electrons which means higher the Z, the more will be the scattering and the decay will be faster with increasing scattering angle θ. However, for neutrons the interaction takes place between the neutrons and the atomic nucleus which is characterized by scattering length b and it is independent of the scattering angle and thus there is no decay with increasing scattering angle.

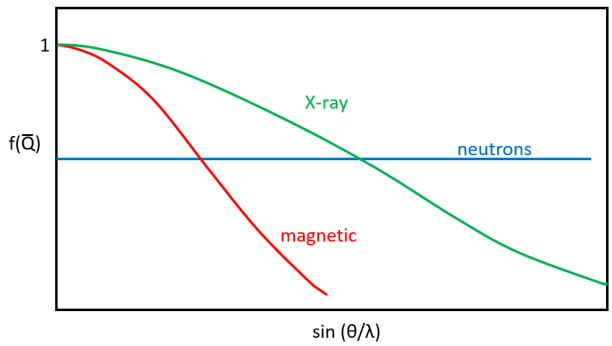

Figure 3.3: Atomic and magnetic form factors. Inspired from [58]

3.3 Magnetic form factor

With neutron possessing spin = 1/2 and a magnetic moment of μ_n = -1.913 μ_N gives rise to magnetic interactions between the spins of the neutrons as well as the magnetic moments of the magnetic atoms. The magnetic moments of the magnetic ions will cause the variation of the magnetic form factor similar to X-rays but the fall of $f(\vec{Q})$ is even more pronounced due to the involvement of only outermost electron orbitals as depicted in fig.3.3. The form factor reveals the distribution of the spin and the orbital magnetization.

3.4 Properties of neutron

In the sections above, we discussed about the scattering basics with respect to X-rays and neutrons. This section will deal with properties of neutrons and what makes them interesting and useful.

The neutron is an elementary particle with a diameter of about $1fm = 10^{-15}m$. It is not a stable particle due to weak interactions and a free neutron undergoes a β-decay after an average lifetime of about 15 minutes, leaving ample time for scattering experiments

$$n \longrightarrow p + e^{-} + \overline{v} \tag{3.24}$$

A neutron has a mass of about $m \sim 1.675 \times 10^{-27}$ kg. Being a chargeless particle, neutron results in large penetration depths. Since neutrons interact with the nuclei, they are very sensitive to low Z elements like hydrogen. It also carries a nuclear spin 1/2 which gives rise to a magnetic dipolar moment as mentioned in section 3.3. Therefore, with this magnetic moment, the neutrons are able to interact with the magnetic field of unpaired electrons resulting in magnetic scattering.

3.5 Reflectivity

Reflectivity is an important technique which enables us to get information on the stacking, thickness and the roughness of the thin film. It probes the laterally averaged structure of the surface and the interface. With neutrons as the probe one can get information about the magnetic depth profile of the thin film which will be discussed later. A simple set-up for specular reflectivity experiment has a beam of X-rays or neutrons of wavelength λ that impinges the planar sample surface at a grazing angle $\alpha_i = \theta$ and a fraction of it is reflected specularly from the surface at an outgoing angle $\alpha_f = \theta$ while a part of it is refracted into the material. The refracted beam is also scattered at the interface resulting in further reflected and refracted part. These reflected beam from different surfaces in a sample interfere constructively and destructively giving rise to reflectivity curve.

Reflectometry probes the scattering length density (SLD) in z-direction resulting in lateral averaging of thickness or roughness. However, if the surface of the film has some roughness or some features then it results in diffuse scattering (Fig.3.4b). Also known as off-specular scattering and it takes place if $\alpha_i \neq \alpha_f$. Off-specular scattering arising from lateral structures with high correlation length will give rise to sharp reflections.

In case of neutrons as a probe, for most materials the index of refraction is slightly smaller than 1, leading to total external reflection for small angles of incidence $\theta < \theta_c$ and the absorption of neutrons is negligible. However, in case of X-rays, the index of

refraction consists of a real part, called dispersion and imaginary part for absorption. Hence, index of refraction is

$$n = 1 - \delta + i\beta \tag{3.25}$$

For neutrons, the real part is given by

$$\delta = \frac{\lambda^2}{2\pi} \sum_j b_j \rho_j \tag{3.26}$$

and for X-rays

$$\delta = \frac{\lambda^2 r_0}{2\pi} \sum_j \rho_j (Z_j + f'_j) \tag{3.27}$$

and refractive index becomes

$$n = 1 - \frac{\lambda^2 r_0}{2\pi} \sum_j \rho_j (Z_j + f'_j + if"_j) \tag{3.28}$$

where b_j is the coherent scattering length, ρ_j is the number density of the different elements, r_0 is the classical electron radius, Z is the number of electrons in the

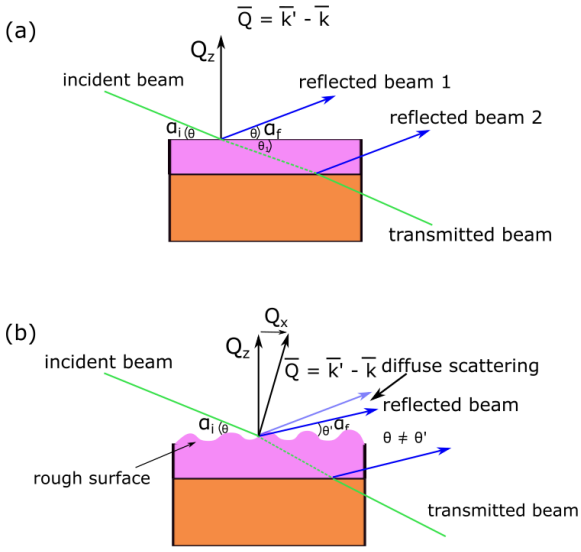

Figure 3.4: a) Schematic of scattering geometry with specular reflectivity where the surface is flat **b)** off-specular scattering or diffuse scattering due to surface roughness or features.

atoms and f' and f'' are corrections for dispersion and absorption close to resonance energies. Typically, they can be neglected and are only important at the absorption edges. Reflectivity **R** is defined as the ratio of the intensities reflected and incoming waves, and transmittance **T** is defined as the ratio of intensities of transmitted and incoming waves. Now according to Fresnel's formulas, the reflectivity and the transmittance from a flat interface can be derived as

$$\text{Reflectivity } R = \left|\frac{\theta - n_1\theta_1}{\theta + n_1\theta_1}\right|^2 \tag{3.29}$$

$$\text{Transmittance } T = \left|\frac{2\theta}{\theta + n_1\theta_1}\right|^2 \tag{3.30}$$

where $\theta = \alpha_i$, angle of incidence and θ_1 is angle of refraction

From Snell's law for refraction

$$\frac{\cos\theta}{\cos\theta_1} = n_1 \tag{3.31}$$

For the angles of incidence θ below the critical angle θ_c, n $= \cos\theta_c$ and $\theta_c \approx \sqrt{2\delta}$, total reflection is observed. All the intensity will be reflected with no wave propagating in z-direction. For incident angles $\theta > \theta_c$, the beam can partially penetrate the sample and is only partly reflected..

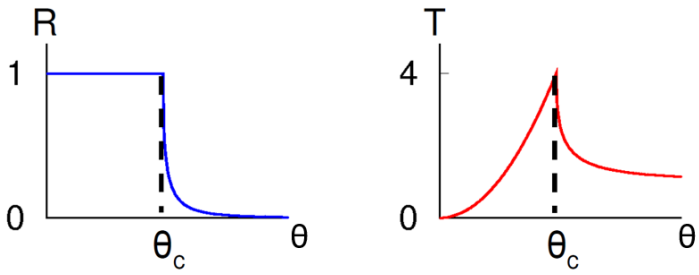

Figure 3.5: Reflectivity and transmittance plotted as a function of the angle of incidence.

3.6 Polarized Neutron Reflectometry

Now since we know that neutron is a spin $\frac{1}{2}$ particle, it can interact with the magnetic induction $\vec{B}$ of a sample and with neutron reflectometry as a tool, one can use it to study the magnetic depth profile of a layered heterostructure. The potential for the interaction of the neutron with a homogeneous magnetic material can be separated

into two parts:

$$\widehat{V_1} = V_1^N \hat{1} + \widehat{V_1}^M \tag{3.32}$$

where V_1^N represents the nuclear interaction and $\hat{1}$ is the unity operator, which does not affect the spin state, so that nuclear interaction can be described independently of the neutron's spin. The second term $\widehat{V_1}^M$ describes the magnetic dipole interaction, which is a scalar product of the neutron magnetic moment operator $\mu_n \hat{\sigma}$ and the magnetic induction $\vec{B_1}$ inside the material: $\widehat{V_1}^M = -\mu_n \hat{\sigma} \cdot \vec{B_1}$.

The magnetic field $\vec{H}$, is typically applied in the plane of the sample. Choosing in-plane direction to be along x-direction of the coordinate system $\vec{H} = H\vec{e_x}$ and also as the quantization axis for the neutron spin. Under this assumption, the spin operator $\hat{\sigma} = (\sigma_x, \sigma_y, \sigma_z)$ has following components (Pauli matrices):

$$\sigma_x = \begin{pmatrix} 1 & 0 \\ 0 & -1 \end{pmatrix} \quad \sigma_y = \begin{pmatrix} 0 & 1 \\ 1 & 0 \end{pmatrix} \quad \sigma_z = \begin{pmatrix} 0 & -i \\ i & 0 \end{pmatrix} \tag{3.33}$$

Therefore, the Schrödinger equation can be solved in coordinate and spin space, where the eigenvectors $|+\rangle$ and $|-\rangle$ of the operator $\hat{\sigma} \cdot \vec{b_0} = \sigma_x$ with the eigenvalues +1 and -1 , respectively, define the states of the neutron with "spin up ↑" and "spin down ↓". The solution of the Schrödinger equation is the neutron wave function $|\Psi(\vec{r})\rangle$, which is a linear combination of those two spin states.

$$\Psi(\vec{r})\rangle = \Psi_\uparrow(\vec{r})|+\rangle + \Psi_\downarrow(\vec{r})|-\rangle = \begin{pmatrix} \Psi_\uparrow(\vec{r}) \\ \Psi_\downarrow(\vec{r}) \end{pmatrix} \tag{3.34}$$

After some calculations, one gets a set of two coupled 1D linear differential equations for every layer as:

$$\Psi''_\uparrow(z) + \left[k_{z1}^2 - 4\pi(\rho_1^N + \rho_1^M m_{x1})\right] \Psi_\uparrow(z) - 4\pi\rho_1^M m_{y1} \Psi_\downarrow(z) = 0 \tag{3.35}$$

$$\Psi''_\downarrow(z) + \left[k_{z1}^2 - 4\pi(\rho_1^N - \rho_1^M m_{x1})\right] \Psi_\downarrow(z) - 4\pi\rho_1^M m_{y1} \Psi_\uparrow(z) = 0 \tag{3.36}$$

In these equation, ρ^N represents the nuclear scattering length density (NSLD) and its magnetic analog ρ^M, magnetic scattering length density (MSLD), which is directly proportional to the net magnetization M of the material. In case of a FM material, the magnetization vector $\vec{M}$ is aligned in some direction, which is described by the unit vector $\vec{m} = \vec{M}/M$. From eq. 3.35, one can see that for non-spin flip (NSF) interaction, for spin ↑, it is the sum of nuclear interaction and magnetic interaction along the quantization direction whereas for spin ↓ (eq. 3.36), it is the difference of nuclear and magnetic interaction. This means, in case of magnetically saturated layer, the scattering length density (SLD) for spin ↑ neutron is enhanced and for spin ↓ neutrons is reduced compared to nonmagnetic case. Thus, it affects the refractive index, total angle of reflections and the reflectivity and one will observe a splitting between reflectivity of both polarization states of the neutron beam.

In case of unsaturated magnetic layer, the component along the field direction will influence the SLD of NSF channel and the in-plane component perpendicular to the field will induce a spin-slip (SF) interaction that is equally strong for both SF channels +-(↑↓) and -+(↓↑).

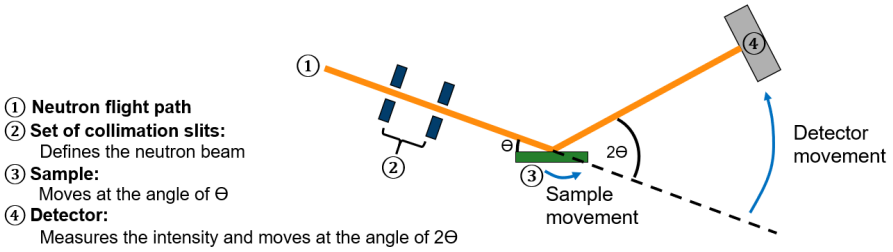

Figure 3.6: Geometric sketch of neutron reflectometry set-up

Suppose, we have a magnetic thin film deposited on a substrate and we want to get information about how the magnetic moments are arranged in the system. For this first we need a set-up for neutron reflectometry. A basic neutron reflectometry set-up requires a (i) radiation source,(ii) a monochromator - to have selected band of wavelengths of neutron beam, (iii) a collimation system - to define the neutron beam, (iv) a sample stage and (v) a detector as shown in fig. 3.6.

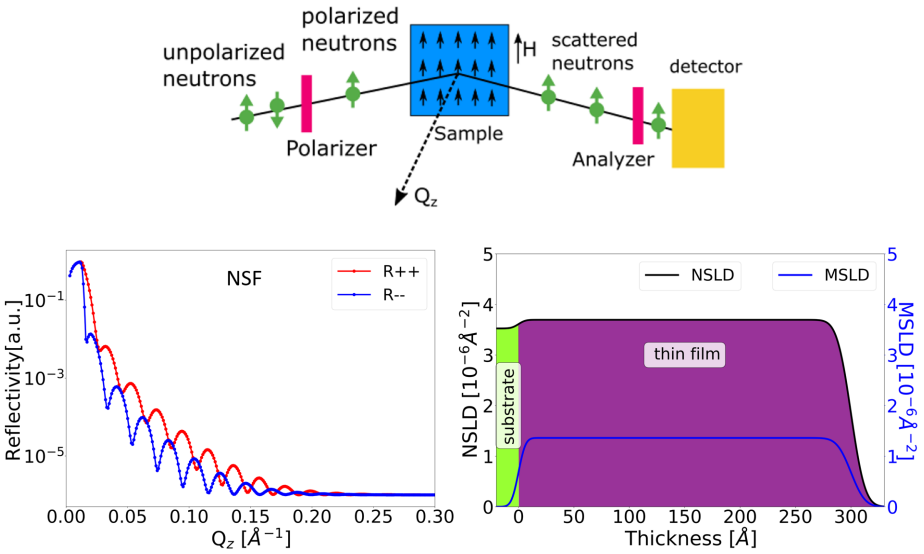

Figure 3.7: PNR depicting Non-spin flip (NSF) channels

For investigating the magnetic structure, we need a 'polarizer' which would select the projection of the neutron spin on the quantization axis (which is the direction of applied magnetic field) before the interaction with the sample and a 'polarization analyzer' to retrieve information about the norm and angle of magnetization in a sample after interaction.

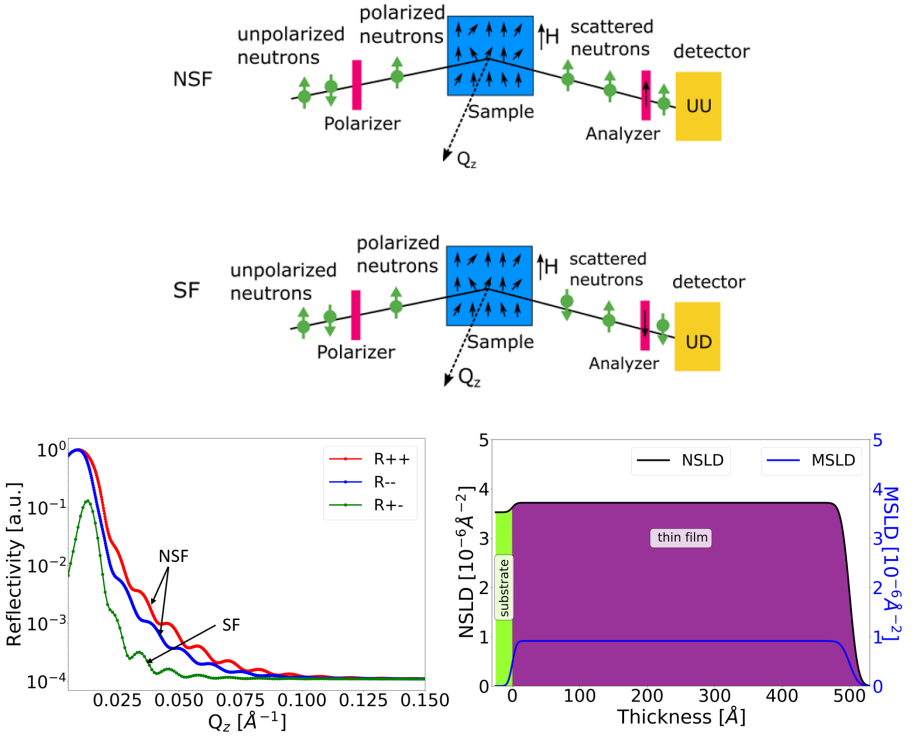

Figure 3.8: PNR depicting Non-spin flip (NSF) and Spin-flip (SF) channels

Fig.3.7 depicts a schematic of NSF channels. In PNR, one talks in terms of 4 channels namely : *R++ (UU), R– (DD), R+- (UD) and R-+ (DU).* UU (R++) means polarizer and analyzer will allow only neutrons with spin ↑ to pass through whereas, for R+- (UD) the polarizer will allow neutrons with spin ↑ and the analyzer will allow neutrons with spin ↓ to pass. Consider a system that has a FM thin film and the applied $\vec{H}$ is high enough to saturate the film, thus, all magnetic moments will be aligned in the direction of the field as shown in Fig.3.7. Now, when a neutron with spin ↑ will interact with the sample, it will result in NSF event as neutron spin and magnetic moment in the film are parallel and one will get curves UU and DD. The splitting between UU and DD arises due to the magnetization of the film, the more magnetization, the higher is the splitting and with different physical models, one can fit the reflectivity curve which yields the scattering length density profile (SLD). The total scattering amplitude will have both nuclear and magnetic part. The SLD profile depicts how the magnetization varies across the film and from

nuclear part one can determine the stoichiometric fluctuations, film roughness and substrate roughness.

In case of a non-saturated film, the magnetization can be canted away from the polarization direction of the neutron spin. The component of the magnetization perpendicular to the neutron polarization will cause SF scattering, while the parallel component leads to NSF scattering as shown in Fig.3.8. For such cases, one has to measure UD and DU channels as well along with UU and DD. Hence, when a neutron with spin ↑ will interact with a magnetic component perpendicular to it, the SF scattering will occur and this spin-flipped neutron ↓ will be able to pass through analyzer, given analyzer spin selection is ↓ resulting in SF signal. In this way one can determine the magnetic depth profile using Polarized Neutron Reflectometry.

3.7 Diffraction

The crystallinity of a film is determined by the diffraction technique where the incident beam results in an interference pattern after encountering a structure. With the resulting interference pattern one can obtain information about the internal lattice of a crystalline structure, unit cell dimensions, site-ordering and depending on the probe (neutrons) magnetic ordering as well. X-rays and neutrons have the wavelength in an order of 10^{-10} m and therefore, can be used to probe the crystal structures. In this thesis work, X-ray diffraction has been used to determine the crystallinity of the thin films. A crystal lattice in three dimensions can be described by three translational vectors $\vec{a_1}, \vec{a_2}$ and $\vec{a_3}$. Using a linear combination, one can address all the lattice points as

$$\vec{a} = u\vec{a_1} + v\vec{a_2} + w\vec{a_3} \tag{3.37}$$

where u,v and w are arbitrary integers. The diffraction pattern depends on the crystal structure and the wavelength of the probe. W.L. Bragg gave a simple explanation of diffraction from crystal. When an incident wave strikes a crystal with parallel planes of atoms, it is reflected specularly from each plane with $\alpha_i = \alpha_f = \theta$. These reflected beams interfere constructively yielding a diffraction pattern. As presented in the Fig.3.9, with parallel atomic planes distance ,d, apart then the path difference is $2d \sin\theta$ between the reflected rays from adjacent atomic planes.The constructive interference will occur when the path difference is an integral number n of the wavelength λ, yielding Bragg's law

$$2d \sin\theta = n\lambda \tag{3.38}$$

The periodicity of the lattice is the base for Bragg's law. Now, with X-ray diffraction, the lattice parameters of the epitaxially grown thin film can be deduced and for that one needs to model the scattered intensity for a single crystalline layer using the electron density ρ_e of the thin film. In this thesis work, the out-of-plane lattice parameter of the film is parallel to one of the crystallographic axis. This

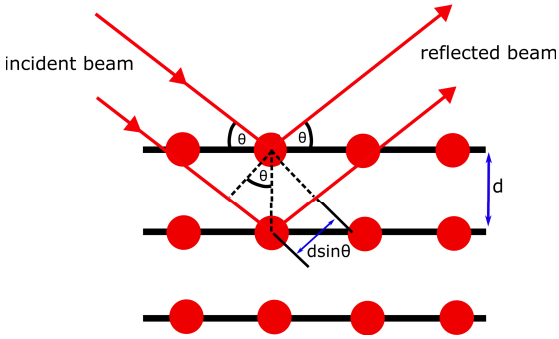

Figure 3.9: Schematic of Bragg's law $2d\sin\theta = n\lambda$, where d is the space between the parallel atomic planes and $2\pi n$ is the phase difference between the reflections from successive planes. Inspired from [59]

means that the layer consisting of N,M and P unit cells along x, y and z direction, the z will be the out-of-plane direction. The overall structure of a thin film can be described mathematically as a convolution of periodic lattice and the unit cell structure. The Fourier transform of ρ_e can be written as a product of Fourier transform of lattice functionρ_L times the Fourier transform of the unit cell function $\rho_{u.c.}$ using convolution theorem:

$$\rho_L \propto \sum_{n=0}^{N-1}\sum_{m=0}^{M-1}\sum_{p=0}^{P-1}\delta(\vec{r}-(n\vec{a}+m\vec{b}+p\vec{c})) \tag{3.39}$$

where $\vec{a},\vec{b}$ and $\vec{c}$ are lattice parameters. The Fourier transform of eq.3.39 yields Laue-function for point like scatterers

$$I(\vec{Q}) \propto \frac{\sin^2\left(\frac{1}{2}N\vec{Q}\vec{a}\right)}{\sin^2\left(\frac{1}{2}\vec{Q}\vec{a}\right)}\cdot\frac{\sin^2\left(\frac{1}{2}M\vec{Q}\vec{b}\right)}{\sin^2\left(\frac{1}{2}\vec{Q}\vec{b}\right)}\cdot\frac{\sin^2\left(\frac{1}{2}P\vec{Q}\vec{c}\right)}{\sin^2\left(\frac{1}{2}\vec{Q}\vec{c}\right)} \tag{3.40}$$

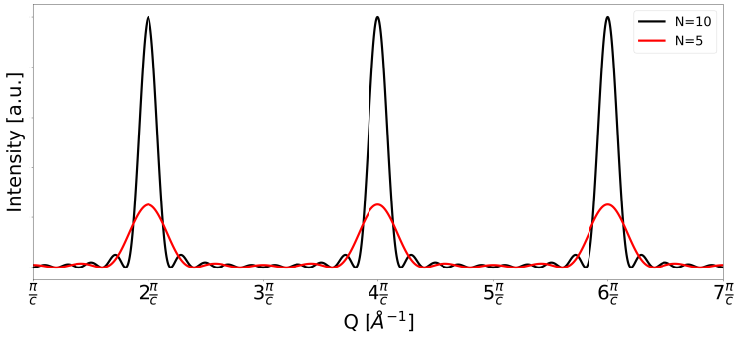

Figure 3.10: Plot of Laue function along the lattice direction $\vec{c}$ with 5 and 10 periods

The Laue function along lattice direction $\vec{c}$ is plotted in Fig.3.10. The maxima occur at the positions $Q = n \cdot \frac{2\pi}{c}$ and are also known as Bragg reflections obtained for scattering from a crystal lattice . The intensity of Bragg reflections scale to the square of the number of periods N^2 and the width of $\frac{2\pi}{N}$. With the increasing number of periods N, the intensity of Laue oscillations becomes negligible compared to the intensity of the Bragg reflections. From the positions of Bragg peaks, it is possible to determine the lattice constants and the unit cell angles.

4 Scattering with Electrons

This chapter discusses the scattering processes that take place when electrons interact with a solid matter and the techniques based on electron scattering used in this thesis. The literature is based on the textbook written by D.B. Williams and C.B. Carter: *Transmission Electron Microscopy* [60].

4.1 Interaction of electrons with matter

It is known that electron exhibits wave-particle duality based on de-Broglie's ideas, where the particle momentum, p, is related to its wavelength, λ, through Planck's constant, h: $\lambda = \frac{h}{p}$. Now in TEM, the momentum is imparted to an electron by accelerating it through a potential drop, V, giving it a kinetic energy of eV. This potential energy must be equal to the kinetic energy, which yields in non-relativistic approximation:

$$eV = \frac{m_0 \nu^2}{2} \tag{4.1}$$

where m_0 is the mass of an electron and ν is the velocity. Thus, using eq. 4.1, the momentum can be equated as

$$p = m_0 \nu = (2 m_0 eV)^{1/2} \tag{4.2}$$

Furthermore using eq. 4.2 in de-Broglie's relation, one gets

$$\lambda = \frac{h}{(2 m_0 eV)^{1/2}} \tag{4.3}$$

From this equation, one can see that, by increasing the accelerating voltage, the wavelength of electrons decreases. Until now, the relativistic effects have been ignored, but for energies higher than 100 keV, the relativistic effects have to be taken into account. This is because the velocity of the electrons (as particles) becomes greater than half the speed of light. Therefore, eq. 4.3 can be modified as

$$\lambda = \frac{h}{\left[2m_0eV\left(1+\frac{eV}{2m_0c^2}\right)\right]^{1/2}} \tag{4.4}$$

When electrons passes through a thin sample, different scattering processes take place: elastic (no loss of energy) and inelastic (change in energy) scattering, coherent and incoherent scattering as shown in Fig. 4.1. The coherently scattered electrons stay in-phase while the incoherently scattered electrons lose the phase relationship after the scattering event. Elastic scattering usually occurs at low angles in the range from 1° - 10°. As the angle becomes larger than 10°, the elastic scattering becomes more incoherent, whereas for inelastic scattering, it always incoherent and occurs typically at angles lower than $< 10°$.

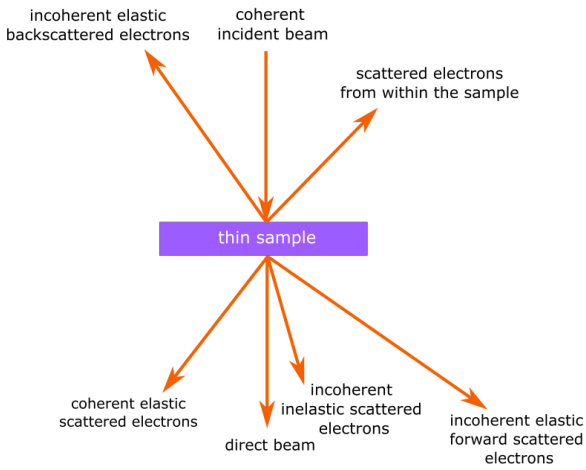

Figure 4.1: Different kind scattering events with electrons passing through a thin sample. Inspired from [60].

Electrons can scatter more than once with increasing scattering angle and the more the scattering events, the more difficult it gets to interpret the images and the spectra obtained. Therefore, to avoid the multiple scattering events, one needs to thin down the sample so that it becomes electron transparent, which is the basis of the TEM. The specimen thickness for TEM is usually in the range from a monolayer (*e.g.* graphene) to a few hundred nanometer depending from the material and acceleration voltage of the TEM (typically 60 to 300 kV). With TEM, unless one has a thick sample which will result in multiple scattering, the single-scattering assumption is plausible for thin enough specimens. Therefore it is important to have very thin samples for TEM experiments. The electrons that are scattered in forward direction, parallel to the incident beam, form the direct beam, which is used for most of the elastic scattering, diffraction, refraction and the inelastic scattering. The scattering events depend on various factors such as thickness, density, crystallinity, atomic number of the scattering atom and the angle of sample with respect to the incident beam.

4.2 Interaction cross-section

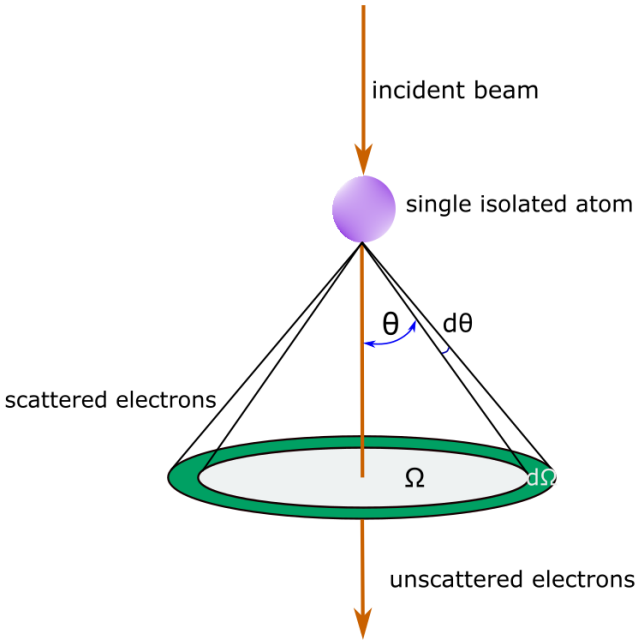

Figure 4.2: Electron scattering by single isolated atom, where the electron is scattered through an angle θ and the total solid angle of scattering is Ω. An incremental increase in scattering angle $d\theta$ gives an incremental increase in a solid angle $d\Omega$, which is the basis for determining the differential scattering cross-section. Inspired by [60].

In TEM, the electrons which pass through the sample are of utmost importance. The probability of an electron undergoing any kind of interaction with an atom is determined by an interaction cross-section. The cross-section does not represent a physical area but, when divided by the actual area of an atom, it represents a probability of the scattering event. The larger the cross-section, the higher the chances of scattering event to occur.

Consider an isolated atom with an cross-sectional area of

$$\sigma_{atom} = \pi r^2 \tag{4.5}$$

where r is the effective radius of a single, isolated atom. The angular distribution of scattering from an atom can be described by the differential cross-section ($\frac{d\sigma}{d\Omega}$). Fig.4.2 depicts the electron scattering event where electrons are scattered at an angle θ into a solid angle Ω and there exists a simple geometric relation between θ and Ω

$$\Omega = 2\pi\,(1 - \cos\theta) \tag{4.6}$$

and

$$d\Omega - 2\pi \sin\theta d\theta \tag{4.7}$$

where $d\theta$ gives an incremental increase in solid angle $d\Omega$ due to incremental increase in scattering angle. Therefore, the differential cross-section can be written as

$$\frac{d\sigma}{d\Omega} = \frac{1}{2\pi \sin\theta} \frac{d\sigma}{d\theta} \tag{4.8}$$

Now σ_{atom} can be calculated for scattering into all angles greater than θ by

$$\sigma_{atom} = \int_{\theta}^{\pi} d\sigma = 2\pi \int_{\theta}^{\pi} \frac{d\sigma}{d\Omega} \sin\theta d\theta \tag{4.9}$$

Now consider a sample with N number of atoms per unit volume, the total cross-section for scattering from the sample can be defined as

$$\sigma_{total} = N\sigma_{atom} \tag{4.10}$$

where $N = \frac{N_0\rho}{A}$, N_0 = Avogadro's number, A = atomic weight of the scattering atoms with density ρ. Thus,

$$\sigma_{total} = \frac{N_0\sigma_{atom}\rho}{A} \tag{4.11}$$

In eq. 4.11, one can define σ_{total} as the number of scattering events per unit distance that the electron travels through the sample. If the sample has thickness t, the probability of scattering is

$$\sigma_{total}t = \frac{N_0\sigma_{atom}(\rho t)}{A} \tag{4.12}$$

4.3 Specimen preparation for TEM

In this thesis, electron transparent specimens for TEM measurements were prepared using focused ion beam (FIB) sputtering in a scanning electron microscope by Lidia Kibkalo from ER-C-1. The dual beam scanning electron microscopy (SEM) and FIB system allows to prepare location sensitive TEM specimens with required geometry and thickness. The single ion gun produces a well controlled beam of Ga ions using an acceleration voltages between typically 0.5 and 30 keV. Insulator materials tend to charge under the electron beam illumination, therefore the specimen preparation was started by depositing a thin few nm thick Au layer on the surface. As depicted in fig.

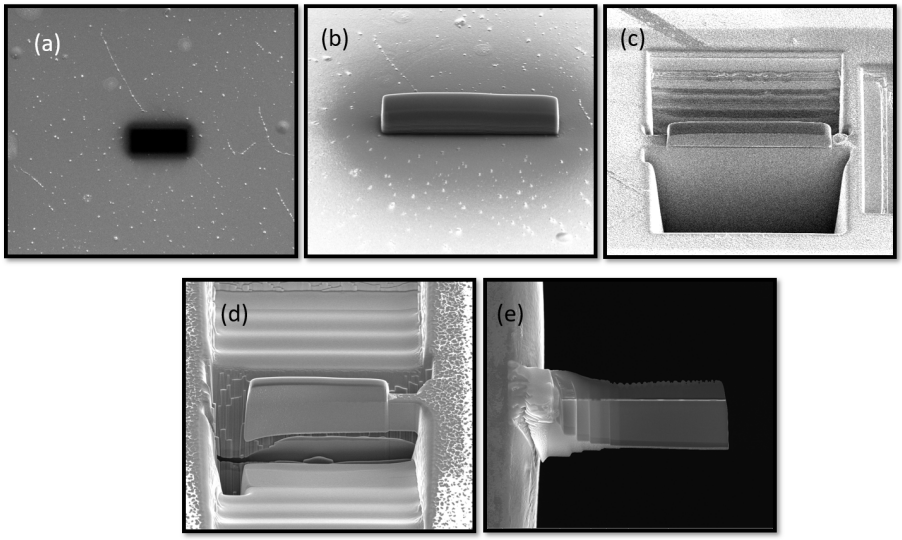

Figure 4.3: FIB preparation of LSMO/PMN-PT (001) sample for TEM studies. **(a, b)** Protective layer deposition on dark area, **(c)** cutting of trenches to take the sample out, **(d)** making an undercut for transfer the lamella to a support grid, **(e)** the thinned specimen is finally attached to the TEM support grid. The protective layer is visible on the top of the sample. Images taken by Lidia Kibkalo (ER-C).

4.3: first a surface protecting layer of C or Pt/C was deposited to protect the sample from the ion irradiation. Then trenches were sputtered on both sides of the specimen, which was followed by an undercut. The piezo controlled micromanipulator system was used to transfer the specimen to a standard Omniprobe style support grid made of copper. The specimen at this step is a few micrometer thick. The final polishing of the specimen was carried out using gradually decreasing ion beam voltages from 30 to 2-5 keV in order to prepare approximately 100 nm thick TEM specimen. In this way one can obtain a cross-section lamella of thin film sample to study the interface properties.

4.4 Instrument set-up

The electron optical system of TEM consist of an electron source, electromagnetic lenses to control the electron beam, apertures, sample stage and different detectors. The electrons are generated and controlled in high vacuum. The modern TEM set-up uses field emission gun (FEG) as an electron source accelerated by 60 to 300 kV voltages, which provide high brightness and coherent electron beam. The 'illumination system' comprises the electron gun to produce electrons and condenser lens system to focus the electrons onto the sample. It can be operated in 2 modes: parallel mode for imaging and electron diffraction and convergent mode for scanning

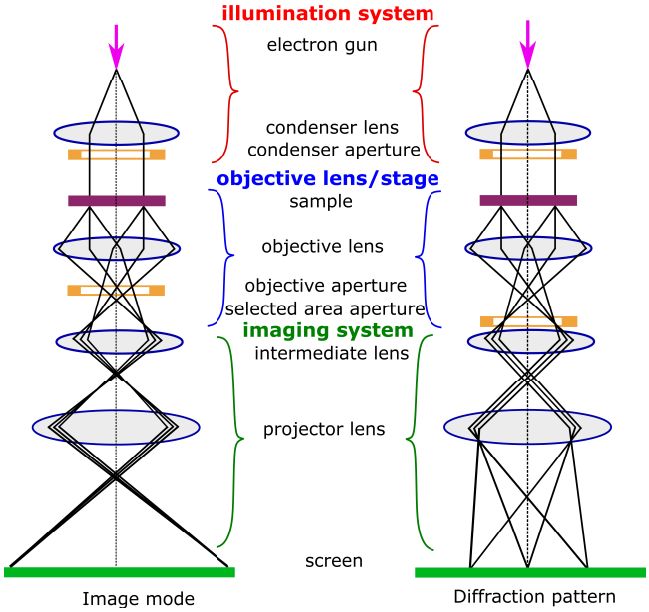

Figure 4.4: TEM modes of operation for imaging and diffraction.

TEM (STEM) imaging and energy dispersive X-ray spectroscopy (EDS). The set-up contains condenser apertures that control the convergent angle of the electron beam as shown in fig 4.4.

The next main part of the set-up is the 'objective lens/stage' which consist of the objective lens, objective aperture and sample stage. The sample is inserted into the pole-piece of the objective lens using a stage that controls the position of the sample and can be also used to apply different external stimuli such as electrical bias, heat, light, electromagnetic fields. The objective aperture is mainly used for bright field and dark field imaging in TEM.

The 'imaging system' is responsible for forming the information from the backfocal plane of the objective lens either in the form of the electron diffraction or as bright field or dark field image into the viewing screen, charged couple device (CCD) or other detectors. It also contains the selected area apertures which can be used in electron diffraction and in the same place electron biprism which is used in electron holography (see section 4.5.4).

In addition, a modern TEM set up is equipped with additional electron optical systems used to correct and control the optical aberrations of the electron beam that leads to sub-Ångstrom image and spectroscopy resolutions. The aberration corrector can be used before the sample to improve the electron beam aberrations that is advantageous for STEM applications or after the sample to improve the image aberrations that limits the spatial resolution provided by the objective lens.

4.5 TEM modes

TEM is a versatile tool that enable to record various different scattering events, X-rays, secondary electrons, etc and provide numerous different imaging and diffraction modes to study the materials structure, composition, electronic and magnetic properties.

4.5.1 Electron diffraction

To understand electron diffraction patterns, kinematical theory of electron diffraction is used. This of course is not applicable to all electron scattering events as it neglects multiple scattering events. However as diffraction arises from coherent and elastic scattering, it considers only those electrons which experience a single scattering event.

Electron diffraction pattern is obtained when the Bragg's condition: $2d\sin\theta = n\lambda$ is fulfilled as shown in fig. 3.9. The diffraction intensity for each crystalline planes is different as the distribution of atoms per unit area is not the same for individual planes. Using the kinematical theory of electron diffraction, one can determine the set of crystal planes for which the diffraction intensity is zero. The structure factor is defined as a mathematical function stating the amplitude and phase of electron beam diffracted from crystallographic planes. This structure factor takes into account the location of atoms in the reflection plane and atomic specifications to describe the diffraction process. Also, the structure factor is the sum of the scattered amplitudes of single atoms f_n and the sum of the phase differences, that is

$$F_{hkl} = \Sigma_n f_n exp\left\{2\pi i(hx_n + ky_n + lz_n)\right\} \tag{4.13}$$

where x_n, y_n, z_n are positions of the atom in the Cartesian coordinates. Then, the intensity of the diffracted wave is

$$I \propto \mid F \mid^2 \propto f^2\left[1 + \cos(\pi(h+k+l))\right]^2 + f^2\left[\sin(2\pi(h+k+l))\right]^2 \tag{4.14}$$

From the above relation, the intensity sometimes becomes zero as it belongs to any diffraction not existing in these planes and is called a forbidden reflection. By using the Bragg's law and structure factor, it is possible to determine the diffracted planes in a crystal. In a real crystal lattice, each of the planes is represented by a point in a reciprocal lattice located at a distance $1/d_{hkl}$ from the center O. A reciprocal lattice is an array of points where each point corresponds to a special plane in a crystal lattice. The distance of a point in the reciprocal lattice to the center is depicted by the vector $g_{(hkl)} = 1/d_{hkl}$, known as diffraction vector. The relation between diffraction pattern and reciprocal lattice is used for the interpretation of different diffraction patterns.

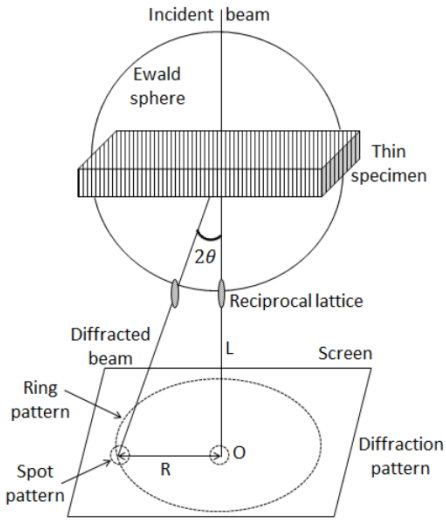

Figure 4.5: Geometrical representation of formation of a diffraction pattern. The relations between incident, transmitted and diffracted beams, the Ewald sphere and different diffraction patterns are illustrated. θ is the angle between transmitted and diffracted beams, R is the distance between collision points of transmitted and diffracted beams and L is the distance between the specimen and the screen. Adapted from [61].

Fig. 4.5 depicts the formation of Ewald sphere in a reciprocal lattice and the diffraction pattern with a radius of $1/\lambda$. When an incident beam of electrons interacts with a thin sample, then a certain percentage of the incident beam gets transmitted, while the rest gets diffracted [61]. Electron diffraction is used to retrieve the basic structural information of a material with which one can determine whether the material is amorphous, single crystalline or polycrystalline. A polycrystalline system will produce an ring pattern and a single crystalline material will result in spot pattern or Kikuchi line pattern or a combination of both. Therefore, by using selected area electron diffraction (SAED) in TEM, one can obtain diffraction patterns as a location sensitive information about the materials.

4.5.2 Scanning Transmission Electron Microscopy -STEM

STEM uses the convergent electron beam to focus the electrons to a fine spot (even to sub-Ångstrom), which then scans the region of interest over the sample in a raster scan illumination system. A typical STEM is equipped with scanning coils which are adjusted to scan the beam on the sample as shown in fig.4.6. The condensor lens system forms the beam and the objective lens focuses the beam. The electron detectors acts as the interface between the incoming electrons from the sample and the image viewed on the display screen.

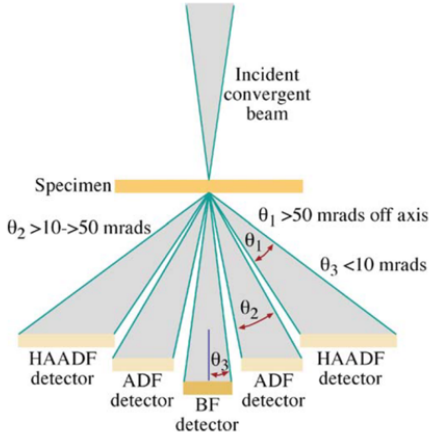

Figure 4.6: HAADF detector set-up for Z-contrast imaging in STEM. Adapted from [60].

STEM takes an advantage on the Rutherford scattering of electrons on atoms which provides chemical sensitivity to the forming image depending from the collection angle used. STEM uses different detectors depending from the collection angle of the electrons as shown in Fig. 4.6. Bright-field detector is positioned at the optical axis of the direct electron beam that detects transmitted electrons deflected typically below angle < 10 mrads and dark-field detectors for electron deflected at higher angles up to several tenths of mrad. The dark-field detectors possess usually a ring shape that allows the direct beam to pass in the middle and provides an angular sensitivity, therefore called annular dark field (ADF) detectors. High-angle annular dark-field (HAADF) detector is used to collect the electrons transmitted at higher angles > 50 mrads, which provides a chemical sensitive information in the STEM image, where the contrast variation scales with the atomic number Z ($I \sim Z^2$) beside of weak diffraction effects. STEM imaging is suitable for parallel recording the deflected electrons for Z-contrast imaging, characteristic X-ray signals induced by scattered electron and the energy-loss of the scattered electrons in order to obtain spectral information as well.

4.5.3 Energy Dispersive X-ray Spectroscopy - EDS

When a high energy electron strikes an atom, it first penetrates through the outer electron cloud and then interacts with the inner shell electrons. If the energy transferred to inner shell electrons is higher than the critical amount of energy, then an electron is ejected leaving behind a hole in the inner shell. The atom is left in an excited state, which returns to its ground state by filling the hole with an electron from outer shell. This transition is accompanied by emission of an X-ray, which is specific to elements present in the system. The energy of emitted X-rays is characteristic of the difference in energy between the two electron shells involved. The

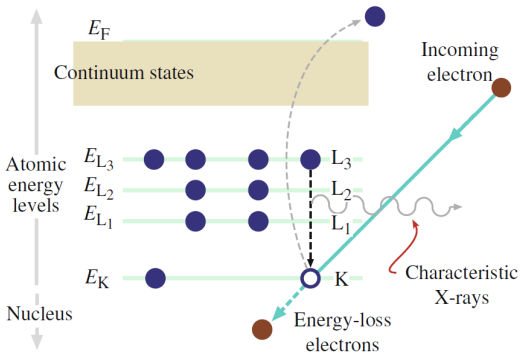

Figure 4.7: Schematic of an ionization process where an inner (K) shell electron is ejected from the atoms by a high energy electron leaving a hole behind. When this hole in K-shell is filled by an electron from outer L-shell electron, it produces characteristic (K_α) X-ray emission with an energy proportional to the energy difference between the 2 electrons shells.Taken from [60].

spectra obtained in this way contains different peaks, which represent the chemical elements and composition in the sample. Simultaneous recording of the X-ray signal with EDS and scattered electrons with bright-field(BF), HAADF STEM detectors leads to spectrum imaging where each pixel in the STEM image is associated with a EDS spectrum.

4.5.4 Off-axis electron holography

This section follows from [62,63]. The conventional TEM records the variation in the intensity of electrons but the phase information is lost. Off-axis electron holography is a technique that allows to recover the phase shift of the electrons that are passing through an electron transparent specimen in the TEM. The analysis of the phase can provide a high-spatial resolution information about local variations in electrostatic potential and magnetic flux density within and around the specimen.

When an electron with charge q = -e enters a magnetic field $\vec{B}$ and an electric field $\vec{E}$, it experiences the Lorentz force $\vec{F}$, which depends on the velocity of electron $\vec{v}$. $\vec{F}$ can be expressed as,

$$\vec{F} = -e(\vec{E} + \vec{v} \times \vec{B}) \tag{4.15}$$

To first approximation, the presence of an in-plane magnetic field B in a TEM sample of thickness t results in the small-angle deflection of an incident electron by an angle

$$\vartheta = \frac{e\lambda}{h} B_\perp t \tag{4.16}$$

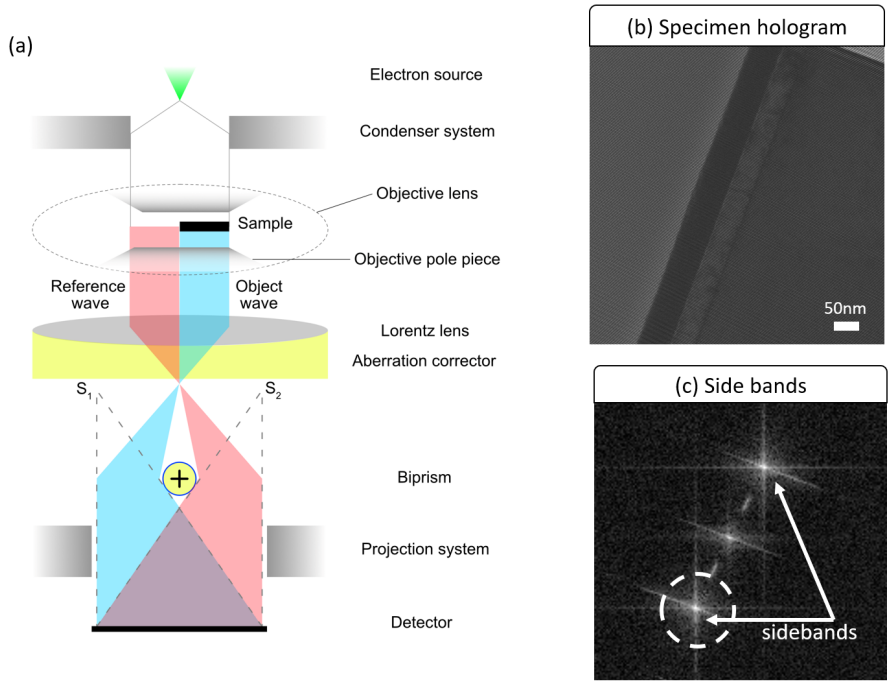

Figure 4.8: (a) Simplified schematic ray diagram of off-axis electron holography in TEM using single biprism. $S_{1,2}$ are the virtual sources of the electron hologram. Taken from [62]. **(b)** Electron hologram of the specimen and **(c)** its Fourier transform showing the side bands.

where λ is the (relativistic) wavelength of the electrons and h is the Planck's constant. For electrons that have been accelerated by 300 kV and pass through a specimen of thickness 100 nm that supports an in-plane magnetic induction of 1 T, the deflection angle is 47.6 μrad. For comparison, typical crystallographic Bragg angles in electron diffraction in the TEM are in the range of a few mrads. For coherent TEM imaging, the electron wave function in the image plane can be written as

$$\psi_i(\vec{r}) = A_i(\vec{r})exp[i\phi_i(\vec{r})] \tag{4.17}$$

where A and ϕ refers to amplitude and phase and subscript i refers to the image plane. The recorded intensity distribution is then given by expression

$$I_i(\vec{r}) = |A_i(\vec{r})|^2 \tag{4.18}$$

The phase contrast technique uses this deflection of the electrons by the magnetization of the sample. The off-axis electron holography records the phase of the electron

wave directly, based on the interference of the primary wave of interest with a reference wave (Fig. 4.8). It uses an electrostatic biprism to interfere an electron wave that passes through the sample (object wave) with another part of same electron wave that passes only through the vacuum (reference wave). A positive voltage is applied to a biprism to generate this interference pattern. The intensity distribution of the off-axis electron hologram can be written as

$$I_{hol}(\vec{r}) = |\psi_i(\vec{r}) + exp\left[2\pi i\vec{q_c}.\vec{r}\right]|^2 = 1 + A_i^2(\vec{r}) + 2A_i(\vec{r})\cos\left[2\pi\vec{q_c}.\vec{r} + \phi_i(\vec{r})\right] \quad (4.19)$$

where $\psi_i(\vec{r})$ is the electron wave function in image plane i with amplitude A_i and phase ϕ_i, $\vec{r}$ is a two-dimensional vector in the plane of the sample and the tilt of the reference wave is specified by a two-dimensional reciprocal space vector $\vec{q} = \vec{q_c}$. Eq.4.19 represents the three separate contributions to the intensity of an off-axis electron hologram: image intensity $A_i^2(\vec{r})$ and an additional set of cosinusoidal fringes, whose local phase shifts and amplitudes are exactly equivalent to the phase and amplitude of the electron wave function in the image plane, respectively.

The complex Fourier transform of a hologram gives the amplitude and the phase information and can be written as

$$\begin{array}{rll} FT\left[I_{hol}(\vec{r})\right] = & \delta(\vec{q}) + FT\left[A_i^2(\vec{r})\right] & \text{centerband} \\ & +\delta\left((\vec{q}) + (\vec{q_c})\right) \otimes FT\left[A_i(\vec{r})exp[i\phi_i(\vec{r})]\right] & -1 \text{ sideband} \\ & +\delta\left((\vec{q}) - (\vec{q_c})\right) \otimes FT\left[A_i(\vec{r})exp[-i\phi_i(\vec{r})]\right] & +1 \text{ sideband} \end{array} \quad (4.20)$$

It depicts 3 bands (fig. 4.8 c): the center band represents the conventional image and contains both elastically and inelastically scattered electrons but does not contain the image phase; the ± 1 side bands are of our interest as they contain the Fourier spectrum of the complete image wave and convoluted around $\vec{q} = \pm\vec{q_c}$, respectively. The two side bands contain only elastically scattered electrons and the amplitude and phase are linearly related to the object properties [64].

From the quantum mechanical description, the incident electron wave experiences a phase shift upon traveling though an electromagnetic potential that can be expressed (in 1D) as

$$\phi(x) = \phi_E + \phi_M = C_E \int V(x,z)dz - \frac{2\pi e}{h}\int A_z(x,z)dz \quad (4.21)$$

where the incident electron beam direction z is perpendicular to x, C_E is an interaction constant with a value of $6.53 \times 10^6\,\mathrm{radV^{-1}m^{-1}}$ at an accelerating voltage of 300 kV, V is the electrostatic potential and A_z is the component of magnetic vector potential along z. The magnetic vector potential $\vec{A}$ is related to the magnetic flux density by $\vec{B} = \nabla \times \vec{A}$. In the absence of long range charge redistribution and electrostatic fringing fields around the specimen, V mainly comprises of the mean inner potential (MIP) of the material V_0, which is dependent on its composition, density and ionicity. Taking MIP constant in the electron beam direction in the specimen with thickness t, the electrostatic contribution to the phase can be simplified to $\phi_E = C_E V_0 t$. the magnetic contribution to the phase can be written as

$$\phi_M = -\frac{2\pi e}{h} \oint A dl \tag{4.22}$$

where the integral is performed around a rectangular loop that is formed by two parallel electron trajectories crossing the sample and joined at infinity by segments perpendicular to their trajectories. different approaches can be employed to separate the magnetic and MIP contributions to the phase. In this work, the approach involves reversing the magnetization direction in the sample in-situ in the electron microscope and subsequently selecting the pairs of holograms that differ only in the opposite directions of the magnetization in the specimen. Thus, the magnetic contribution to the phase can be obtained by taking half of the difference between the two phase images. The in-situ magnetization reversal can be achieved by exciting the microscope objective lens and tilting the specimen to apply a precalibrated magnetic field [65].

5 Experimental techniques

5.1 Thin Film Growth

This section describes the different growth techniques employed to deposit $La_{0.7}Sr_{0.3}MnO_3$ (LSMO) and $BaTiO_3$ thin films on $Pb(Mg_{1/3}Nb_{2/3})_{0.7}Ti_{0.3}O_3$ (PMN-PT-(001)) and Nb doped $SrTiO_3$ (Nb:STO(001)) substrates, respectively. Different techniques used to characterize the thin film heterostructures structurally and magnetically are discussed here.

5.1.1 Oxide Molecular Beam Epitaxy - OMBE

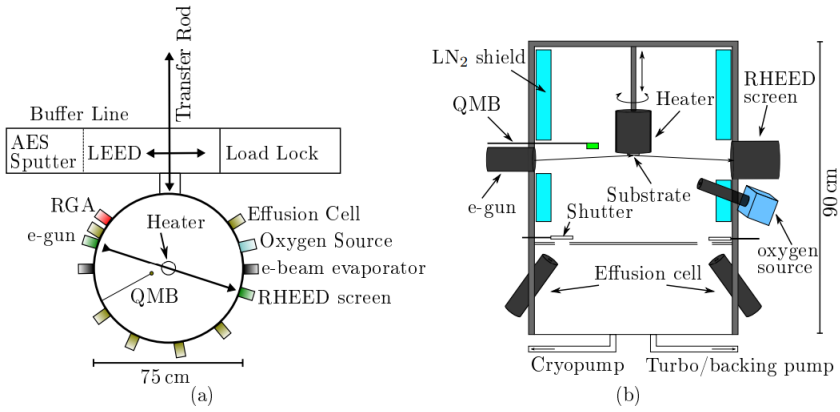

Figure 5.1: (a) Top view of the OMBE system showing load lock, buffer line and the main chamber (b) Cross-sectional view of the main chamber. Adapted from [66].

Oxide molecular beam epitaxy (OMBE) is a technique which gives a precise control on growth of stoichiometric thin films as well as facilitates the understanding of the nature of epitaxially grown oxide thin film at the atomic level [67]. OMBE uses ultra-high vacuum (UHV) environment to minimize the contamination of the growing layer. The beams of atoms or molecules impinge on the substrate that is kept at growth temperature (high temperature) to provide sufficient thermal energy for the incoming atoms to migrate over the surface to the lattice sites. Due to UHV, the atoms and molecules can travel in nearly collision-free paths until they arrive at

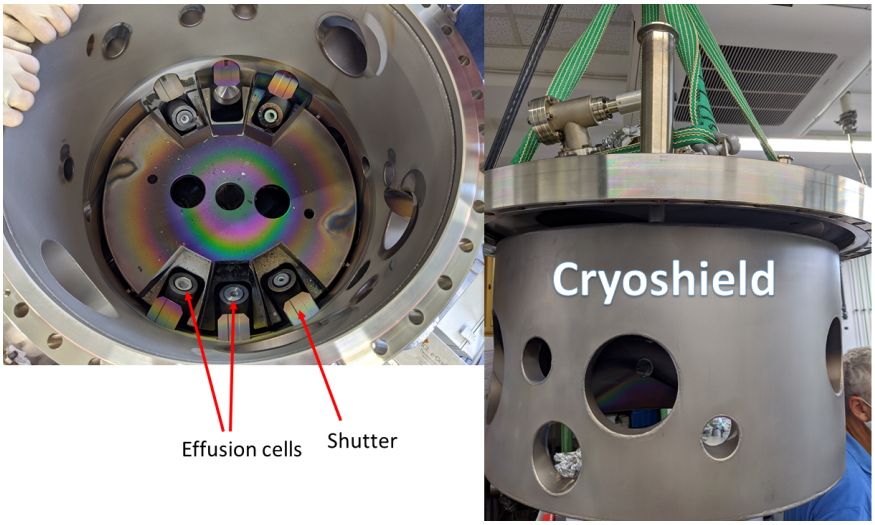

Figure 5.2: Inside view of Oxide Molecular Beam Epitaxy (OMBE) at JCNS-2, Forschungszentrum Jülich GmbH.

the substrate [68].

The OMBE system used is manufactured by DCA Instruments. It consists of three main parts: load lock, buffer line and main chamber as shown in fig. 5.1a. The substrate is first inserted in the load lock which is pumped with a combination of turbo pump and a scroll pump. There is a gate valve separating the load lock and buffer line which is open to transfer the substrate to buffer line. The buffer line and the connected auger electron spectroscopy (AES) are pumped by a turbo pump and an ion getter pump. There is another gate valve separating the main chamber and buffer line which is open to transfer the substrate to the main chamber using transfer rod. The heater shown in the fig. 5.1a is called 'main manipulator' which holds the substrate and regulates the temperature at the substrate position. A turbo pump with a scroll pump is used to maintain the vacuum in the main chamber. The base pressure of OMBE chamber is typically $1 \cdot 10^{-10}$ mbar. The main chamber is equipped with six effusion cells and two electron guns (e-gun). Each e-gun comprises of four crucibles. Since the effusion cells are heated to very high temperatures during deposition, the OMBE chamber is equipped with a cryo-shielding filled with liquid nitrogen to protect the chamber from the heat radiation of effusion cells and to reduce the contamination. Furthermore, the cryo-shield captures the atoms that do not hit the substrate and prevents uncontrolled backscattering.

For the growth of oxide thin films, an atomic oxygen source is installed and with the help of oxygen plasma directed towards the sample, the growing films are oxidized. The flux of the oxygen is controlled by a mass flow controller. Each effusion cell and e-gun is equipped with a shutter which is opened and closed according to the deposition requirement of the filled element. For the deposition of the film, rates are calibrated for each required element using quartz microbalance (QMB)

and adjusted by a proportional-integral-derivative (PID) controller to maintain stable fluxes. When some mass is deposited on this piezoelectric quartz crystal, the resonant frequency changes, which is used to determine the rate calibration. The rates are first calibrated roughly in the vacuum and then the oxygen plasma is turned on for final calibration of the rates. As the oxygen plasma is turned on the pressure rises to $5.3 \cdot 10^{-6}$ mbar. OMBE is also equipped with in-situ sample characterization techniques: RHEED and LEED which are discussed section 5.3.1 and 5.3.2.

5.1.2 High Oxygen Pressure Sputtering System - HOPSS

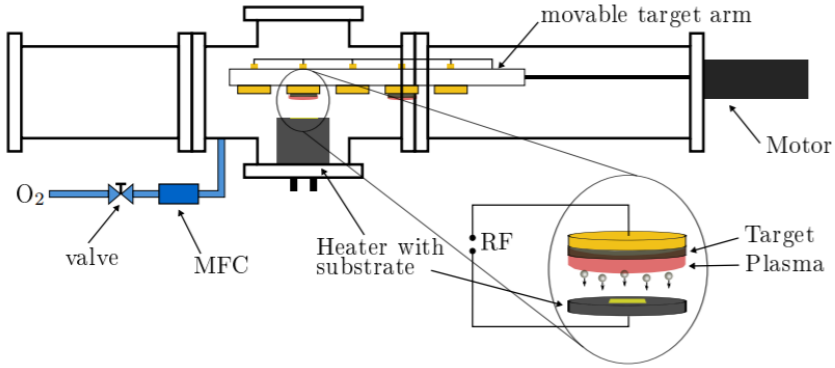

Figure 5.3: Schematic of high oxygen pressure sputtering system (HOPSS). Adapted from [66].

High oxygen pressure sputtering system (HOPSS) in another physical vapour deposition (PVD) technique used to grow oxide thin films. This technique uses RF power of frequency 13.56 MHz which is coupled to the target material. To start the sputtering process a base pressure of 10^{-6} mbar is required which can be reached by the turbo pump and a backing pump. Pure oxygen is used as a process gas to avoid oxygen deficiencies in the layer and the flow of oxygen is controlled by a mass flow controller. The target material used is commercially available from Kurt J.Lesker and the stoichiometry is pre-defined. A substrate is placed on the substrate heater which can be heated upto 1300 K. A movable target arm is installed to start and stop the sputtering by moving the target to substrate position. When the RF power is applied, the electrons start oscillating between the electrodes: cathode - target material and anode - substrate and ignites the oxygen plasma. These electrodes are connected with blocking capacitor which is a part of an impedance-matching network that facilitates the power transfer from the RF source to the plasma discharge. The ionized atoms from oxygen bombard the target, thereby ejecting the target atoms which are neutral but with the help of applied rf electric field, these ejected atoms are able to move and get deposited on the substrate. The HOPSS has a plasma generator with automatic tuning for igniting the oxygen plasma.

5.2 Comparison between OMBE and HOPSS

MBE and HOPSS, both are PVD techniques. MBE uses UHV conditions whereas HOPSS uses high vacuum (HV) conditions for deposition. This will affect the amount of impurity atoms during depositon. One can control the deposition rates with atomic precision in MBE and with RHEED system installed, it becomes possible for in-situ monitoring of the crystal growth process, while for HOPSS, no such system is present. MBE facilitates epitaxial deposition of thin films on crystalline substrates where one can play with the stoichiometry of the films easily as it uses effusion cells as a vapor source. Therefore, by controlling the growth rates, different stoichiometric thin films can be produced, which is not the case in HOPSS. Sputtering uses stoichiometric targets which are commercially prepared, thus it is not possible to play with the stoichiometry. The main drawback of MBE is the low deposition rates which leads to longer growth time compared to HOPSS for the same thickness of the film.

5.3 Structural characterization techniques

5.3.1 Reflection High Energy Electron Diffraction - RHEED

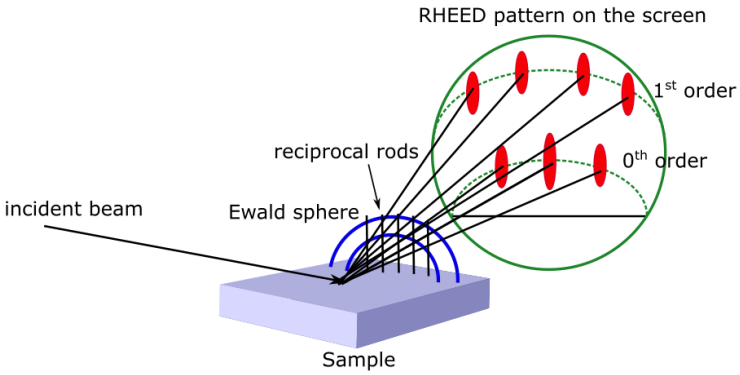

Figure 5.4: Schematic of RHEED scattering geometry.

RHEED is an important and very useful technique to determine the crystallinity, surface quality and the thickness of thin films during their growth and after the growth as well. The electron source emits the electrons of kinetic energy of 15 keV which impinge the sample surface under the grazing angles smaller than 2 °. Thus, the information obtained from the sample is highly surface sensitive. The electron beam striking the sample surface produces rod like pattern on the RHEED screen which originate from the 2D reciprocal lattice rods of the sample surface. RHEED

uses Ewald's sphere to analyze the crystallographic properties of a sample and the Ewald's sphere is centered on the sample with a radius equal to the magnitude of wave vector of incident electrons

$$k_i = \frac{2\pi}{\lambda} \tag{5.1}$$

with λ being the de-Broglie wavelength. When the rods of reciprocal lattice intersect the Ewald's sphere, the diffraction conditions are satisfied. However many reciprocal rods intersect the Ewald's sphere but due the geometry of RHEED system only the rods which are within the angular range of detector are projected onto the screen. Therefore, only low orders of diffraction are visible. In addition to this, one can also monitor the growth quality of the thin film during deposition by recording the RHEED intensity. This is only useful in the cases where the film grows layer-by-layer.

5.3.2 Low Energy Electron Diffraction - LEED

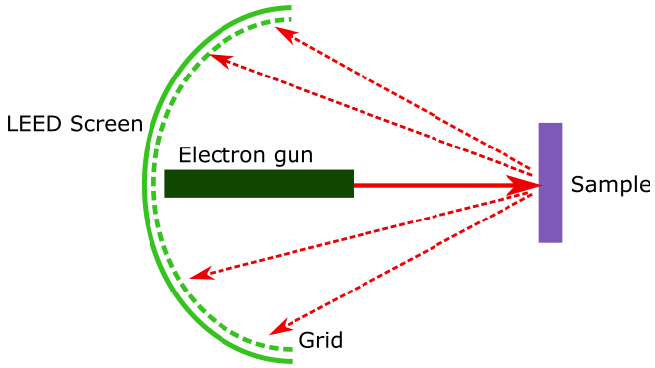

Figure 5.5: Schematic of LEED scattering geometry.

LEED is an another in-situ structural characterization technique used for surface structure analysis. It uses low energy electrons of energy range 20-500 eV which are bombarded onto the sample surface with normal incidence. The de-Broglie wavelength λ of low energy electrons is in the range of 0.05-0.3 nm and can be calculated by $\lambda[\text{Å}] = \sqrt{150.4/E[eV]}$. Since the mean free path of low energy electrons is of the order of a few atomic layers, the diffraction occurs from the very top layers only. LEED also uses Ewald's sphere construction for determining the crystallogrpahic properties. The diffracted beam produces the spots where the reciprocal rods intersect the Ewald's sphere. These LEED spots are the 2-dimensional projection of surface reciprocal lattices which are deduced from the atomic arrangement of the surface [69]. The LEED geometric set-up is shown in fig.5.5. The electron gun produces electrons by thermionic emission from a hot filament. This electron beam passes through a Wehnelt cylinder followed by an electrostatic lens which accelerates and collimates the beam normal to the sample surface. After the backscattering from the sample occurs, the electrons pass through a retarding grid, which acts as

an energy filter removing inelastically scattered electrons from the spectrum.

5.3.3 X-ray Reflectometer -XRR and X-ray Diffraction -XRD

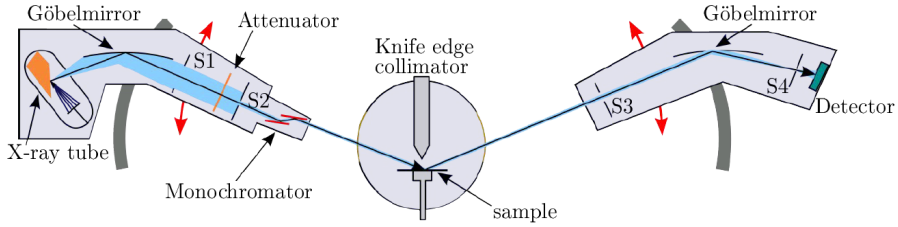

Figure 5.6: Schematic of Bruker D8 Advanced X-ray reflectometer. Taken from [70].

The Bruker D8 Advanced X-ray reflectometer has been used in reflectometry and diffraction mode to characterize the thin films structurally. The system has Cu X-ray source, where the Cu $K_{\alpha 1}$ radiation of wavelength of 1.54 Å is selected and collimated with a Göbel mirror, a slit system and a channel cut monochromator. With this geometry only out-of-plane components of crystalline films are accessible. In the reflectometer mode, one can measure the film thickness and the laterally averaged roughness of the film and in diffractometer mode, the crystallinity and the out-of-plane lattice lattice parameters can be measured.

5.3.4 Grazing Incidence Small Angle X-ray Scattering - GISAXS

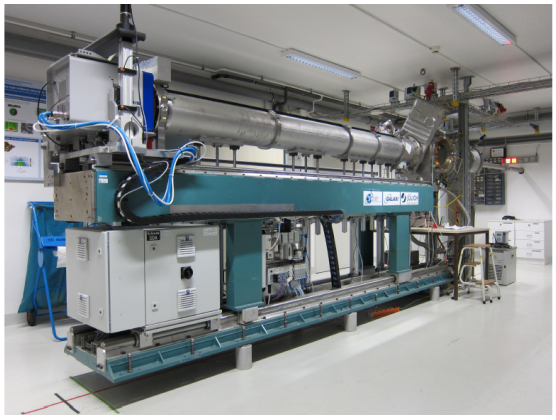

Figure 5.7: GALAXI diffractometer for GISAXS and XRR measurements. Taken from [71].

Gallium anode low-angle x-ray instrument (GALAXI) uses the METALJET source built by Bruker AXS and this X-ray source utilizes a liquid metal jet of a GaInSn

alloy as anode. When an electron beam of 20 μm height $\times$ 80 μm width at 70 keV energy with 200 W power hits the liquid metal jet, the X-rays are produced. It utilizes parabolic Montel-type optics to parallelize and monochromatize the beam. The collimation and the size of the beam at the sample position is defined by the two 4-segment slits separated by a distance of 4 m and the flux of $1 \cdot 10^9$ photon/mm^2.s is obtained at exit point of the source. At sample stage, the sample can be adjusted by two rotational and two translational degrees of freedom. There is a second sample holder that contains reference sample for calibration purposes. The detector distance can be adjusted between 835 mm and 3535 mm in 5 steps. The flight path is fully evacuated between the X-rays and the detector and a Pilatus 1M 2D position sensitive detector with 169 $\times$ 179 mm^2 active area is used for detecting the X-rays [71]. GISAXS was performed on the LSMO/PMN-PT samples before and after the voltage in order to investigate the presence of any lateral correlations as a function of voltage. The diffractometer was used to perform the reflectivity from the heterostructures and since one can measure larger Q-range, the layer thickness and interfacial profile was determined.

5.3.5 Atomic Force Microscopy - AFM

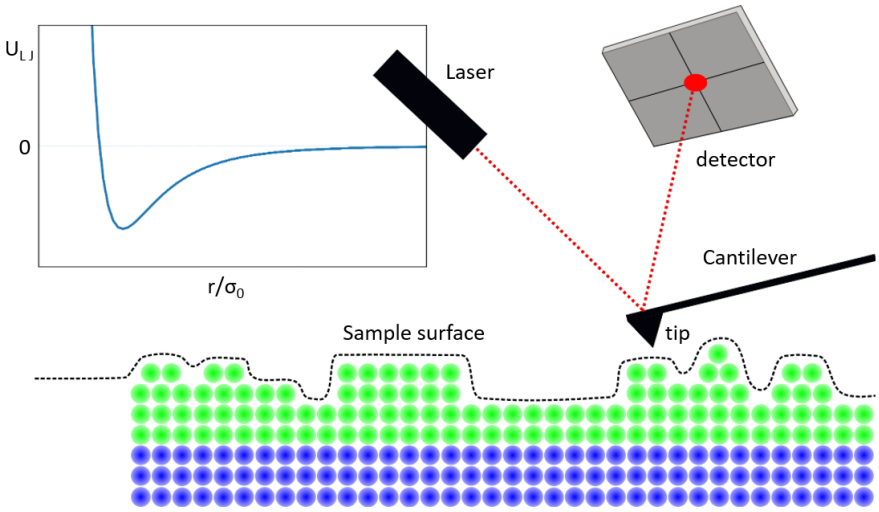

Figure 5.8: (a) Schematic of AFM technique. Taken from [66]. **(b)** Lennard-Jones potential qualitatively depicts the interaction between the tip of the cantilever and the surface atoms in AFM. σ_0 refers to the characteristic length and U_{LJ} is the potential in arbitrary units. Adapted from [72].

AFM is a scanning probe microscopy which gathers information based on 'feeling' or 'touching' the sample surface, depending on the mode in use. It measures short range chemical forces and long range Van der Waals and electrostatic forces with the help of a cantilever. This cantilever has a tip and both cantilever and tip are

sensitive to these forces and measures the forces existing between the tip and the sample based on a tip-sample spring constant. Here we use a non-contact mode in which the sample is scanned in x-y directions with the cantilever placed close enough to the sample surface that it is able to measure the tip-sample force F_{ts} directly. F_{ts} is the derivative of electrostatic potential between the tip and the sample $F_{ts} = \frac{\partial V_{ts}}{\partial z}$ resulting in the deflection and oscillation of the cantilever. There is a feedback loop system which maintains the constant oscillation amplitude by adjusting the tip to sample distance Δz. The scanning software records the relative displacement Δz and constructs a topographic image of the sample surface [73]. The Lennard-Jones potential is a good approximation for a qualitative description of the tip-sample interaction in AFM. In this work for topographic analysis an Agilent Technologies 5400 Atomic Force Microscope (JCNS-2) and Asylum Research Cypher SPM (PGI-6) has been used. Fig.5.8 depicts how the amplitude is measured from a deflection of a laser beam. The change in amplitude occurs due to interaction between the surface atoms and the tip atoms. One can get the height profile and the sample roughness.

5.3.6 Piezoresponse Force Microscopy -PFM

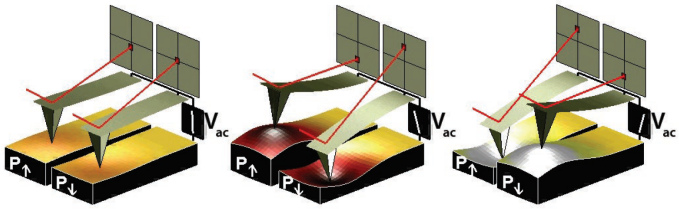

Figure 5.9: Sign dependence of the sample strain in PFM with the application of bias. Taken from [74].

PFM is another type of scanning probe microscopy which records the mechanical response of a sample on application of electrical voltage via conductive tip. It is a contact mode AFM. It is an useful technique for the characterization of ferroelectric materials. On applying the voltage, the conductive tip deflects based on the direction of the polarization below the tip. The polarization parallel and aligned with the electric field ($P \uparrow E \uparrow$) will results in positive piezo effect causing local expansion of the sample and if the polarization is anti-parallel with the applied electric field ($P \downarrow E \uparrow$) will produce local contraction of the sample with negative piezo effect. This sign dependent behavior can be deduced from the phase image where the phase of cantilever gives access to the polarization orientation, phase $\varphi = 0°$ (in-phase) and $\varphi = 180°$ (out-of-phase). There are different modes in PFM as described. **Vertical mode**: gives information about out-of-plane polarization. **Lateral mode**: in-plane component of polarization can me measured as lateral motion of the cantilever caused by the bias-induced surface shearing. **Lithography mode**: one can modify the ferroelectric polarization of the sample and can induce ferroelectric polarization reversal on achieving the local coercive field and make patterns without changing the surface topography [74].PFM measurements were performed using the

PFM mode in Asylum Research Cypher SPM from PGI-6.

5.4 Magnetometry measurements - MPMS

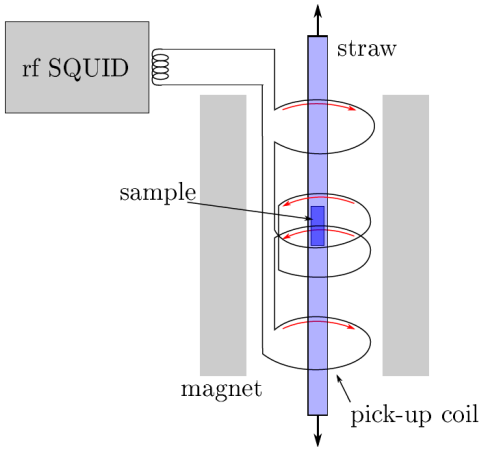

Figure 5.10: Schematic of MPMS set-up. Taken from [66].

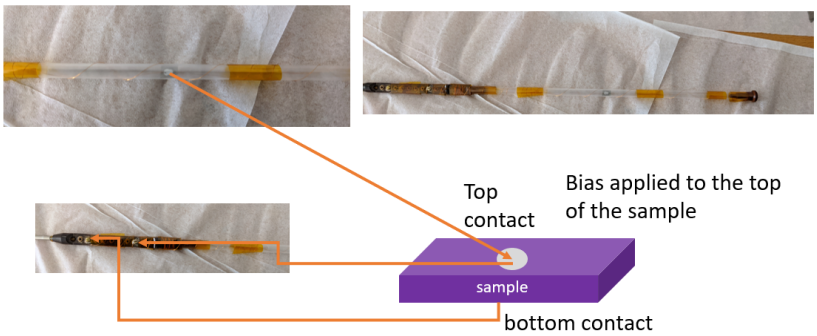

Figure 5.11: DC conductive rod mounted with the sample having top and bottom contacts. The bias is applied to the top of the sample.

The magnetometry measurements are performed using a Quantum Design Magnetic Property Measurement System (MPMS). MPMS uses a superconducting magnet to generate large magnetic fields and can go upto 7 T. There is a superconducting pick-up coil which is inductively coupled to the sample and to a rf SQUID. When performing a measurement in MPMS, the sample moves through these superconducting pick-up coils and the magnetic moment of the sample generates an electric current in the pick-up coils. The pick-up coils, connecting wires and the SQUID form a closed superconducting loop. Thus, when the magnetic flux changes in pick-up coils, it produces a change in the persistent current in the detection circuit which

is proportional to the change in magnetic flux. Since SQUID is extremely sensitive to the fluctuations in magnetic fields, the sensors have to be shielded from both, the fluctuations in ambient magnetic field of the laboratory and from the large magnetic fields produced by the superconducting magnetic [75]. Due to this, the whole set-up is installed in dewar and is constantly kept under liquid Helium to maintain the superconducting behaviour of the superconducting coils. The sample temperature can be chosen between 1.9 K to 400 K. The MPMS achieves a sensitivity of approximately 10^{-12} Am^2.

The sample is mounted in a drinking straw which is longer than the extension of pick-up coils and also, it does not induce any signal for pick-up coils. The Reciprocating Sample Option (RSO) is used as the sample transport mode. It is quite sensitive to even a small magnetic moments and offers good noise rejection.

For performing magnetoelectric measurements, DC option is used with a modified design based on Borisov 's set-up [76] implemented by Dr.Oleg Petracic and Dr.Liming.M. Wang. With this DC rod one can apply electric fields to the sample using conductive wires from a power supply. According to initial design a Vespel rod was used for sample mounting but due to strong background signal, Vespel rod is replaced by a drinking straw. Top and bottom contacts are made on the sample using Ag paste and then copper wires are attached to each contact. The sample is inserted carefully in the straw which is then connected to the conductive sample rod. The DC option uses a stepper motor to move the sample gradually through the pick-up coils. The maximum voltage that can be applied with this set-up is ±200 V.

5.5 Rutherford Backscattering Spectrometry - RBS

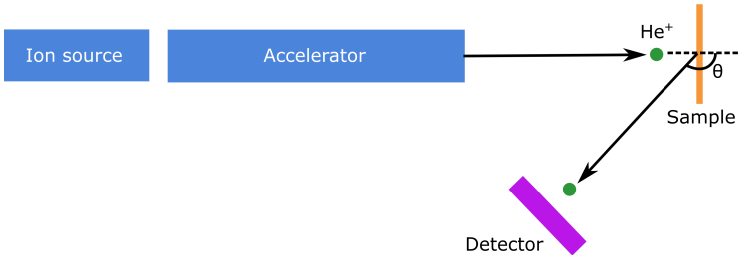

Figure 5.12: Schematic of RBS experiment.

Rutherford backscattering spectrometry (RBS) is an ion scattering technique used to determine the stoichiometry of the thin films. It is a representation of the electrostatic repulsion between high energy incident ions and the target nuclei. An RBS set-up has 3 essential components: an ion source, a linear particle accelerator for accelerating the incident ions to high energies and a detector for recording the energies of backscattered ions. An ion source produces light Helium ions which are then accelerated by the particle accelerator and are bombarded towards the sample. During this event of collision, transfer of energy occurs between the incident

particle and the target atoms and the change in energy of backscattered Helium ions under scattering angle θ depends on the masses of the involved particles in the sample. The resulting energies of backscattered particles are element specific and thus can be used to deduce the stoichiometry of the thin films. The energy E_1 of the backscattered ions after the scattering process can be written as:

$$E_1 = K^2 E_0 \tag{5.2}$$

where E_0 is the initial energy and the K kinematic factor can be written as

$$K = \frac{M_1^2}{(M_1 + M_2)^2} \left\{ \cos\theta \pm \left[\left(\frac{M_2}{M_1} \right) - \sin^2\theta \right]^{1/2} \right\}^2 \tag{5.3}$$

where M_1 is the mass of Helium ion and M_2 is the mass of target atoms, θ is the scattering angle. For $M_1 < M_2$ plus sign applies and for $M_1 > M_2$ minus sign applies [77].It is a non-destructive technique. The data is analyzed using RUMP [78] software package by Dr. Jürgen Schubert from PGI-9. The error of the measurement lies within a few percent and depends on the element of the scattering atoms.

5.6 Scanning transmission electron microscopy (STEM)

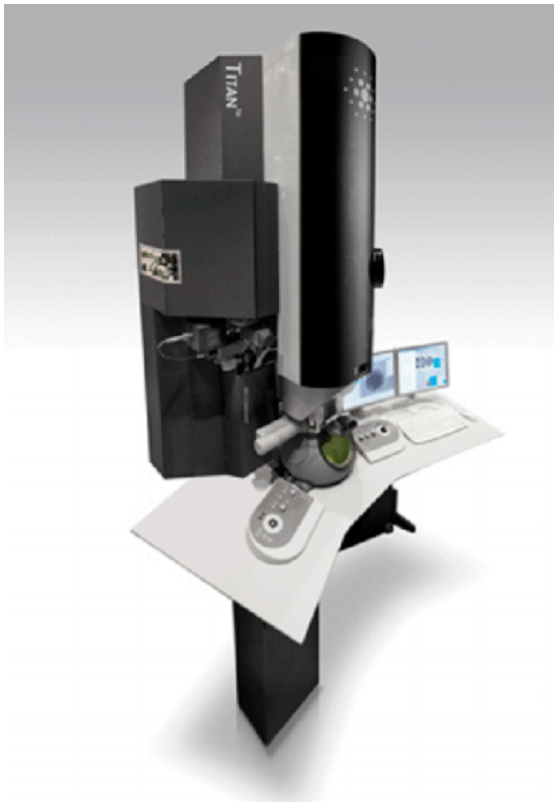

Figure 5.13: FEI Titan G2 80-200 ChemiSTEM used to perform structural and chemical analysis. Taken from [79].

STEM is a method to probe structural and chemical properties of the sample. The measurements were performed at ER-C-1 with Dr. Qianqian Lan and Dr. Lei Jin at FEI Titan G2 80-200 ChemiSTEM [79]. It is equipped with a Schottky type high-brightness electron gun, a Cs probe corrector, an in-column Super-X energy dispersive X-ray spectroscopy (EDS) and a post-column energy filter system with dual electron energy loss spectroscopy option. HAADF STEM was performed on LSMO/PMN-PT(001) heterostructures to investigate the structural properties and elemental mapping was recorded using EDS. These measurement helped in resolving the interface between LSMO and PMN-PT(001). With EDS, different regions of interest were chosen to compare the element concentrations. HAADF-STEM is highly sensitive to the atomic number $|Z|$ of atoms in the sample and thus, one obtains Z-contrast images.

5.7 Polarized Beam Reflectometer -PBR

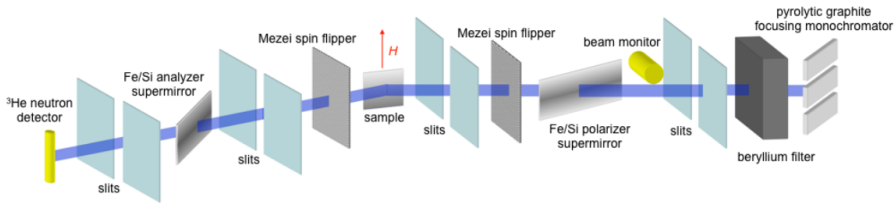

Figure 5.14: Schematic of PBR experimental set-up. Taken from [80]

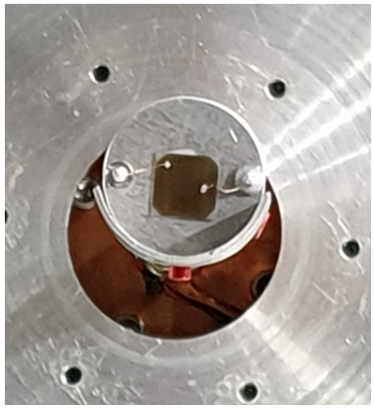

Figure 5.15: Sample holder used at PBR for applying voltage. Thin platinum wires and silver paste was used to make the contacts.

Polarized Neutron Reflectometry measurements were performed at NCNR, NIST, USA with PBR instrument. The instrument set-up is depicted in fig.5.14. The wavelength used for measurements was 4.75Å with $\frac{\Delta\lambda}{\lambda} = 0.03$. PBR uses a pyrolytic graphite as a focusing monochromator, a beryllium filter to suppress the $\lambda/2$ contamination, a supermirror to polarize the beam and a spin-flipper to flip the neutron spin. For collimation of beam, slit systems are used. There is a special sample holder for applying voltage to the sample and the sample environment is equipped with a closed cycle cryostat which can measure in the range of 10 K to 330 K and the magnetic fields parallel to the sample surface upto 0.75 T. There is a second flipper and a supermirror for performing polarization analysis. PBR uses ^3He pencil detector for detecting the scattered neutrons.

5.8 Combination of neutron scattering and electron microscopy techniques

This thesis focuses on investigation of magnetic and structural properties of oxide heterostructures by using a combination of advanced neutron scattering and electron microscopy methods. With neutrons as a probe, it is possible to study light elements like hydrogen and oxygen, which is difficult to probe with electrons. However, electron microscopy gives access to the localized real space atomic information, whereas, with neutron scattering, the information is averaged over complete sample. By using both techniques in complementarity, one can obtain a detailed information of the probed system. In this thesis PNR experiments helped to obtain magnetic depth profile of LSMO/PMN-PT(001) heterostructures which revealed the presence of an interlayer with reduced nuclear scattering length density (NSLD) and magnetic scattering length density (MSLD). To examine this interlayer, it becomes crucial to get information at microscopic level. STEM and EDS experiments were performed to understand the structure as well as stoichiometric fluctuations in this interlayer, which in turn explained the reduced magnetization and NSLD in PNR. In addition, with off-axis electron holography, it was possible to directly measure the phase shift of the incoming electron wave and to facilitate a direct comparison between magnetization profile and the real-space structure. A combination of all these advanced techniques provides a comprehensive picture of the magnetization profile of LSMO/PMN-PT(001) heterostructures.

6 Experimental results I: $La_{0.7}Sr_{0.3}MnO_3$ on PMN-PT (001)

This chapter discusses about the magnetoelectric (ME) effect in LSMO/PMN-PT(001) heterostructures. The samples were produced using OMBE and were further characterized structurally and magnetically using different techniques. The results reveal that different mechanisms play a role in the ME coupling in this heterostructure. Major parts of this chapter are included in an article published in New Journal of Physics [81]. All measurements included in the article were performed and analyzed by the author of this thesis apart from TEM images (analysis of TEM measurements were performed by the author). The manuscript was written by the author.

6.1 Sample growth and structural analysis

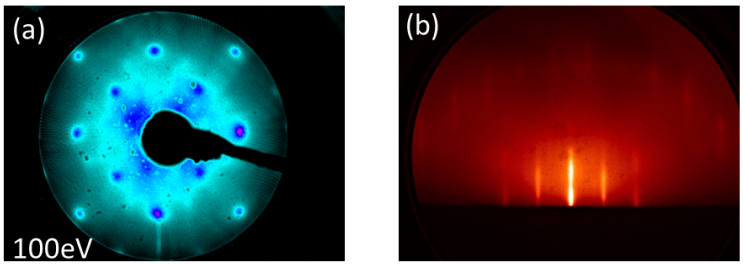

Figure 6.1: In-situ structural characterizations **(a)** LEED and **(b)** RHEED pattern of $La_{0.7}Sr_{0.3}MnO_3$ film on PMN-PT (001) substrate.

The LSMO layers are deposited on PMN-PT(001) substrate using OMBE. The PMN-PT single crystal substrates (Crystal GmbH) are pre-treated with ethanol and acetone and then annealed at 730° C for 5400 s in oxygen atmosphere. The growth rates of individual elements La, Sr and Mn are first calibrated in the vacuum and then again in oxygen atmosphere. Co-deposition method is used for the growth of LSMO layers and the deposition takes place at 730° C under a pressure of 5.8×10^{-6} mbar with an oxygen flow of 0.15 sccm for 6450 s. The sample is post-annealed at 200° C for 1800 s and then cooled to room temperature. The frequency change for each element is tabulated in table.S3. The $La_{0.7}Sr_{0.3}MnO_3$ growth parameters are taken from Markus Waschk's thesis work [66]. Fig.6.1 shows the LEED

and RHEED pattern recorded after the deposition of LSMO layer, depicting the good crystalline quality of the sample with no surface reconstruction as seen from the LEED image. The presence of Laue spots with sharp RHEED spots indicate a smooth surface of the film.

Element	Temperature [°C]	Frequency change [Hz/s]
La	1501	-0.11
Sr	484	-0.038
Mn	791.2	-0.091

Table 6.1: Growth rates used for LSMO deposition on PMN-PT(001).

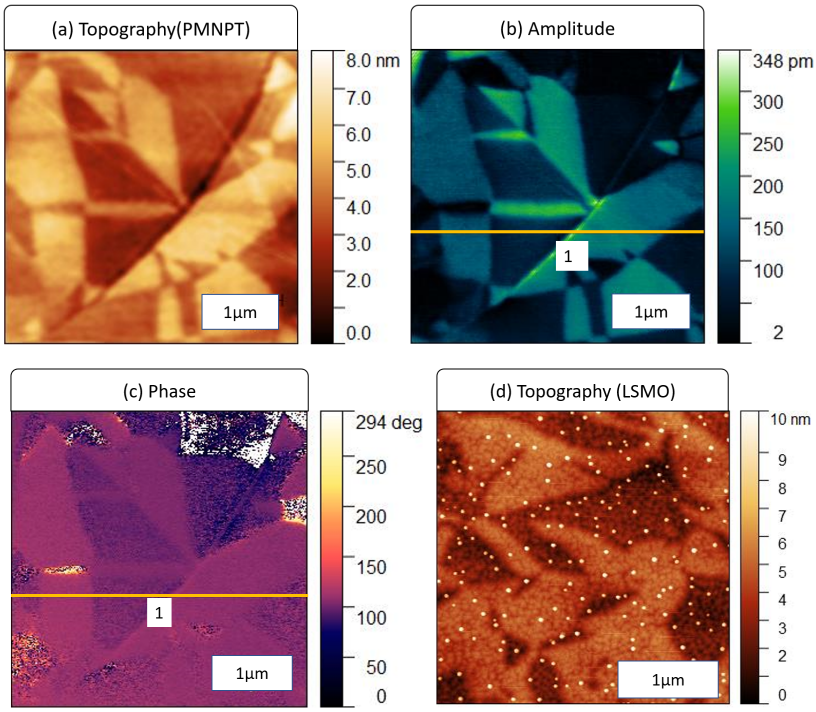

Figure 6.2: PFM images of bare PMN-PT (001) substrate **(a)** Topography, **(b)** amplitude and **(c)** phase shows the presence of FE domains. **(d)** Topographic image after deposition of LSMO layer showing excess of Mn crystallized on the top the film.

The bare PMN-PT(001) substrate is first probed using PFM shown in fig.6.2, which depicts the topographic, amplitude and phase scans of the substrate. The amplitude and phase image provides the information on the strength of the signal and the direction of polarization in PMN-PT(001), respectively. The root mean square (RMS) roughness, σ_{RMS} from the topography signal is calculated using

$$\sigma_{RMS} = \sqrt{\Sigma_{n=0}^{N} \frac{(z_i - z_0)^2}{N}} \tag{6.1}$$

where z_i and z_0 are the local height and the mean height at position i, respectively. For the estimation of roughness error, the standard deviations of four quadrants are calculated from the measurement. The topographic signal gives $\sigma_{RMS} = 11.3 \pm 0.9$Å for bare PMN-PT(001).

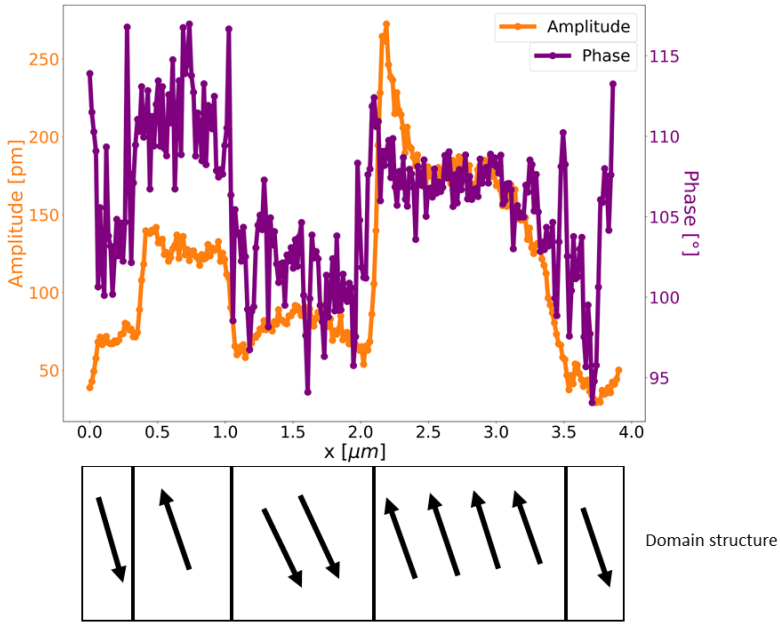

Figure 6.3: Line cut profile from fig. 6.2(b) and (c) demonstrating the change in amplitude with respect to domain structure.

A line cut is performed across the amplitude and phase image to understand the domain structure. In PFM, the cantilever is in contact mode and based on the piezo-response of the material, the signal gets recorded. The expansion and contraction of FE domains in PMN-PT result in the positive and negative piezo-reponse. The polarization switching in PMN-PT (001) can occur along [111] direction and here, one measures piezo-response along [001] .Therefore, what one observes from the line cut plot is the out-of-plane component of polarization vector pointing upwards, causing increase in amplitude and the polarization vector pointing downwards resulting in decrease of amplitude. The amplitude goes down at the domain boundaries. Fig.6.2(d) shows the topography after deposition of LSMO film on PMN-PT(001). The FE domains are still visible, however there is presence of small particles which is probably indicating a slight excess of Mn crystallized on the surface of LSMO. Such effect was observed by Alexandra Steffens also in her thesis work [82]. The topographic signal gives $\sigma_{RMS} = 12.9 \pm 0.7$Å for LSMO film.

The crystalline nature of as-grown LSMO film is probed by X-ray diffraction which demonstrates single crystalline growth of the film along [001] direction. LSMO ($a = 3.876$Å)and PMN-PT ($a = 4.02$Å) has in-plane lattice mismatch of +3.5%, thus LSMO experiences in-plane tensile strain. This results in reduction of out-of-plane lattice parameter c of LSMO. The experimental value is found to be $c_{LSMO} = 3.82$Å which is 1.3% lower than the bulk value. However, this reflects to the fact that LSMO is partially relaxed. Since, the bulk of the film has $c_{LSMO} = 3.82$Å, one can calculate the in-plane lattice parameter from the volume of LSMO, $a = 3.904$Å. Therefore, the bulk of the film retains an in-plane tensile strain of 0.7%. Fig.6.5 shows that with increase of film thickness above $\sim$ 30-40 Å, the film starts relaxing by forming defects (yellow structure). The formation of dislocation is evident from the insertion of an extra half atomic plane. The LSMO thickness deduced from x-ray reflectometry measurements is $295^{+4.4}_{-3.6}$Å. A top layer with reduced scattering length density (SLD) and thickness of $27.9^{+2.6}_{-2.7}$Å had to be taken into account to get the best fitting model.

To determine the stoichiometry, the LSMO film is deposited on MgO substrate. MgO is chosen because Mg and O are lighter than La, Sr and Mn, i.e. their contribution to RBS spectrum is at lower energy than the film peaks. The stoichiometry of the as-deposited LSMO film is confirmed with RBS measurement shown in fig.6.6. The composition can be determined as $La_{0.7}Sr_{0.3}Mn_1O_{3-\delta}$. As one can see from the data, the Mn peak is a bit broad and the fit only matches the data if one substitutes half the Mn signal with Fe, which is not possible as Fe was not used for the deposition. Therefore, this peak broadening is taken as an artifact from the measurement. The ratio between La:Sr fits well with the expected ratio. Thus, the stoichiometry is confirmed within the measurement error of 5%.

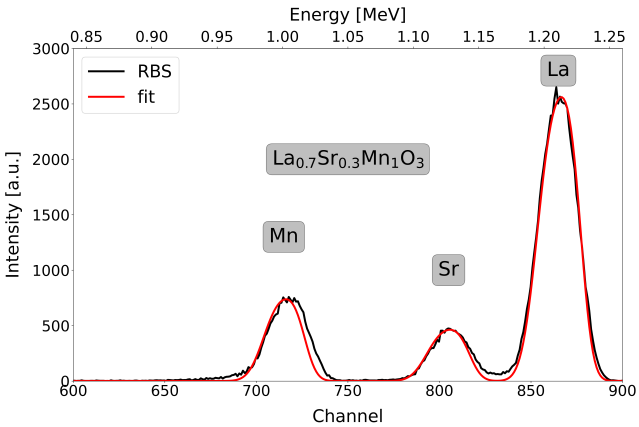

Figure 6.6: RBS data and simulation for LSMO film deposited on MgO.

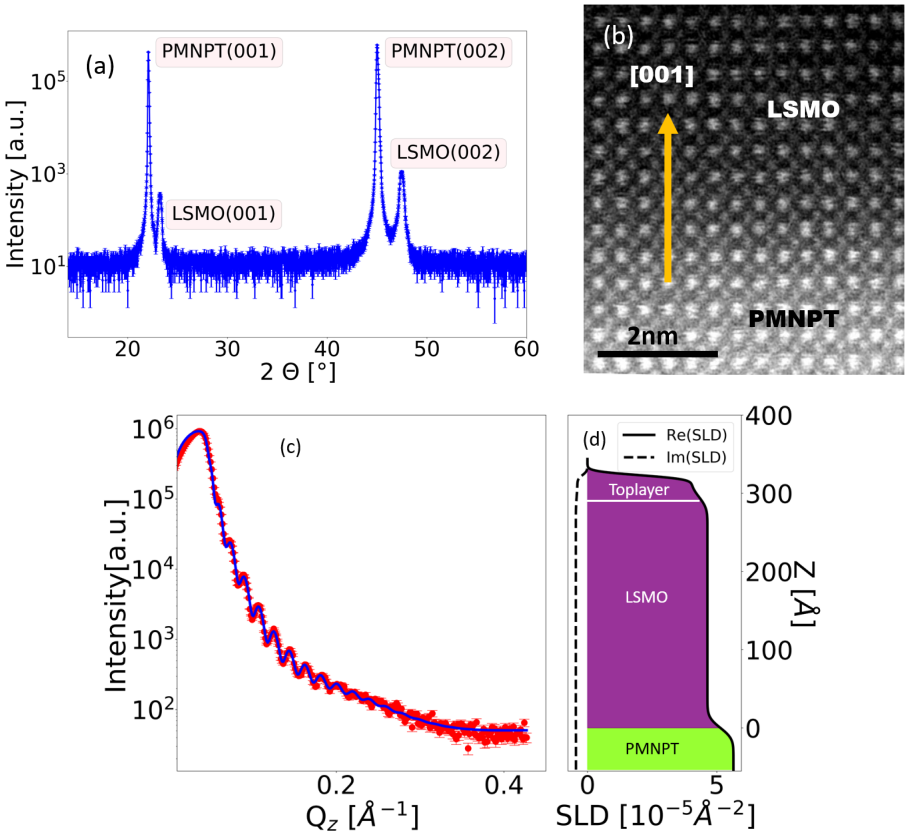

Figure 6.4: The crystallinity of the as-grown LSMO/PMN-PT(001) heterostructure is determined by **(a)** X-ray diffraction , **(b)** HAADF-STEM image shows the epitaxial growth of LSMO on PMN-PT viewed along [001], **(c)** the thickness and roughness of the film is determined by XRR measurement and **(d)** Scattering length density (SLD) profile of the sample. The XRR fitting parameters are mentioned in supplementary material in table. S4.

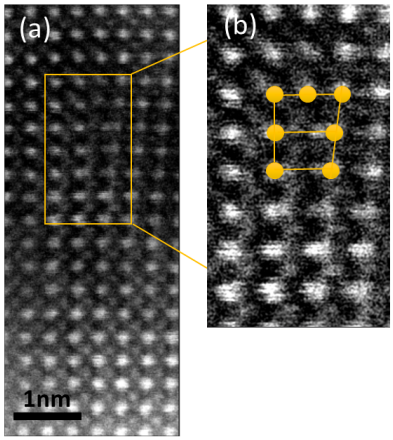

Figure 6.5: Formation of a dislocation in LSMO away from the interface.

6.2 Macroscopic magnetization measurements

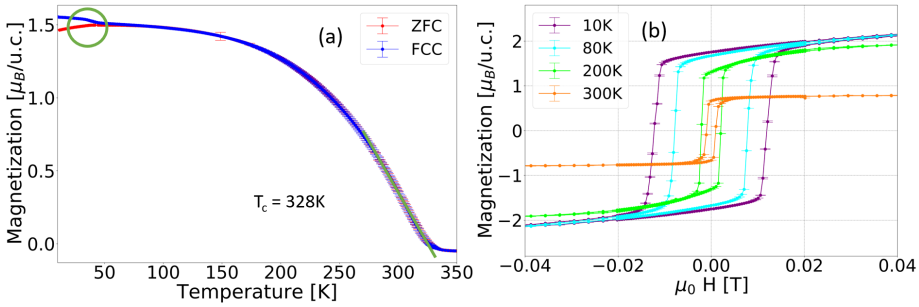

Figure 6.7: (a) Magnetization vs temperature curves for 300Å LSMO film on PMN-PT(001) and **(b)** magnetization hysteresis measurements as a function of temperature.

The macroscopic magnetic properties of LSMO/PMN-PT(001) are probed with RSO option of MPMS. The magnetization of LSMO is recorded as a function of temperature with an applied field of $\mu_0 H = 50\,\mathrm{mT}$. The magnetic field is applied along [100] direction, parallel to the sample. The cooling and warming cycles are performed at the temperature rate of 2 K/min. One observes a kink in magnetization in field cooled-cooling (FCC) and zero field-cooling (ZFC) curves around $\sim 50\,\mathrm{K}$ which indicates the appearance of new magnetic phase. Since PMN-PT and LSMO do not have any structural or magnetic phase transition in this temperature regime, therefore their contribution to this kink can be ruled out. This is discussed later in detail. The Curie temperature obtained for LSMO is $T_c = 328\,\mathrm{K}$ and the magnetization above T_c becomes negative due to the diamagnetic contribution from the substrate. The magnetization as a function of applied magnetic field at different temperatures is depicted in fig.6.7b showing a stable ferromagnetic state of LSMO. Even with large lattice mismatch between the film and the substrate, good quality LSMO thin film were achieved successfully.

6.2.1 Magnetoelectric measurements

After confirming the magnetic and structural properties, the influence of electric field on magnetism of LSMO is probed. For these measurements, a special set-up with DC rod having electrical contacts is used to measure the magnetoelectric (ME) properties by MPMS-SQUID. This set-up is explained section 5.4. For an uniform application of voltage, a Au layer is deposited to serve as a bottom electrode and LSMO works as top electrode. The final structure is depicted in fig.6.8.

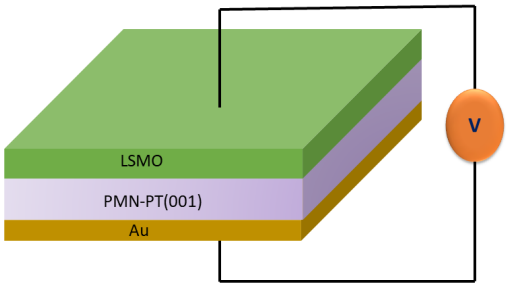

Figure 6.8: Schematic of final LSMO/PMN-PT(001) heterostructure.

6.2.2 Temperature dependent ME coupling

LSMO is an heteroepitaxially grown thin film and since LSMO and PMN-PT have misfit strain of +3.5%, the film is biaxially strained. This misfit strain does not affect the Mn-O bond length but results in the alteration of Mn-O-Mn bond angle responsible for double exchange interaction in LSMO [83]. The change of Mn-O-Mn bond angle affects the electron hopping probability as, according to Hubbard model the hopping probability t depends on the bond angle θ via $t = t_0 \cos(\pi - \theta)^2$, where t_0 is the value of hopping for an undistorted 180° Mn-O-Mn straight bond [84]. Therefore, when LSMO is deposited on PMN-PT, it experiences in-plane tensile strain which leads to distortion and reduction in the bond angles between Mn-O-Mn, which further modifies the exchange interaction thereby altering the electronic and magnetic properties: destabilizes the ferromagnetism. However, on applying voltage, PMN-PT experiences in-plane compressive strain which when transferred to LSMO, results in increasing of Mn-O-Mn bond angle, going towards 180° and thus stabilizes the ferromagnetism. The asymmetry in butterfly loop occurs due to influence of FE polarization switching effect which becomes much more visible when the measurements are made in remanent magnetic field. One has to note that the results observed in fig.6.9 depict the effect on magnetization as a function of both magnetic field and electric field. This means the magnetic moments in LSMO follow both electric and magnetic field.

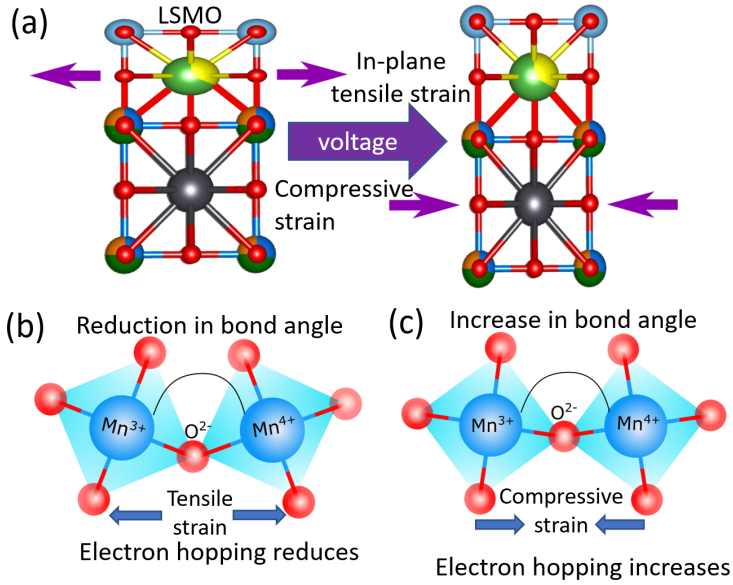

Figure 6.9: Schematic of strain-mediated magnetoelectric coupling in LSMO/PMN-PT(001).

Fig. 6.10 shows the ME coupling observed at 300 K and 80 K. The magnetic field of 10 mT and 50 mT is applied along [100] direction and the electric field is applied along [001] direction. The electric field is applied in the following loop: 0 kV/cm $\rightarrow$ +4 kV/cm $\rightarrow$ 0 kV/cm $\rightarrow$ -4 kV/cm $\rightarrow$ 0 kV/cm and the magnetization is recorded for 6 loops. An asymmetric butterfly loop is observed at 300 K. A butterfly loop is characteristic of strain-mediated ME coupling [46]. However, the asymmetry of this loop indicates the presence of another effect also. There is a difference $\sim$ 2% between the magnetization values obtained for $\pm$V and the cross-over point is shifted to +1kV/cm. At low temperature, 80 K one observes a linear behavior of ME coupling: magnetization increases for -4 kV/cm and decreases for +4 kV/cm. The magnetization is normalized to $\mu_B/u.c.$ by measuring the deposited area and the thickness of the film, leading to a systematic error of about 4% for the absolute value of the magnetization. The statistical error is several orders of magnitude smaller than the magnetization value.

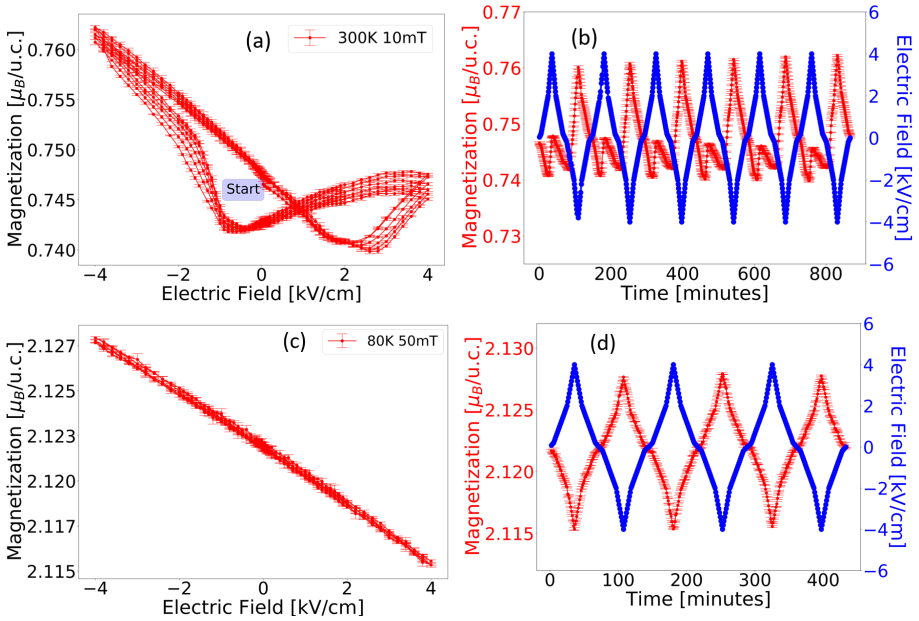

Figure 6.10: **(a)** Magnetization vs electric field **(b)** magnetization and electric field as a function of time at T=300 K with $\mu_0 H = 10$ mT, **(c)** magnetization vs electric field and **(d)** magnetization and electric field as a function of time at T=80 K with $\mu_0 H = 50$ mT.

The piezoelectric strains are significantly reduced at low temperatures resulting in hardening of polarization rotation [85]. Also, the electric coercive field 'E$_c$' is very high and the FE polarization cannot be switched with this small amount of electric field. Although the polarization in PMN-PT cannot rotate but is still produces strain in the system under applied electric field. For these measurements at 80 K, the sample is already poled with negatively bias voltage from the last voltage cycle at 300 K resulting in polarization pointing upwards as shown in fig. 6.11. The sample is then cooled to 80 K with applied magnetic field of 50 mT. Therefore, on applying -4 kV/cm voltage, the polarization tends to align along the electric field leading to compressive strain in the system, thereby enhancing the magnetization. However, on applying +4 kV/cm, the polarization is not able to rotate to follow the electric field due to the hardening of polarization rotation, thus resulting in tensile strain and causing reduction in magnetization. Therefore, the ME coupling at 80 K is a strain-mediated coupling effect.

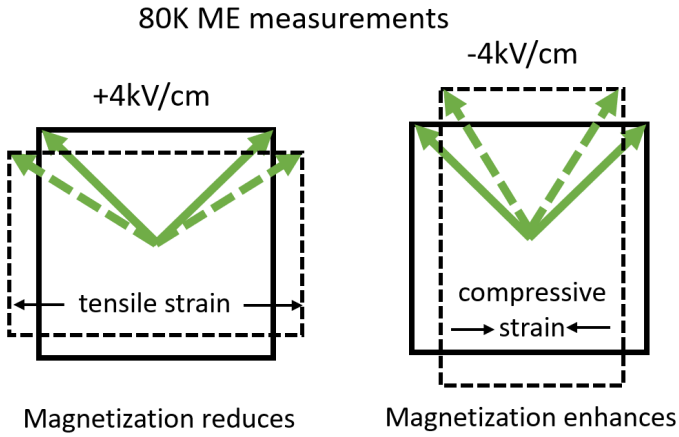

Figure 6.11: Schematic of strain-mediated ME coupling in LSMO/PMN-PT(001) at 80 K.

6.2.3 Directional dependence of ME coupling

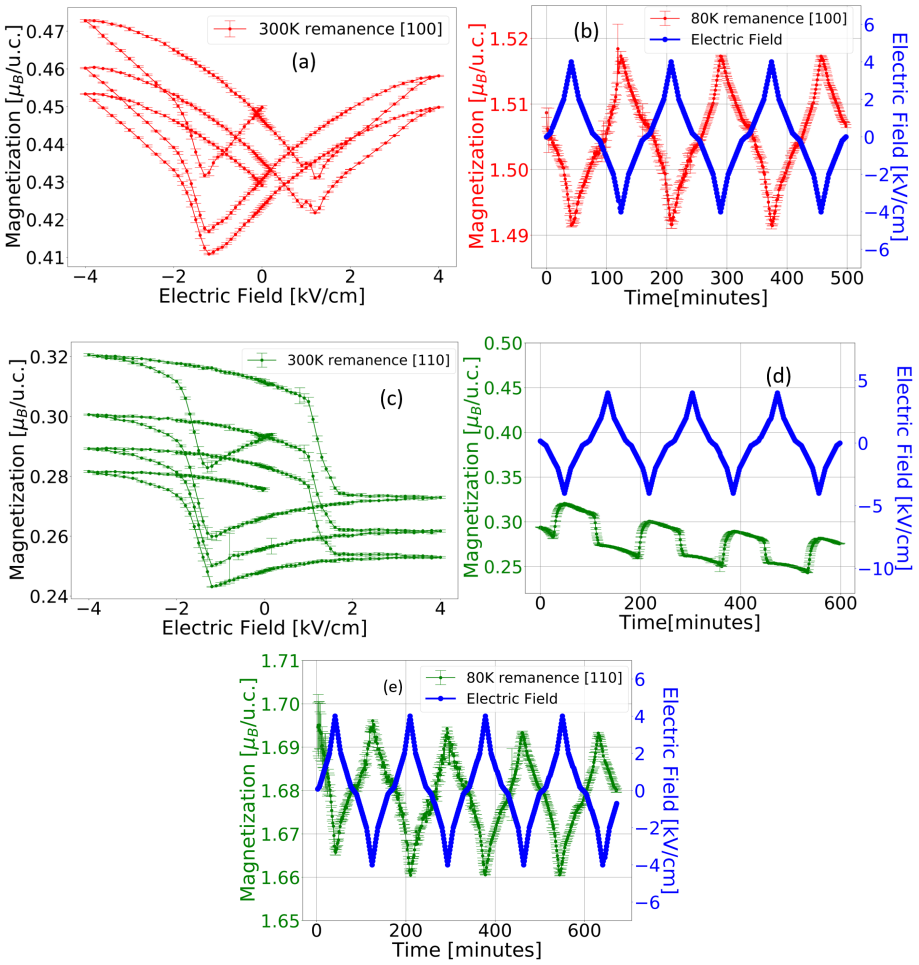

Figure 6.12: **(a)** Magnetization vs electric field curve in remanence at 300 K along hard axis of LSMO [100], **(b)** ME coupling at 80 K along [100], **(c)** ME coupling along easy axis of LSMO [110] at 300 K and **(d)** ME vs time plot of ME coupling along [110] at 300 K showing switching behavior of magnetization, **(e)** 80 K.

The pure influence of electric field on magnetization of LSMO is measured in remanence. LSMO, on experiencing in-plane tensile strain tends to favor in-plane orbital occupancy resulting in an in-plane magnetic easy axis along the face diagonals [110] and [1$\bar{1}$0] and the hard axis is along [100] [9]. Therefore, measurements in fig.6.12 represents nature of ME coupling along the hard axis [100] and along easy axis [110] at 300 K and 80 K, under the pure influence of electric field in remanence. In this

case magnetic moments in LSMO possess more degrees of freedom as they are no longer pinned by the magnetic field. The measurements performed at 80 K along both the axes display no significant change in the behavior compared to earlier measurements with applied magnetic field. The ME coupling still follows a linear strain behavior. However for 300 K along [100], one still observes asymmetric butterfly loop but along the easy axis [110] a hysteresis like loop is observed indicating switching of ferroelectric polarizations in PMN-PT(001). Fig.6.12(e) depicts the ME vs time along [110] where the switching of magnetization is evident near the electric coercive field (E_c) PMN-PT around ±1.5 kV/cm. This demonstrates that polarization switching results in charge-mediated ME coupling which is prominent along easy axis [110] and is also the reason behind the asymmetric butterfly loop along hard axis [100].

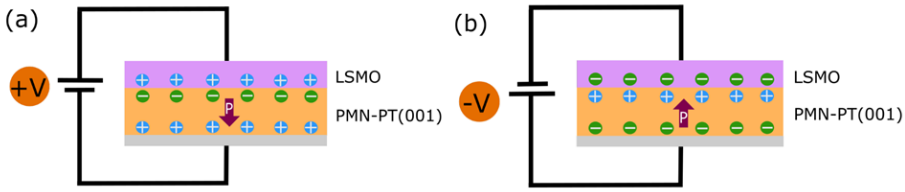

Figure 6.13: Schematic of charge-mediated coupling based on switching of ferroelectric polarization in PMN-PT(001).

PMN-PT(001) exhibits eight possible polarization directions which lie along ⟨111⟩ and on applying positive voltage, (fig. 6.13 (a)), the polarization rotates toward [00$\bar{1}$] direction and with an application of negative voltage,(fig. 6.13 (b)), the polarization rotates towards [001], [86]. This switching of polarization results in accumulation of charges close to the interface in LSMO which affects the Mn^{3+}/Mn^{4+} ratio responsible for the double exchange interaction. With positive applied voltage, positive charges get accumulated and for negative voltage, negative charges are accumulated. The accumulation of negative charges in LSMO causes reduction of Mn^{4+} ions, strengthening the double exchange interaction whereas, the accumulation of positive charges increases the presence of Mn^{4+} ions, thereby weakening the double exchange interaction, hence ferromagnetism in LSMO [87]. This leads to hysteresis loop like behaviour as observed in fig.6.12(c).

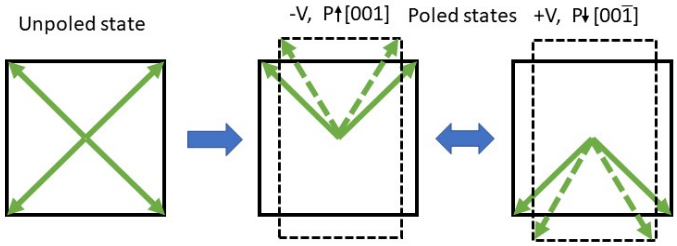

Figure 6.14: Unpoled and poled state of polarizations in PMN-PT(001).

As discussed in the theory chapter, the PMN-PT(001) single crystal possesses spontaneous polarizations along ⟨111⟩ and therefore the lattice parameter is slightly elongated along the polarization directions making the PMN-PT unit cell a 'pseudo-cubic'. under such rhombohedral distortions in PMN-PT(001), the projections of the ⟨111⟩ polarization vectors on the (001) plane lie along the pseudo-cubic ⟨110⟩ directions. In an unpoled state, the virgin states of polarizations as well as FE domains are oriented along the eight possible ⟨111⟩ direction in a stochastic manner, as shown in fig.6.14, leading to random orientation of the in-plane rhombohedral distortions. When the electric field is applied to a PMN-PT(001) single crystals along [001], the dipoles are aligned along any four equivalent ⟨111⟩ direction at $\sim 54.7°$ from the [001]. With increasing electric field these dipoles tend to rotate towards the [001] direction resulting in enhanced strain [88].

6.2.4 Theoretical model

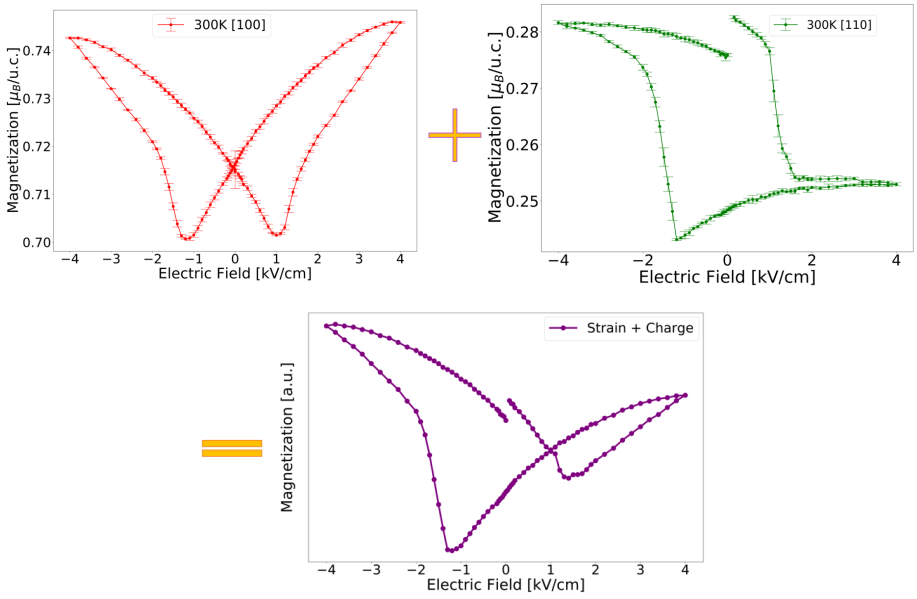

Figure 6.15: Superposition of experimental magnetization data obtained due to strain and charge-mediated ME coupling in LSMO/PMN-PT(001) heterostructure resulting in an asymmetric butterfly loop. Based on this approach, a theoretical model is proposed to de-couple strain and charge mediated effects in ME coupling.

In this section a theoretical model is proposed to de-couple the influence of strain and charge mediated effect in ME coupling. The ratio of strain and charge mediated coupling in a system is sample specific. As in most samples both effects are present simultaneously, the individual contributions superimpose. However, two measurements could be recorded that show pure strain coupling along [100] with applied magnetic field and charge coupling along [110] in remanence as shown in fig.

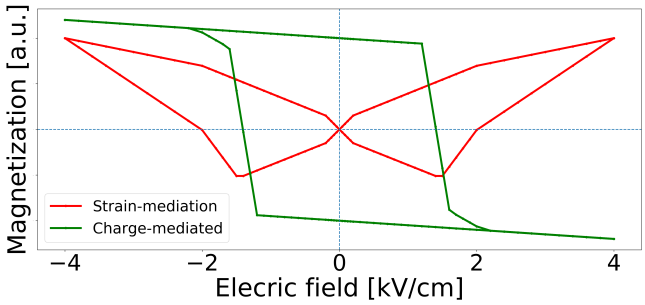

Figure 6.16: Simulation of a mathematical model for qualitative estimation of strain and charge contribution to ME coupling.

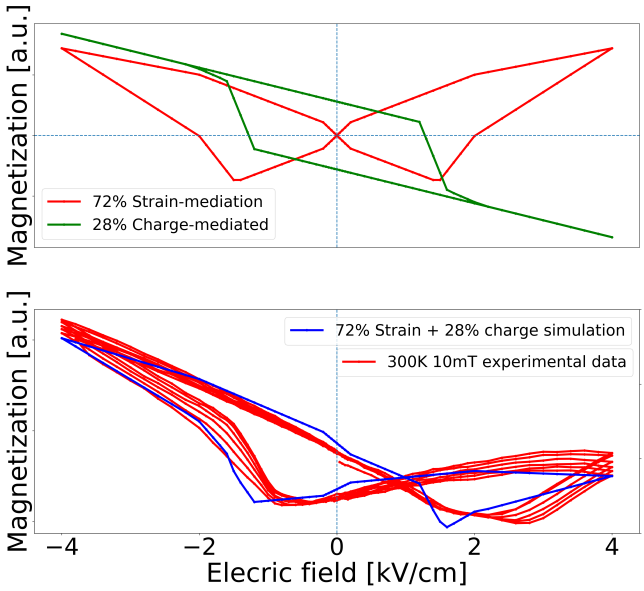

Figure 6.17: Top: The plot depicts the simulation for coupling of 72% strain and 28% charge resulting in an asymmetric butterfly loop. **Bottom:** The simulation is modeled for the experimental data obtained at 300 K with applied magnetic field of 10mT (as shown in fig. 6.10a) showing a qualitative estimation of strain and charge-mediated contributions.

6.15. Combining the two data sets produces an asymmetric butterfly loop similar to results shown in fig. 6.12a. This is not a quantitative model but a qualitative assumption to reproduce the shape of the ME loops in order to motivate the two coupling effects. Thus, one can conclusively say that the asymmetry in strain-mediated butterfly ME loop arises due to the contribution from the charge-mediated FE polarization switching effect. Similarly to the model constructed for Fe_3O_4/PMN-PT in the thesis of Patrick Schöffmann [72], a simple mathematical model is constructed to have a qualitative estimation of strain and charge-mediated contributions in the

ME coupling. This mathematical model consists of a strain and polarization curve created using literature data [89] and normalized to 1 as shown in fig. 6.16. The electric coercive field E_c is taken to be $\pm$ 1.5 kV/cm as in literature.

For quantitative modeling, one needs to measure the strain vs electric field curve and polarization vs electric field curve separately for the PMN-PT(001) substrate. However, this mathematical model is a good starting assumption to determine the qualitative influence of both strain and charge-mediated ME coupling. There are three parts contributing to this mathematical model: strain, polarization and tilt. The third part tilt is an intrinsic part of polarization hysteresis like loop arising due to the presence of multi-domain FE states in PMN-PT (001). This theoretical model is used to fit the ME curve shown in fig.6.10(a) and by playing around with the ratio of three parts mentioned above, a reasonable fit is obtained by taking 72% contribution of strain and 28% charge contribution (fig. 6.17). The top plot, fig. 6.17 depicts how the strain and charge-mediated magnetization loops evolve with the change in the strain and charge ratios.

6.2.5 Before and after voltage measurements

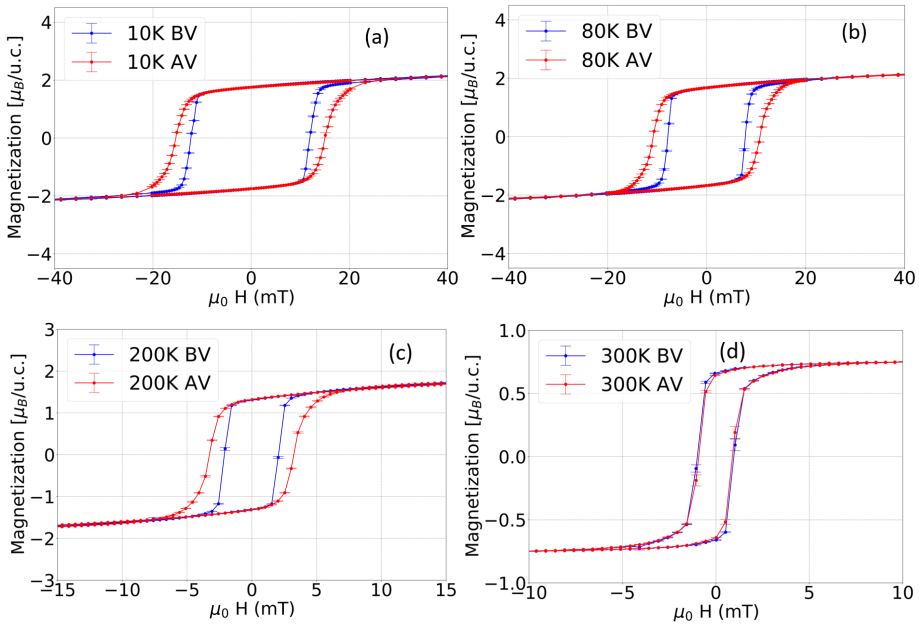

Figure 6.18: Magnetization hysteresis curve measured at different temperatures, **(a)** 10 K, **(b)** 80 K, **(c)** 200 K and **(d)** 300 K, before and after removing the applied voltage. Note the change in scale.

The magnetization vs applied magnetic field curves were recorded before and after removal of the applied voltage, depicted in fig. 6.18 at different temperatures. The

results show a change in coercive field, H_c after removing the voltage. Table 6.2 presents the percentage obtained in H_c.

T(K)	H_C-BV (mT)	H_C-AV (mT)	Change(%)
10K	12.1	15.1	+25%
80K	7.8	10.7	+37%
200K	2.1	3.3	+62%
300K	-0.9	-0.9	within error

Table 6.2: H_C before application of voltage (BV), after removal of voltage (AV), and percentage change. Uncertainty in H_C is ± 0.1 mT.

H_c is the magnitude of magnetic field required to reduce the magnetization of a ferromagnetic material to zero after the sample has been driven to saturation. Fig.6.18 represents the set of measurements recorded along the hard axis [100] of LSMO and after the sample has seen voltage, a significant increase in H_c is obtained at low temperatures. However, no change can be observed within the error in H_c at 300 K. The coercivity is directly related to the magnetocrystalline anisotropy energy (MAE) and it tends to increase along the hard axis under in-plane tensile strain [90]. In our system, when the voltage applied to LSMO/PMN-PT(001) is switched-off, the FE polarizations retain their state and thus continue to strain the system. Since, now the system is under tensile strain, it results in increase of MAE, thereby increasing the coercivity along the hard axis [100] of LSMO. The MAE is dominant at low temperatures and that is the reason, why one observes significant changes at low temperatures [91, 92]. At 300 K the anisotropy field is mostly dependent on the shape anisotropy, thus, the change is not significant.

6.2.6 Negative remanence

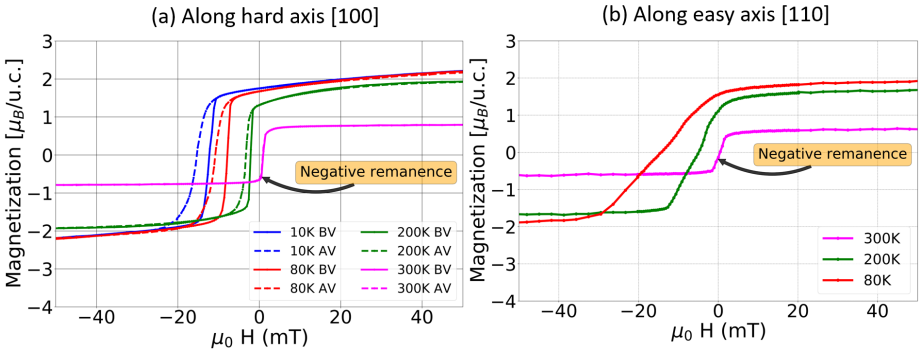

Figure 6.19: (a) First half (from +2.5 T to -2.5 T) of the M-H loops presented in fig. 6.18 showing the presence of negative remanence at 300 K along the hard axis[100] of LSMO and **(b)** half M-H loops along the easy axis of LSMO [110].

While measuring the magnetization hysteresis loops, one observes an interesting behaviour of LSMO/PMN-PT(001). For 300 K M-H curve, a negative remanence is

observed for both hard [100] and easy axis [110] of LSMO. However, at other temperatures (10 K, 80 K and 200 K), the magnetization follows the normal hysteresis loop as shown in fig. 6.19. One should note that this effect is not related to the applied voltage as the negative remanence is observed in the both scenarios: before and after application of voltage.

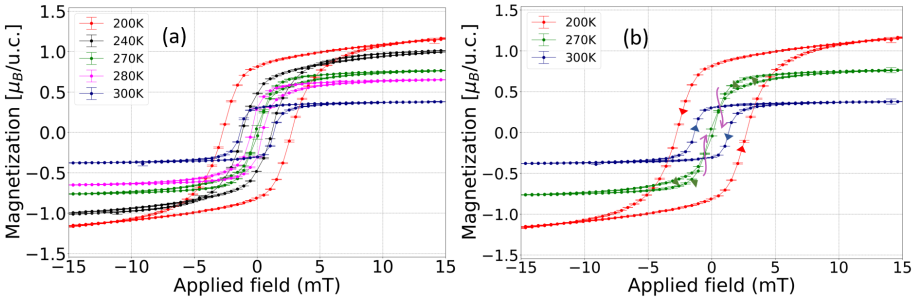

Figure 6.20: (a) M-H loops recorded along [100] at different temperatures. Loops in **(b)** shows the switching temperature 270 K at which behavior changes from normal hysteresis loop to inverted hysteresis loop.

M-H curves are recorded at different temperatures along [100] as shown in fig. 6.20(a) to determine the cross-over temperature at which the behavior of magnetization changes from normal hysteresis loop to inverted hysteresis loop. Fig. 6.20(b) shows that at 270 K the M-H curve becomes very slim and switches to inverted hysteresis loop with negative remanence. After 270 K, the M-H curves start getting broader and the magnetization follows inverted hysteresis loop (IHL) with negative remanence. In a typical ferromagnetic system, if the applied magnetic field is in positive direction, the remanent magnetization M_r is positive. But here one observes that with the applied magnetic field in positive direction leads to negative M_r and inverted hysteresis loop from 270 K onwards. The arrows in fig. 6.20(b) depicts how the magnetization behavior evolves with the applied magnetic field. The negative remanence effect appears when the direction of magnetization is opposite to the direction of applied magnetic field [93]. This means that there is probably some other magnetic ordering present in the system which is able to switch the magnetization of LSMO at this temperature. The initial speculation is based on the results reported by Mottaghi *et al.* [94] and Kumari *et al.* [93] where negative remanence was observed due to the presence of magnetically inhomogeneous spin cluster regions. In our system, one can observe Mn_3O_4 particles at the interface which are ferrimagnetic with T_c=43 K [95], but are paramagnetic at 270 K where one observed negative remanence effect, therefore they cannot influence the magnetization of LSMO at higher temperatures. However, one also observes reduced magnetization at the interlayer from the PNR measurements which is due to presence of Mn_3O_4 particles, defects near the interface as shown in fig.6.5, as well as the strong in-plane tensile strain imparted on LSMO deposited on PMN-PT. The magnetic behavior of LSMO is governed by the double exchange interaction between Mn^{3+} - O^{2-} - Mn^{4+} bond. Now, if there is presence of defects or/oxygen vacancies in the film, it can break this exchange interaction resulting in higher spin disorder [93]. In addition,

it is well known that tensile strain can suppress the ferromagnetism in LSMO due to strain-induced distortions of MnO_6 octahedra. From the above results one can see that there are structural inhomogeneities consisting of spin clusters localized at the interface [96–98]. At higher temperature, the spin disorder is high due to thermal energy and with the presence of magnetically inhomogeneous spin cluster regions, it may become plausible to switch the magnetization direction in LSMO. This is just an speculation for this observed behavior. A clear and systematic study is needed to understand the origin of negative remanence and inverted hysteresis loop in LSMO/PMN-PT(001) heterostructure.

LSMO grows under the influence of in-plane tensile strain imparted from PMN-PT(001) with a lattice mismatch of +3.5%, which results in formation of defects near the interface as seen from fig. 6.5. The magnetic behavior of LSMO is governed by the double exchange interaction between Mn^{3+} - O^{2-} - Mn^{4+} bond. Now , if there is presence of defects or/oxygen vacancies in the film, it can break this exchange interaction resulting in higher spin disorder. In our system, one clearly observes presence of defects and Mn_3O_4 particles near the interface which will definitely affect the magnetic properties of LSMO. Therefore, the presence of negative remanence can plausibly be attributed to coexistence of the magnetically inhomogeneous regions consisting of Mn_3O_4 particles and lower ferromagnetic ordering in the LSMO thin film [93].

6.3 Depth resolved magnetization

The magnetic depth profile of LSMO/PMN-PT(001) is probed as a function of voltage via polarized neutron reflectometry (PNR). The experiments were performed at NIST Center for Neutron Research (NCNR), NIST using the 'Polarized Beam Reflectometer (PBR)'. The experiments are performed at two temperatures: 300 K and 80 K with two magnetic fields: 10 mT and 50 mT, respectively. The same magnetic fields are used in the ME measurements performed at MPMS. The magnetic fields used at each temperature are near saturation (sample is nearly saturated but not completely), which means that there is a possibility to observe spin-flip signal from the sample. Due to this reason, all four channels were recorded: R++ (UU), R– (DD), R+- (UD) and R-+ (DU). With PNR, one can probe how the magnetization of the system varies along the depth of your film. It quantifies the laterally averaged scattering length density (SLD) perpendicular to the sample surface. The SLD profile obtained from the fitting model has two components: NSLD which gets affected by parameters like film thickness, roughness, density and chemical structure of the unit cell, then there is MSLD which depends on the magnetization per unit cell and the magnetic roughness. Based on these parameters, a fitting model is prepared and these parameters can be strongly correlated, the effect of which one observes during the fitting refinement. Fig. 6.21 shows the sample orientation with respect to the neutron beam and the applied magnetic field. The electrical connections are made using Ag paste and thin platinum wires. The voltage is applied along [001] direction.

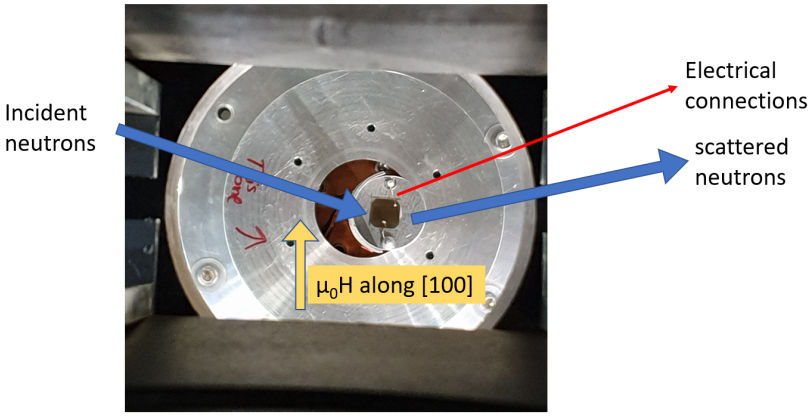

Figure 6.21: Image of voltage sample holder at PBR with neutron beam direction and the applied magnetic field direction with respect to the sample.

For the electric field of 0 kV/cm, the first curve was measured at 80 K and then the temperature was ramped up to 300 K. Before every measurement the rocking curve was recorded for each electric field as the voltage was ramped in small steps at both the temperatures. Once reaching at 300 K, one started to ramp up the voltage and the rocking curve for different electric fields at 300 K is shown in fig. 6.22(a). One can see that as the magnitude of applied electric field increases, the rocking curve gets broader and broader with a significant drop in peak intensity. The rocking curve is the broadest at 300 K for -4 kV/cm. Once the voltage loop was completed for 300 K, the sample was cooled to 80 K with the applied magnetic field of 50 mT and repeated the voltage loop. Fig.6.22(b) depicts the rocking curve at different steps of electric field. The rocking curve continues to broaden up further on application of voltage at 80 K. Fig.6.23 demonstrates the slit settings used during these measurements. After application of voltage, the reflected beam broadened as one can see from the rocking curve measurements and since the slits were not open enough to capture all the intensity from the broad rocking curve, some intensity was lost. Broadening of rocking curve means that the application of voltage introduced some surface corrugation which smeared out the PNR signal resulting in the significant drop in the intensity. This surface corrugation led to major pre-critical egde artifacts in the data, thus making the data fitting complicated. The spin-flip signal in the plots is shown until 0.02 $Å^{-1}$ as the intensity becomes zero within the error bars.

Even with the deteriorated signal and broad rocking curve, the SLD profile reveals interesting results. Fig. 6.24 depicts the measurements performed at 80 K with different applied electric fields. The data reduction and fitting is performed using Refl1D and Reductus programs [99]. A simplest model is used to fit this data which includes an LSMO film, an interlayer and the substrate. After first fitting, LSMO NSLD, PMN-PT NSLD, interlayer NSLD and the interlayer thickness were kept constant while other parameters were allowed to vary to get the best fit within the simple physical model. Although there is a drop in peak intensity after application

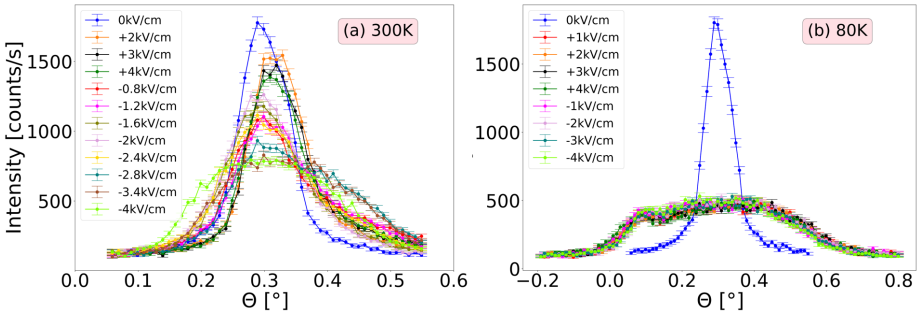

Figure 6.22: Rocking curves measured at different steps of applied electric field **(a)** at 300 K ,**(b)** and at 80 K.

of electric field, this will not effect the NSLD profile as it is material dependent and not intensity dependent.

The reduced NSLD and MSLD indicates some stoichiometric fluctuation at the interface which is further studied using TEM. Table.6.3 represents the change in magnetization with the application of bipolar voltage. The slight variation in LSMO thickness is also observed which can be understood considering the system strained on application of voltage. The roughness increases with voltage which is evident from the rocking curves and the drop in the intensity of the signal. One can see that the MSLD of LSMO stays constant and starts to drop as the nuclear roughness increases. Magnetic roughness and nuclear roughness are strongly correlated parameters. Due to the time between the growth, measurement and transport, the top interface of the film is not very smooth due to some aging effect. The interesting thing to note is that one observes an interlayer with reduced NSLD and MSLD and with the thickness of 53^{+1}_{-1}, Å. The deduced LSMO layer thickness is 268^{+1}_{-1} Å. All three SLD profiles are plotted together in fig.6.25 (a).

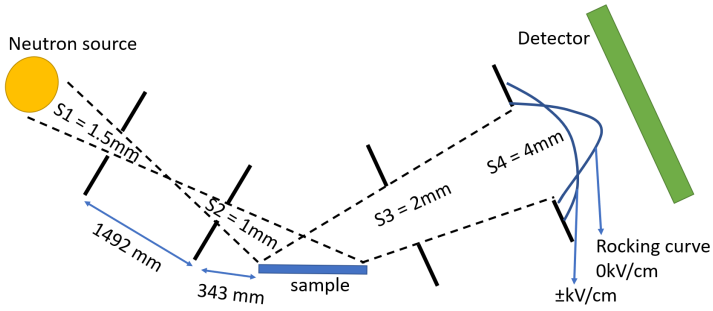

Figure 6.23: Schematic of slit settings used during the measurements and due to the broadening of the rocking curve, some of the intensity was lost due to the narrow slit opening which resulted in artifacts in the PNR data.

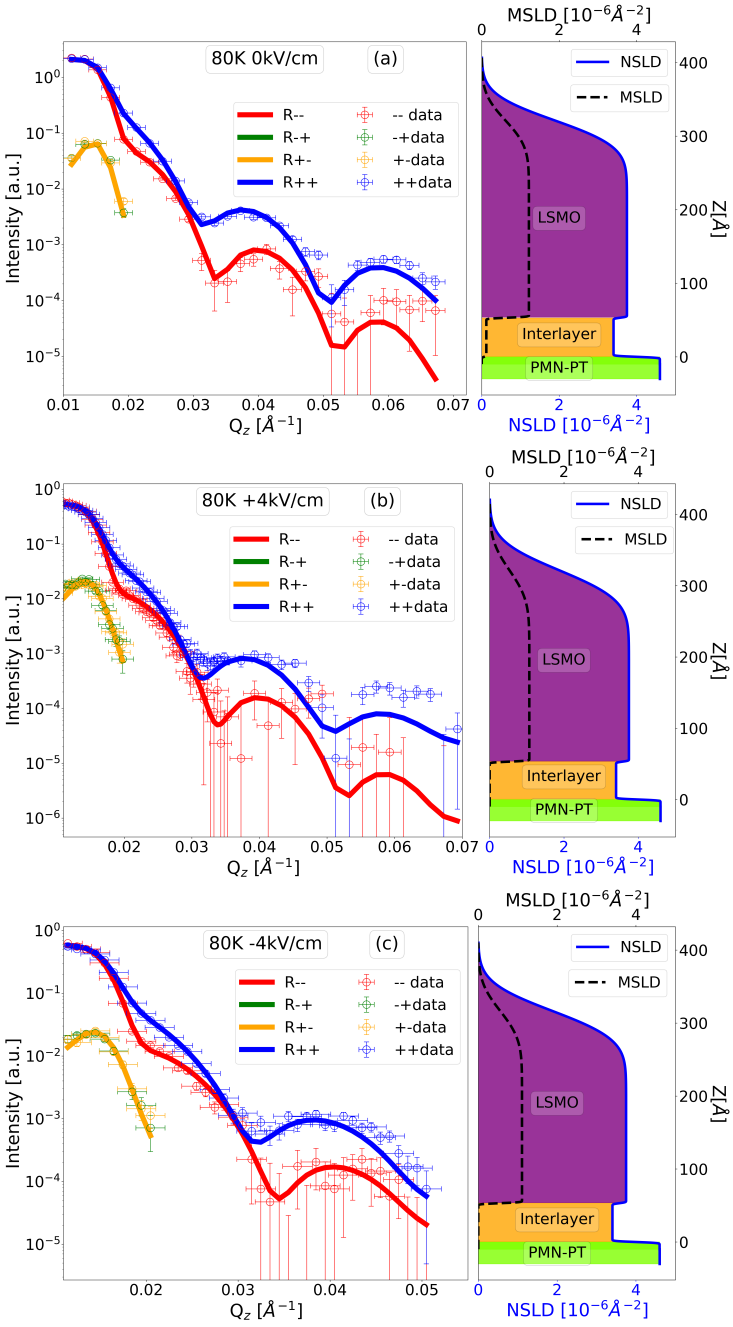

Figure 6.24: PNR curves measured at 80 K with the applied magnetic field of 50 mT at **(a)** 0 kV/cm **(b)** +4 kV/cm and **(c)** -4 kV/cm with deduced SLD profiles. Note the change in scale.

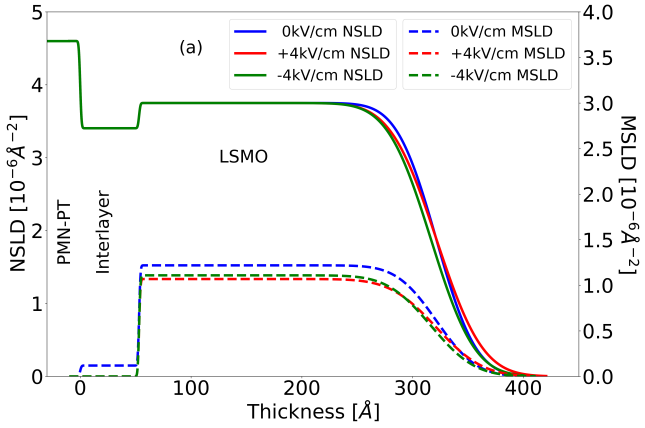

Figure 6.25: SLD profiles of PNR curves measured at 0 kV/cm, +4 kV/cm and -4 kV/cm.

Parameter	0kV/cm	+4kV/cm	-4kV/cm
LSMO d [Å]	268.30^{+1}_{-1}	268.40^{+1}_{-1}	263.50^{+3}_{-1}
LSMO σ [Å]	28.30^{+2}_{-1}	32.90^{+1}_{-3}	31.10^{+2}_{-2}
LSMO M [$\mu_B/u.c.$]	$2.67^{+0.10}_{-0.10}$	$2.34^{+0.08}_{-0.03}$	$2.43^{+0.06}_{-0.05}$
Interlayer M [$\mu_B/u.c.$]	$0.24^{+0.06}_{-0.07}$	-	-

Table 6.3: Parameters (d: thickness, σ: roughness and M: magnetization per unit cell) used for the fitting model with different voltage steps. These parameters were allowed to vary.

The observed magnetization of LSMO is highest for 0 kV/cm and drops for the other electric fields. This is due to the change in the sample quality which is evident from the broadening of the reflected beam. One has to mention that the starting state of magnetization for the samples used for PNR and SQUID is different. In SQUID measurements, the sample first cycles through 6 voltage loops at 300 K and then it is cooled to 80 K for another set of voltage loops. It has been observed in the ME measurements, that for the first cycle of applied voltage at 300 K, the magnetization drops initially and then follows the butterfly loop as can be seen from fig.6.26. This behavior is observed for other SQUID measurements as well. Therefore, when 0 kV/cm is measured at 80 K in SQUID, the magnetization has been already reduced, whereas for PNR measurements, the magnetization was recorded for both the temperatures in the virgin state of the sample for 0 kV/cm. That is why the magnetization value obtained from PNR for 0 kV/cm at 80 K is higher than gated values.

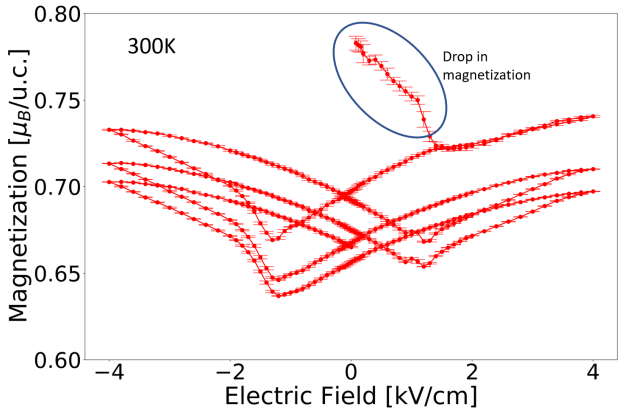

Figure 6.26: Drop in magnetization in the first cycle of voltage loop measured at 300 K with applied field of 10 mT.

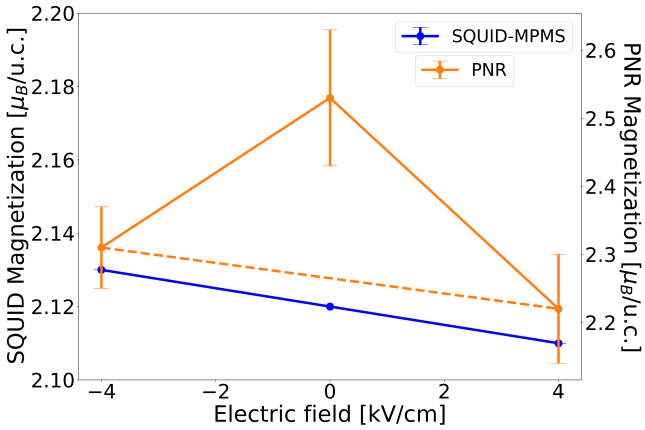

Figure 6.27: Comparison between the magnetization obtained from SQUID-MPMS and PNR for ±4 kV/cm at 80 K. The error bars for SQUID are smaller than the data point. The magnetization obtained for 0 kV/cm from PNR is higher than the gated values as it was measured in the virgin state of the sample. This has been observed in SQUID that magnetization drops initially before it starts following a butterfly loop as shown in fig. 6.26. The change in magnetization in PNR for ±4 kV/cm follows similar pattern as in SQUID-MPMS.

However, the magnetization obtained for -4 kV/cm is higher than for +4 kV/cm, which is in good agreement with the SQUID measurements as shown in fig. 6.27. The spin-flip signal arises due to the magnetization angle of $\sim 18°\pm2°$ from the quantization axis of the polarized neutron beam and the angle of magnetization remains constant throughout the depth of the film. Due to the problem of surface corrugation which resulted in smearing out of the PNR signal, one may have lost

some of the precise information. From the overall measurement and analysis, one was able to observe the strain-mediated ME coupling in LSMO/PMN-PT(001) with a presence of interlayer. Taking into account the 18° rotation of magnetization and for comparison with SQUID data which will only see the longitudinal moment rather than vector, one can calculate magnetization from the relation: $M_L = M\cos\theta$, where θ is 18°, M_L is longitudinal component of magnetization and M is the vector magnetization. The M_L obtained for -4 kV/cm and +4 kV/cm will be 2.31±0.06 $\mu_B/u.c.$ and 2.22±0.08 $\mu_B/u.c.$ respectively. From SQUID its 2.13 $\mu_B/u.c.$ for -4 kV/cm and 2.11 $\mu_B/u.c.$ for +4 kV/cm.

The 300 K measurements are shown in supplementary material. Due to low magnetic signal and artifacts in data after application of voltage, it was difficult to fit the data. Some measurements were performed by mail-in experiment at ILL with reflectometer SUPERADAM. Two samples were sent, one in the virgin state and other after applying the voltage. The aim of the experiment was to investigate presence of any off-specular magnetic scattering as a function of voltage but due to time constraint, it was not possible to perform full polarization analysis over the complete detector area. The 2D detector maps obtained from the experiment shows some off-specular scattering but one cannot be sure if it is due to any magnetic feature as off-specular scattering can arise from roughness of the sample as well, thus can be just nuclear contribution.No other new information was obtained from this measurement. The 2D maps are shown in supplementary material.

X-ray reflectivity was performed on a similar LSMO/PMN-PT(001) sample using our in-house GALAXI [71] to determine the thickness. GALAXI provides longer Q-range for measuring as the sample to detector distance can be adjusted as per requirements.

Fig.6.28 represents the fit for obtained XRR curve with two models: LSMO-interlayer-substrate and LSMO-substrate. The experimental data shows dampening of the oscillation between $Q_z = 0.2$ to 0.3 $Å^{-1}$ which indicates presence of another layer. The index of refraction is defined as $n = 1 - \delta + i\beta$. The best fit is obtained with a model having interlayer. The interlayer is an intrinsic formation in the system and its thickness can vary from sample to sample. The thickness deduced from XRR fitting is LSMO : 270 ± 1 Å and interlayer: 11 ± 3 Å. The XRR (fig.6.4c) measured with Bruker D8 diffractometer does not show any oscillation dampening due to lower Q-range compared to GALAXI. The fitting was performed by Randolf Beerwerth using *Born-again* software [100].

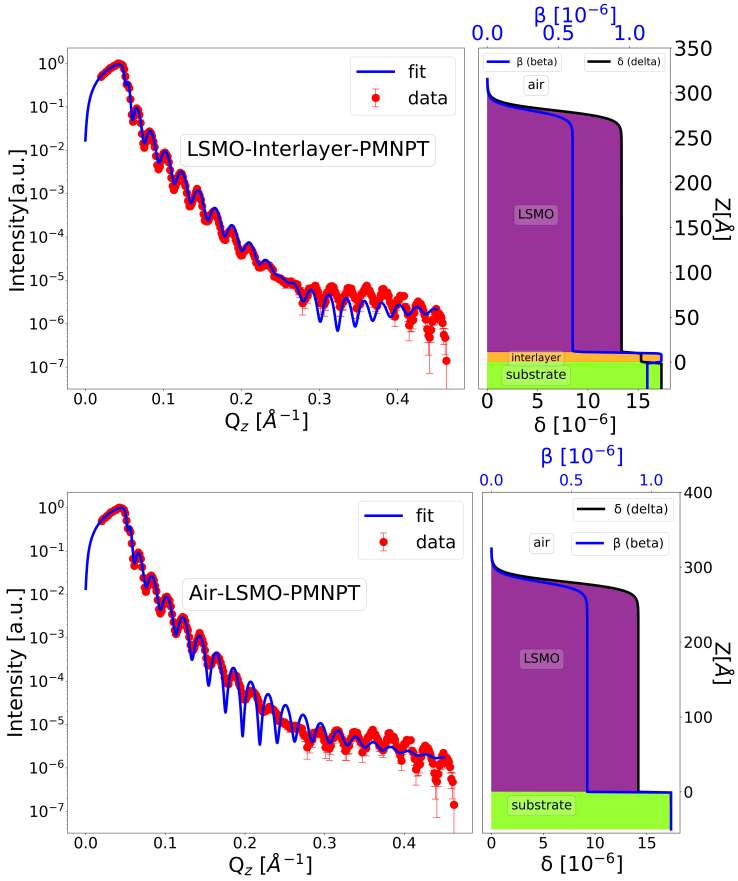

Figure 6.28: Top: XRR curve representing presence of an interlayer in the profile of index of refraction in LSMO/PMN-PT(001) heterostructure. **Bottom:** Model presentation if only LSMO layer is taken into consideration. Fitting performed by Randolf Beerwerth.

6.4 STEM studies of the interlayer

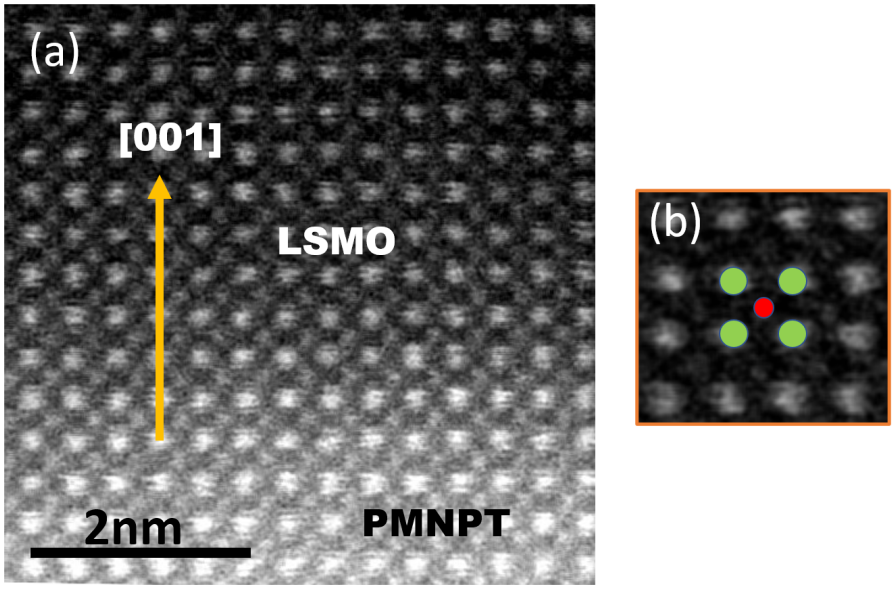

Figure 6.29: (a) HAADF-STEM image of epitaxial growth of LSMO on PMN-PT(001). **(b)** AMO perovskite structure represented with colored spheres indicated A-site (green) and M-site (red).

HAADF-STEM measurements were performed on LSMO/PMN-PT(001) heterostructures to study the structural properties of the interlayer and the film. These measurements are from the samples which have not been exposed to the voltage. The measurement depicted in fig. 6.29 shows a pseudo-cubic structure and A-site and M-site of the perovskite is depicted in the magnified section in fig. 6.29(b). Due to the large lattice mismatch between LSMO and PMN-PT, there is formation of defects which has been shown in fig. 6.5. In order to probe the information about stoichiometric fluctuations as in the interlayer, chemical imaging is performed.

The fig. 6.30(a) displays the cross-sectional overview of the heterostructure where one can already observe the presence of dark regions near the interface and fig. 6.30(b) shows a close-up, revealing the dark regions to be particles with a triangular cross-section. HAADF-STEM images are formed by using incoherent elastically scattering electrons which are collected at higher angles (69 mrad). It is more sensitive to heavier elements as they have larger scattering cross-section whereas for lighter elements with smaller scattering cross-section, HAADF or Z-contrast is sensitive to the compositional changes. The fig. 6.30(b) represents darker regions at the interface which means there is stoichiometric fluctuation and the elemental composition has lower Z elements compared to the bulk of the film.

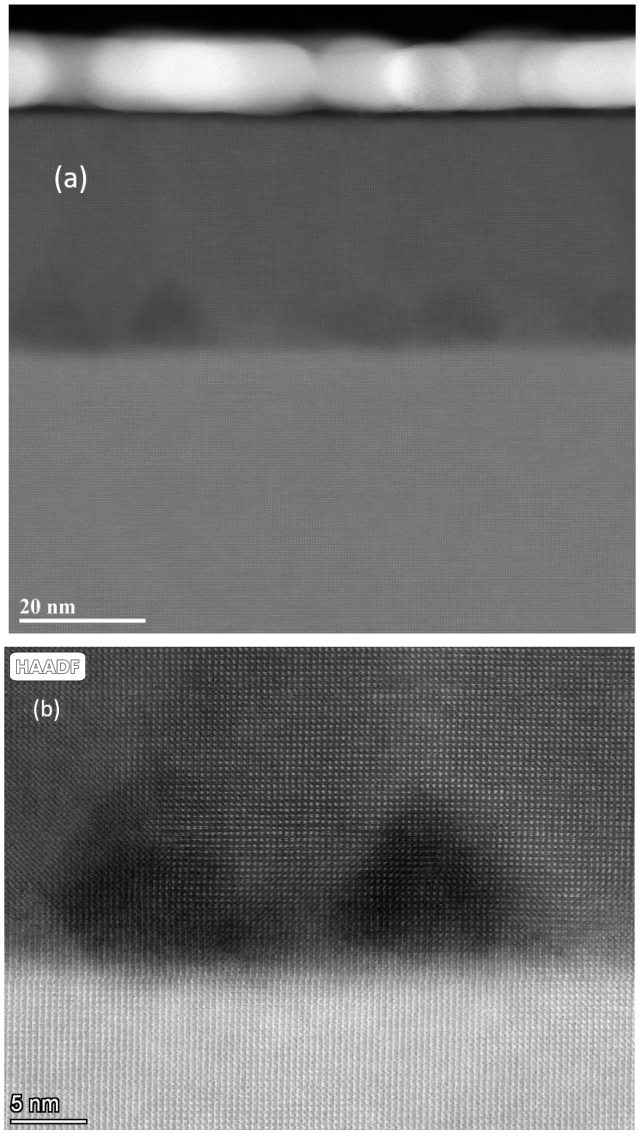

Figure 6.30: (a) Overview of the cross-section along [001] of LSMO/PMN-PT(001) heterostructure. Au layer is deposited on the top. One can see the presence of triangular shaped particles as dark regions. **(b)** the HAADF-STEM image shows presence of triangular shaped dark regions at the interface of LSMO and PMN-PT.

EDS in STEM is used to collect the chemical information across the interface as shown in fig.6.31 depicting La-deficiency in the darker regions.Since the contrast is not very high, the EDS maps of La and Mn with HAADF were superimposed where one observes the La-deficient areas have Mn-excess as depicted in fig.6.32. For

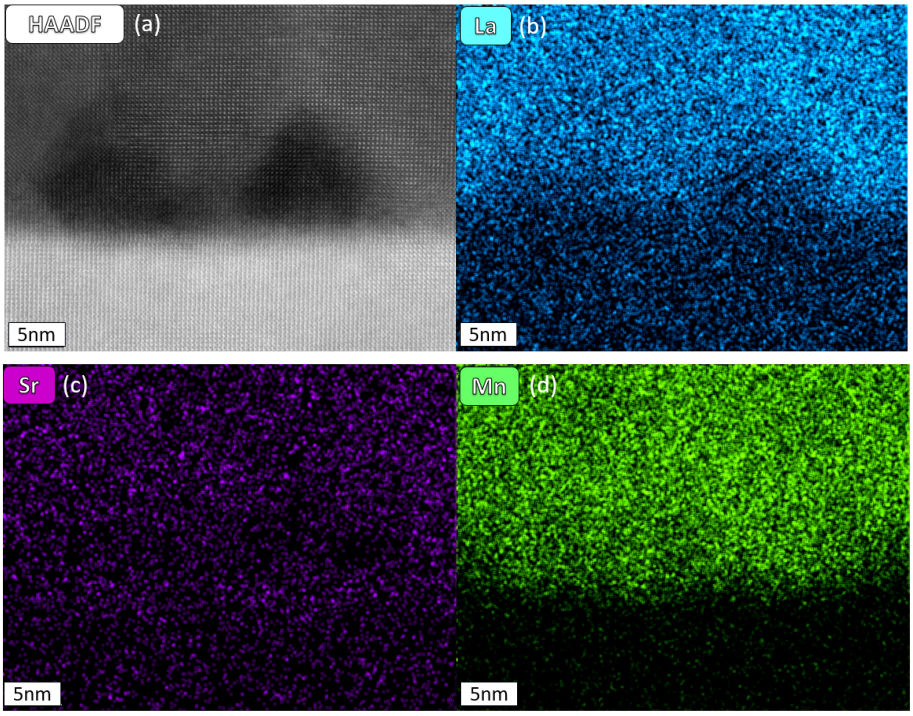

Figure 6.31: Spectrum imaging with STEM/EDS **(a)** HAADF-STEM image, **(b)** La-EDS map showing La-deficiency in the dark triangular shaped regions, **(c)** Sr-EDS map and **(d)** Mn-EDS map.

further clarification, EDS spectra is extracted from different characteristic regions of interest as shown in fig. 6.33.

From the atomic fractions obtained from EDS measurements, one can calculate the stoichiometry of of the probed region. Area 1 shows less than 5% of Mn_3O_4 and the darker region shows more than 30% of Mn_3O_4. There is a slight inter-diffusion of Pb and Nb near the interface. One observes a kink in magnetization in FCC and ZFC curve shown in fig.6.7(a) which is around 43 K. The Curie temperature of Mn_3O_4 is 43 K, [95] thereby confirming the particle stoichiometry to be Mn_3O_4.

Parameter	La:Sr ratio
Area 1	$0.77^{+0.05}_{-0.07} : 0.23^{+0.07}_{-0.05}$
Area 2	$0.76^{+0.06}_{-0.06} : 0.24^{+0.06}_{-0.06}$

Table 6.4: La:Sr ratio in LSMO obtained from the EDS spectrum recorded for the area 1 and area 2.

The stoichiometry obtained from these measurements (table. 6.4) are very localized as STEM provides the information only of the probed region of interest. The

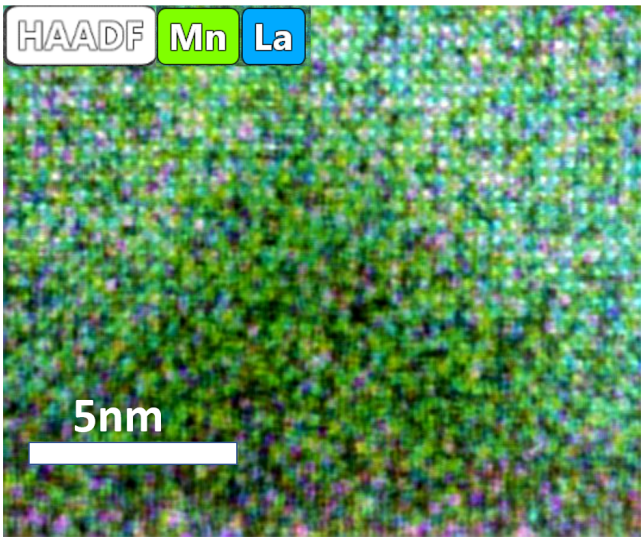

Figure 6.32: EDS maps of Mn and La overlapped with HAADF image showing the excess Mn in dark region.

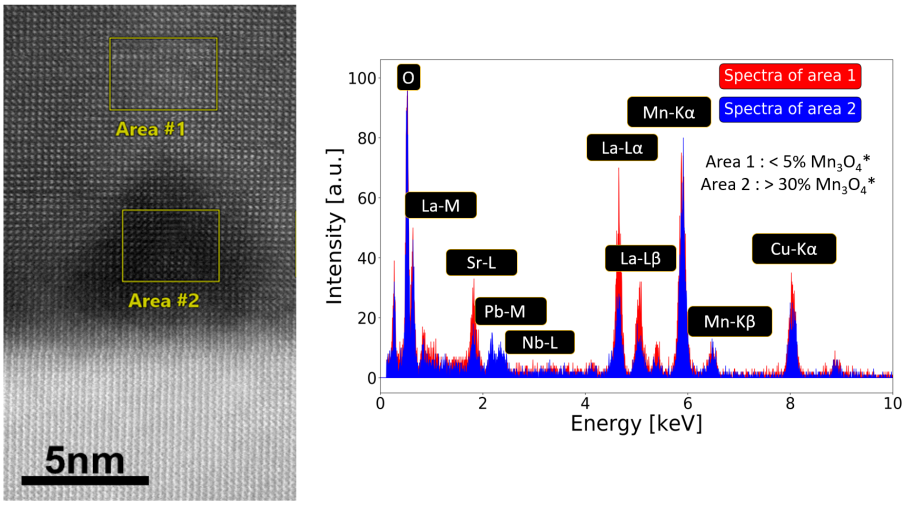

Figure 6.33: EDX spectrum of area 1 and 2. * EDX itself does not prove the Mn-excess to be in Mn_3O_4 stoichiometry but measurements shown in fig. 6.7 shows jump in magnetization at at 43 K which is a Curie temperature ,T_C, of Mn_3O_4.

stoichiometry of the complete film is determined by RBS shown in fig. 6.6.

The presence of these Mn_3O_4 particles explains the drop of NSLD in the PNR data as Mn has negative scattering length. It has to be noted that the particle size of

Mn_3O_4 can vary from sample to sample as it is intrinsic formation during growth. For the sample measured in TEM, the particle height is 80-90Å composing of interlayer whereas the sample used for PNR has interlayer width of 53Å. The formation of Mn_3O_4 particles at the interlayer is not surprising due to its chemical compatibility with the whole manganite perovskite family [101]. Mn_3O_4 crystallizes in a distorted spinel structure with tetrahedral A-sites occupied by Mn^{2+} ion and the octahedral B-sites are occupied by Mn^{3+} ions [102, 103] with cell parameters of $a = 5.76$ Å and $c = 9.47$ Å. The manganese segregation in such a compound usually occurs due to La-deficiency which is visible in fig. 6.31 and the appearance of manganese oxide at the interface appears in a stochastic manner as seen from STEM images. The biaxial in-plane compressive strain from PMN-PT(001) and high oxygen partial pressure during growth allows Mn_3O_4 to grow epitaxially in cubic phase [104–106]. When growing on PMN-PT(001), Mn_3O_4 experiences in-plane compressive strain of -1.2% which is smaller compared to +3.5% in-plane tensile stain experienced by LSMO, thus making it energetically favorable for Mn_3O_4 to nucleate on top of the substrate. TEM images show the possible presence of triangular shaped- Mn_3O_4 particles at the interlayer.

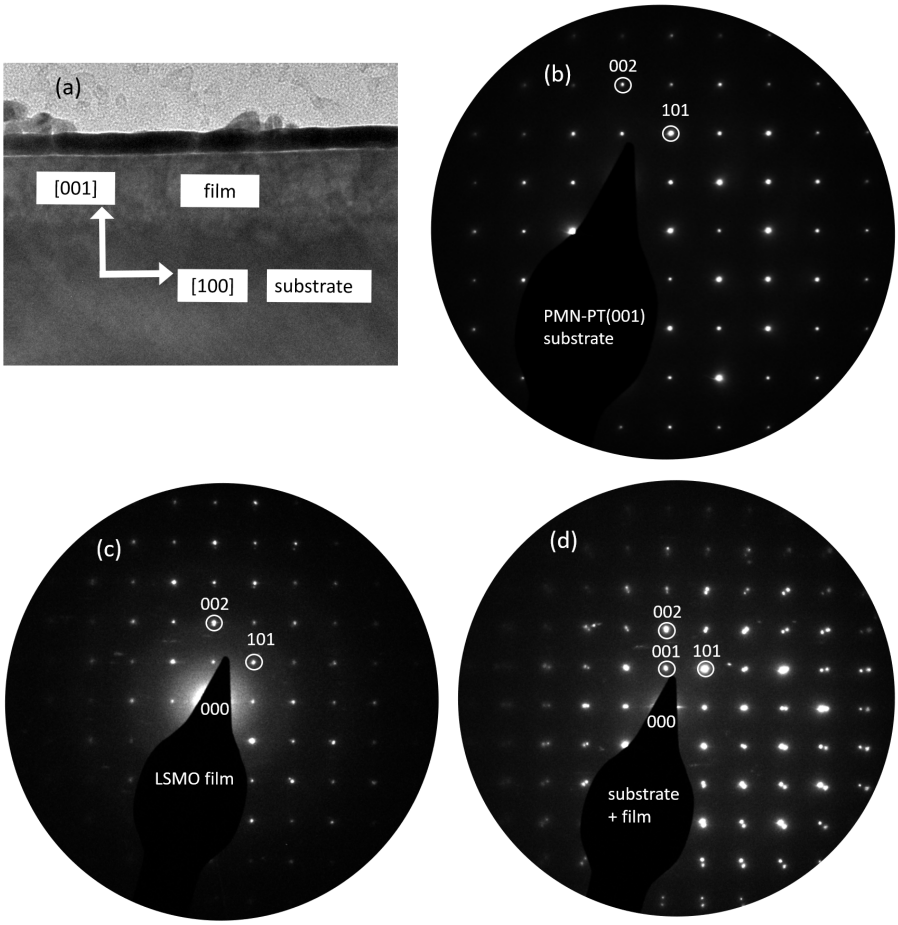

Figure 6.34: (a) SAED-TEM image of the cross-section of LSMO/PMN-PT(001). **(b)** Electron diffraction pattern of the substrate PMN-PT(001), **(c)** Electron diffraction pattern of the film LSMO and **(d)** Electron diffraction pattern of the film + substrate. This splitting of spots indicate the strain relaxation in the film.

The electron diffraction pattern is recorded for the substrate, film and the film + substrate together as shown in fig. 6.34. From the diffraction pattern obtained from the substrate and film, a clear cubic lattice is visible. However, the diffraction pattern of film + substrate displays splitting of reflections arising due to the difference in the structures in the film caused by strain relaxation. The strain usually relaxes in 2-3 monolayer right after the growth. The presence of strain relaxation in LSMO is not surprising owing to the fact that LSMO and PMN-PT has large lattice mismatch of +3.5%. The precipitates visible on the top of the LSMO film in in fig. 6.34(a) are the excess of Mn which crystallized on the top of the film. It is visible in the AFM image in fig.6.2(d).

6.5 Conclusions

LSMO films were successfully grown on PMN-PT(001) substrate. RHEED, LEED, XRR and XRD confirm the single crystalline thin films of LSMO. The STEM measurements show epitaxial growth of LSMO. A stable ferromagnetic state is observed from macroscopic magnetization measurements. The LSMO/PMN-PT(001) heterostructures demonstrate magnetoelectric coupling which has contribution from both strain and charge-mediated ME coupling. Different parameters influence the presence of these ME couplings. The strain-mediated ME coupling is found to be prominent along the hard axis [100] of the LSMO whereas charge-mediated ME coupling becomes prominent along the easy axis [110] of LSMO at 300 K. A change in the behavior of strain-mediated ME coupling is observed as function of temperature which changes from butterfly loop at 300 K to linear at 80 K. Change in H_C is observed after removing the voltage. The increased H_C after voltage is attributed to the magnetocrystalline anistropy energy which increases with tensile strain. An interesting effect of negative remanence is observed at higher temperature in LSMO/PMN-PT(001) heterostructures which probably arises due to the presence of inhomogeneous magnetic layer near the interface of LSMO/PMN-PT(001). A systematic study is required to fully understand the appearance of negative remanence effect in this system. The study of magnetic depth profile using PNR reveals presence of interlayer with reduced NSLD and MSLD. The reduced magnetization in interlayer is not surprising owing to the fact that high tensile strain can suppress the ferromagnetism in LSMO. Also, one observes presence of defects near the interface which also plays role in breaking the exchange interaction between Mn-O-Mn bond, thus reducing the ferromagnetism. The interlayer is probed by TEM which shows the presence of Mn_3O_4 particles in LSMO layer. The presence of these particles was confirmed by ZFC and FCC measurements also which show kink in the magnetization near 43 K, Curie temperature T_C of Mn_3O_4. Due to good chemical compatibility, it becomes easier for Mn_3O_4 to nucleate in an LSMO matrix.

7 Experimental results II: ultra-thin LSMO/PMN-PT(001)

This chapter discusses the results obtained for ultra-thin LSMO deposited on PMN-PT(001) substrate using OMBE. The previous chapter details out the results which were influenced by both the bulk and the interface properties of LSMO/PMN-PT(001). By growing a thin layer of LSMO, the influence of interface effects are more visible.

7.1 Structural characterization

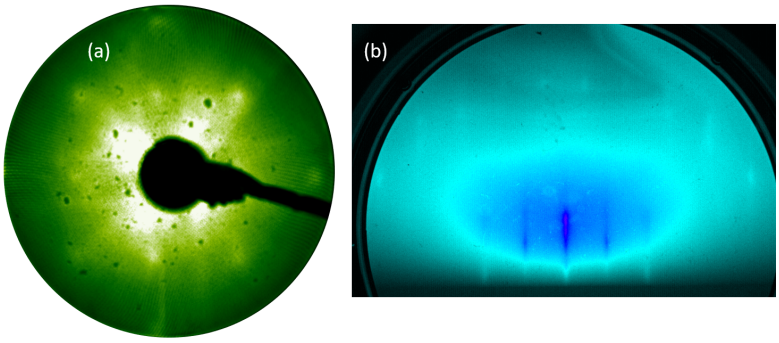

Figure 7.1: In-situ structural characterizations **(a)** LEED and **(b)** RHEED pattern of about 100 Å $La_{0.7}Sr_{0.3}MnO_3$ film deposited on PMN-PT (001) substrate.

An ultra-thin LSMO film was deposited on PMN-PT(001) substrate using OMBE. It was structurally characterized in-situ with LEED and RHEED as shown in fig. 7.1. The RHEED pattern displays presence of Laue spots as well as sharp RHEED spots confirming the good crystallinity of the sample. However, the LEED spots are not so sharp as one can see from the fig. 7.1 (a) suggesting that the surface of the LSMO film is not very smooth. The film is further studied using X-ray diffraction which depicts single crystalline growth of LSMO as shown in fig. 7.2 (a). The LSMO film has out-of-plane lattice parameter of $c = 3.82 \pm 0.003$Å which matches the c obtained for 300Å thick LSMO in the previous results. This means that the film is partially relaxed. The thickness of the LSMO layer determined by XRR (fig. 7.2) is 110.6 ± 0.6 Å with a roughness of 3.4 Å.

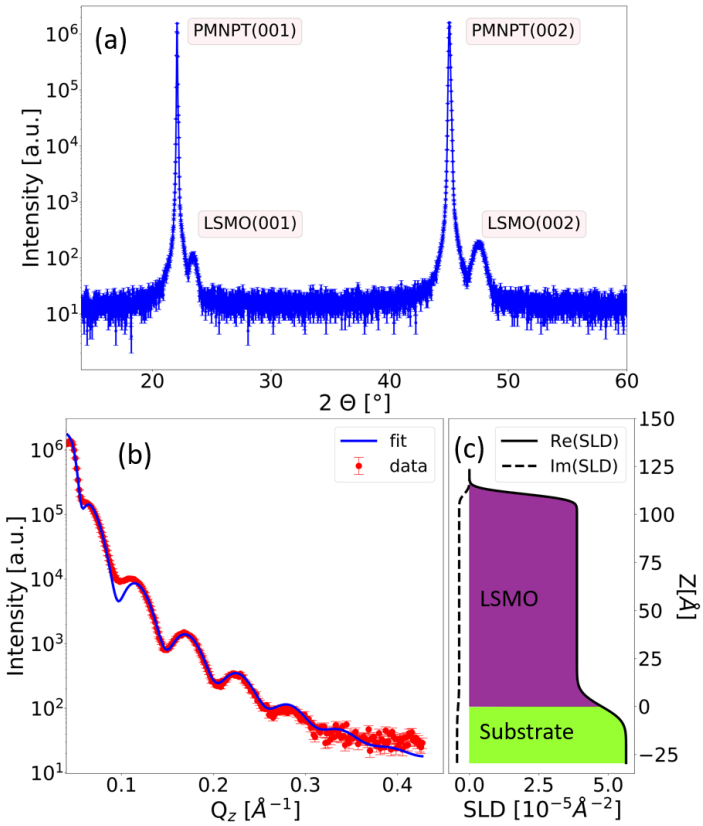

Figure 7.2: **(a)** XRD and **(b)** XRR of $La_{0.7}Sr_{0.3}MnO_3$ film deposited on PMN-PT (001) substrate. **(c)** The XRR fit assumes the ratio of 8:2 for LSMO : Mn_3O_4 particles. The XRR fitting parameters are mentioned in supplementary material in table. S5

The initial model used for the fitting of the XRR curve consists of LSMO layer and substrate, with a reduced SLD value of the LSMO layer compared to the theory. This reduced SLD could result from the defects or holes in the film. Based on the previous measurements and results, a new model was created with a 'ratio' parameter which controlled the ratio between Mn_3O_4 particles (as seen from previous results) and LSMO in the film. Both models produced similar results with reduction of SLD in the LSMO layer, with a ratio parameter of 80% LSMO and 20% Mn_3O_4 in the LSMO layer. Considering the results obtained earlier, the ratio model is the better explanation for the reduced SLD. The fitting is not perfect as one can see from the XRR fit that the pre-critical edge does not matches so well due to some artifacts in the measurement. Also, the dip of the oscillation at $Q_z = 0.1\,\text{Å}^{-1}$ does not fit well. Based on the different parameters taken into account, this is the best fit obtained for 110 Å LSMO film.

7.2 Macroscopic magnetization measurements

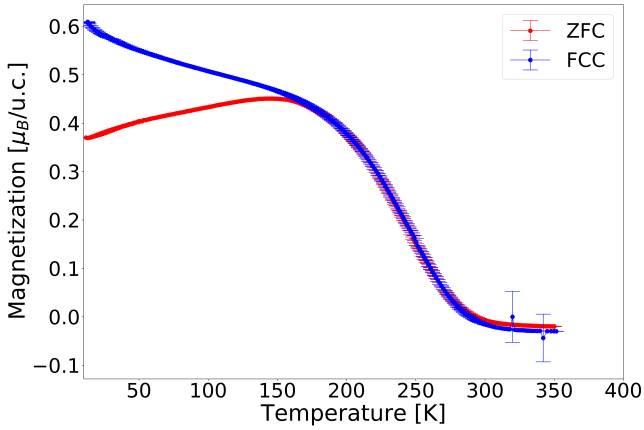

Figure 7.3: Magnetization vs temperature curves measured with applied field of 50 mT for 110 Å LSMO/PMN-PT(001).

Magnetization as a function of temperature was recorded with an applied magnetic field of 50 mT. Fig. 7.3 shows the ZFC and FCC curves for the ultra-thin LSMO film. The T_C has significantly reduced from 328 K for 300 Å thick LSMO to 283 K for 110 Å LSMO film. It is known that the tensile strain suppresses ferromagnetism and reduces T_C due to strain induced MnO_6 octahedra distortion [96]. There is a decrease in the magnetization in ZFC curve in the low temperature regime which indicates some pinning of magnetic moments in LSMO. From the results obtained for 320 Å thick LSMO film, one observes presence of defects and inhomogeneously magnetic film near the interface. Therefore, with the thickness of 110 Å, the effect of defects and strain imparted by the PMN-PT substrate become much more visible. The presence of defects/oxygen vacancies can easily break the Mn-O-Mn bond which would result in clusters of disordered spins near the interface, the effect of which is visible in ZFC curve.

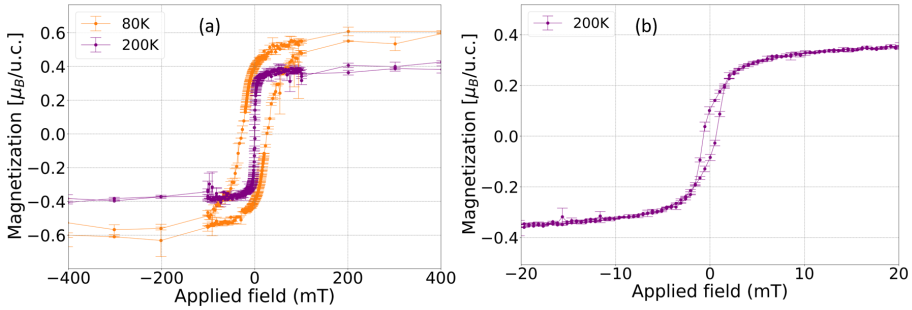

Figure 7.4: (a) M-H curves recorded at 80 K and 200 K and **(b)** zoom-in on 200 K M-H curve. Note the change in the scale of applied field.

Magnetization as a function of applied magnetic field was recorded at two temper-

atures: 80 K and 200 K as shown in fig. 7.4. There is a significant drop in the magnetization compared to magnetization obtained for 300 Å LSMO film. It was expected due to lower thickness and more defects present in the film. LSMO film with 110 Å shows a stable ferromagnetic state. Previously, the presence of a negative remanence was observed at higher temperatures of about 270 K for 300 Å LSMO layer in LSMO/PMN-PT(001) heterostructures (see chapter 6). Based on this, the M-H curves for this thickness was also measured and the negative remanence was observed for the 200 K M-H curve as depicted in fig. 7.5.

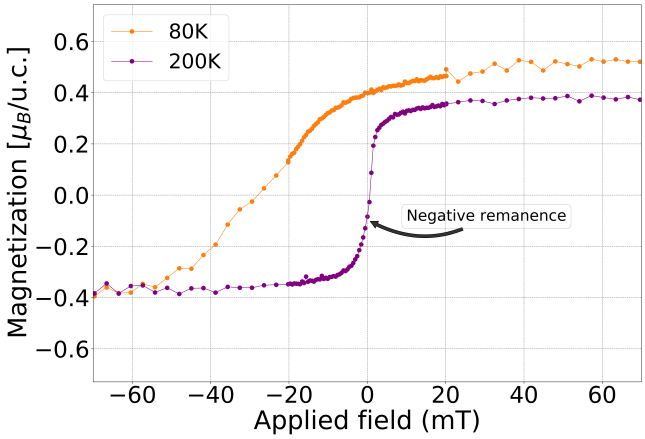

Figure 7.5: Appearance of negative remanence in M-H curve measured at 200 K.

It is interesting to note that the negative remanence effect appears close to the T_C of the film. Until now the only explanation for the presence of this effect is based on the inhomogeneous magnetism near the interface. In this case the thickness of the film is lower and has more defects as can be seen from the ZFC curve and probably due to this the negative remanence is visible for a low temperature like 200 K. These speculation are supported by the results obtained in the work of Kumari *et al.* [93] and Mottaghi *et al.* [94]. More thorough and systematic study is needed to understand the presence of negative remanence effect.

7.3 Magnetoelectric measurements

Magnetization as a function of voltage was recorded for 110 Å thick LSMO/PMN-PT(001) sample. The magnetoelectric measurements were performed at two temperatures: 80 K and 200 K as shown in fig. 7.6. No major changes were observed in the magnetization from the measurements apart from gradual increase in the magnetization. At 80 K, the magnetization increases but does not vary much compared to the results obtained for 300 Å LSMO film in fig. 6.10 in chapter 6. Also, at 200 K, one can see a little variation (marked with green circles) in the magnetization signal but not strong enough to confirmly say that there is presence of ME coupling. For such a thin film, the change in magnetization is not clearly visible. There is no pres-

ence of butterfly loop, which is expected as measurements performed are already in low temperature regime of PMN-PT(001). It becomes a bit difficult to study the influence of voltage on such a thin film of LSMO as it consists of defects as well as magnetically inhomogeneous regions. There is a plausibility of some magnetization relaxation as a function of time.

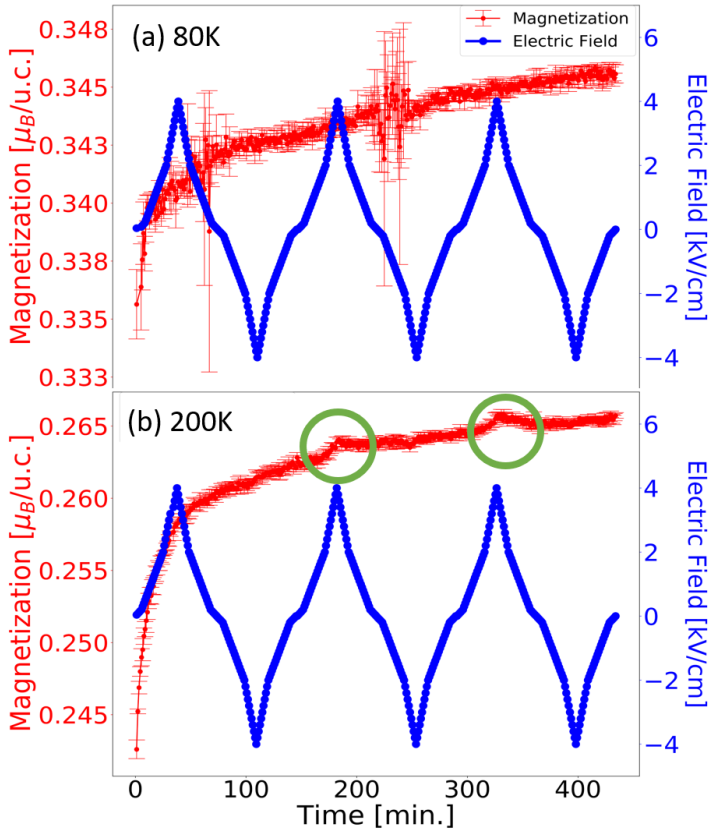

Figure 7.6: Magnetization vs electric field curves of 110Å LSMO thin film **(a)** at 80 K and **(b)** at 200 K. Green circles are showing small variation in magnetization as a function of electric field at 200 K.

7.4 Conclusion

The growth of 110 Å LSMO layer was successful with good crystalline quality. Reduction in T_C was observed compared to 300 Å LSMO layer. With decreasing thickness and presence of defects, leads to reduction of magnetization in the LSMO layer. ZFC curve demonstrates the pinning of magnetic moments which further confirms the presence of defects in the film. However, the negative remanence effect is still visible at 200 K. This indicates the existence of magnetically inhomogeneous regions

in the LSMO film. The magnetoelectric measurements demonstrate increase in the magnetization, although the variation of magnetization as a function of an applied voltage is not clearly visible, probably due to higher concentration of the defects in the film which suppresses the magnetic signal. Ultra-thin films having low magnetic signal, makes the study of magnetoelectric properties difficult.

8 Experimental Results III: Magnetic field mapping of LSMO/PMN-PT(001) by off-axis electron holography

In the previous two chapters the magnetic properties of LSMO were investigated using macroscopic measurements and scattering studies. In macroscopic measurements, magnetic properties are averaged over the whole sample volume, whereas in scattering, the magnetic depth profile is accessible by model fitting of the measured signal. In order to directly visualize and measure the magnetic field in LSMO, off-axis electron holography (EH) in TEM was carried out using cross-sectional specimens of the LSMO deposited on PMN-PT. The main advantage of using off-axis EH is that the magnetic information can be recorded alongside the microscopic structure and composition information enabling a direct comparison between magnetization profile and real-space structure. Off-axis EH in conjunction with polarized neutron reflectometry gives a holistic information on the magnetization profile of LSMO/PMN-PT(001) heterostructures.

This chapter discusses the results of off-axis EH measurements performed on LSMO/ PMN-PT(001) heterostructure as a function of temperature. The off-axis EH experiments were performed with the help of Dr. Qianqian Lan from ER-C-1. A relatively thick LSMO layer of about 500 Å was deposited, so that the magnetic signal from LSMO layer is strong enough to be recorded. The FIB specimen for the experiment was prepared by Lidia Kibkalo from ER-C-1.

8.1 Structural and magnetic characterizations

Figure 8.1 shows the LEED and RHEED patterns recorded after growth in OMBE. One observes sharp LEED spots and absence of any surface reconstruction. The presence of Laue ring with sharp RHEED spots indicates smooth surface and good crystalline quality of the LSMO layer. The heterostructure was then characterized using XRD (fig. 8.2) confirming a single phase growth of LSMO oriented along [001] direction. The zoom-in on (001) peak shows present of Laue oscillations indicating good crystalline quality of the as-grown LSMO layer. The crystalline thickness calculated from the Laue oscillations shows that 92% of the film is single crystalline.

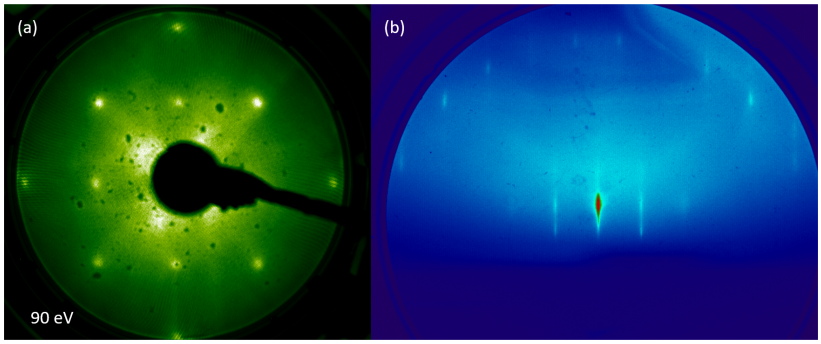

Figure 8.1: In-situ structural characterizations **(a)** LEED and **(b)** RHEED pattern of 500 Å LSMO layer on PMN-PT(001) substrate.

It was not possible to perform XRR scan on this sample as the substrate had some surface corrugation due to broad rocking curve that hinder any reflectivity measurement. Although the reflectivity measurements were not successful, the surface corrugation of the substrate didn't affect the growth and magnetic properties of the LSMO film. The quality of the as-grown LSMO is good that was further confirmed by STEM measurements on this sample.

The magnetic properties of this sample were probed by recording the magnetization as a function of temperature, as shown in fig. 8.3 (a). The M-T curve gives a Curie temperature of $T_C = 358\,K$. One still observes jump in magnetization due to Mn_3O_4 particles near 43 K, however, this effect is not as sharp as observed for 300 Å samples. This probably indicates that the ratio of Mn_3O_4 particles is reduced compared to 300 Å samples. This can arise due to stoichiometric fluctuation from sample to sample. Also, Mn_3O_4 has a good chemical compatibility with the whole perovskite manganite family, and therefore, it can nucleate in the LSMO matrix. Fig.8.3 (b) shows the magnetization hysteresis measured at different temperatures. The M-H curve shows enhanced magnetization at 300 K from $0.92\,\mu_B/u.c.$ for 300 Å to $1.55\,\mu_B/u.c.$ for 500 Å LSMO layer.

Interestingly, in an inspection of the half-cycle in M-H loops where the applied magnetic field varies from +2.5 T to -2.5 T, the presence of negative remanence (NRM) effect at 300 K was observed (fig. 8.4). The presence of NRM effect in LSMO film at room temperature has been consistent in this work. This effect was found in the LSMO/BTO/Nb:STO (001) heterostructure as well. Until now the only speculation for this behaviour has been attributed the presence of defects/oxygen vacancies in the system [93, 94]. A systematic set of experiments are required to understand the presence of this NRM effect. Nevertheless the bulk magnetic measurements confirm the stable ferromagnetic properties of the LSMO film that can be locally mapped and measured with off-axis EH in TEM.

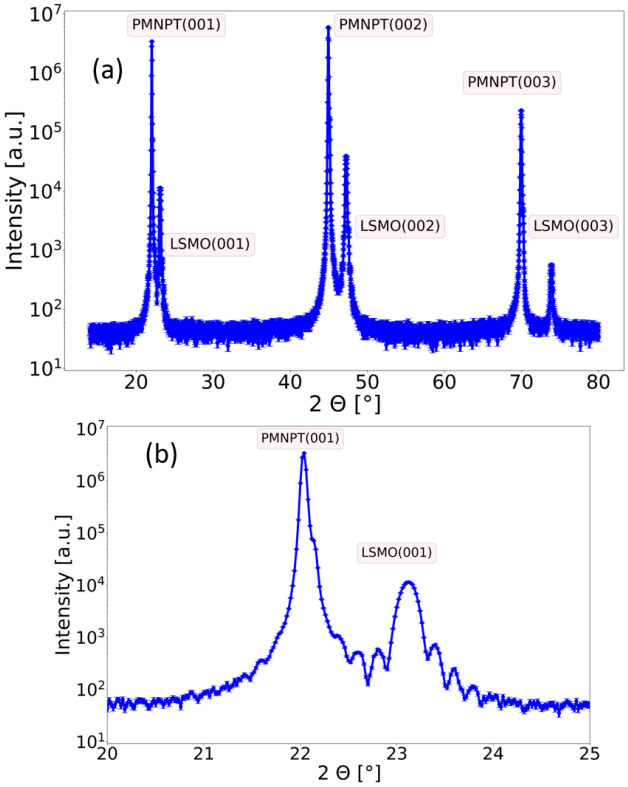

Figure 8.2: (a) XRD scan of 500 Å thick LSMO layer deposited on PMN-PT(001) and **(b)** zoom -in on the (001) peak where one can see the Laue oscillations as well.

8.2 Specimen preparation for TEM studies

Cross-sectional preparation of the LSMO samples for off-axis EH measurements were carried out using FIB sputtering in a dual-beam SEM system. The initial plan was to perform off-axis EH on two samples: one which has seen voltage and an other sample in the virgin state to study the before and after voltage effect on the magnetization of LSMO . The sample which has seen voltage was exposed to a voltage loop from 0 V $\rightarrow$ +200 V $\rightarrow$ 0 V $\rightarrow$ -200 V. Fig. 8.5 shows the secondary electron (SE) scanning electron microscopy (SEM) images of the FIB specimens. One can clearly see the major difference in the PMN-PT structures. The sample that has been exposed to voltage cycle has a lot of defects and pores compared to the virgin sample. Therefore, it became difficult to further reduce the thickness of the voltage sample for the experiment, as it was breaking apart. The off-axis EH was performed only on the virgin sample. During FIB lamella preparation, Au layer of 550 Å was deposited on 500 Å thick LSMO using sputtering to reduce the electron beam induced charging, which would hinder the imaging and sputtering processes.

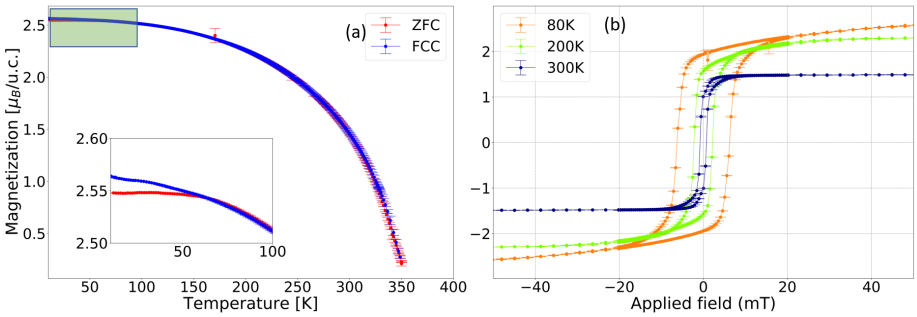

Figure 8.3: (a) ZFC and FCC measurements of the LSMO using an applied field of 50 mT. Inset is a zoom-in on the jump in magnetization due to Mn_3O_4 particles, **(b)** M-H hysteresis curves measured at 80, 200 and 300 K, respectively.

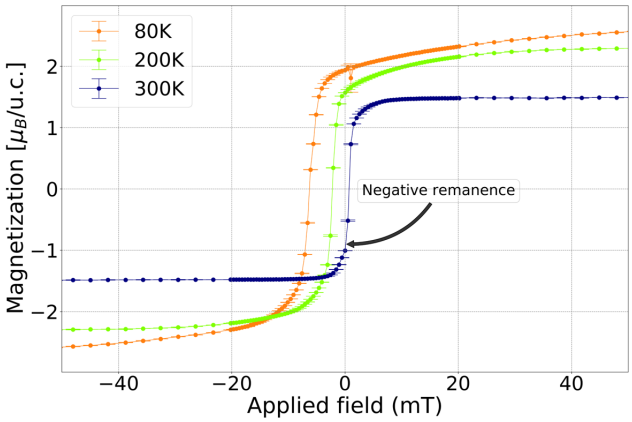

Figure 8.4: Presence of negative remanence (NRM) effect at 300 K.

In addition, a carbon layer was deposited in the FIB/SEM system as protective layer as shown in Fig. 8.6.

8.3 STEM measurement

The cross-sectional specimen was first studied using aberration-corrected HAADF-STEM imaging at 200 kV. HAADF images were recorded using a 69 mrad annular dark-field detector semi-angle that ensures the good chemical element sensitivity of the image contrast. The images in fig. 8.7 show the 500 Å LSMO layer deposited on PMN-PT(001). The specimen was aligned to the closest crystallographic zone axis using a double-tilt TEM holder. The high-resolution HAADF STEM image of the interface region (fig. 8.7(b) and (c)) reveals the epitaxial growth of LSMO on PMN-PT(001) and presence of dislocations at the interface, which formed due to the lattice

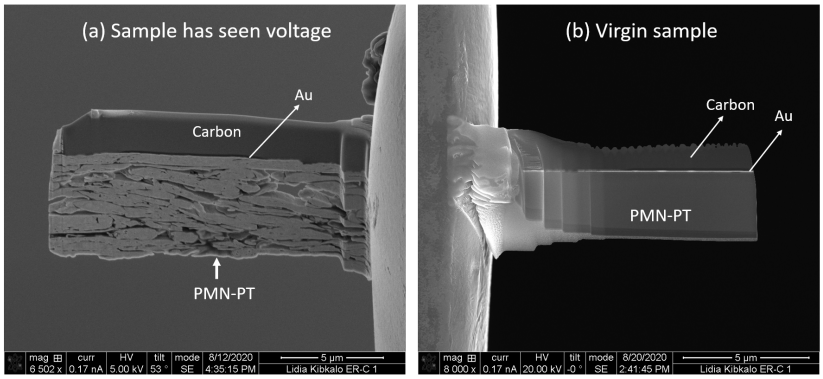

Figure 8.5: Secondary electron SEM images of FIB lamella show the cross-sections of the **(a)** sample which has seen voltage and **(b)** sample in its virgin state. The defective structure of the sample that has seen voltage prevented the specimen preparation.

mismatch between the two structures. In HAADF STEM images, the presence of Mn_3O_4 particles was not observed as in 300 Å LSMO/PMN-PT(001) samples (see chapter 6). As one still observes a small jump in magnetization in FCC curve (fig. 8.3), this indicates that there are still a few Mn_3O_4 particles present although the amount is drastically reduced or the size is very small. Since the formation of the Mn_3O_4 particles is an intrinsic property of Mn-excess LSMO films, therefore, the amount can vary from sample to sample.

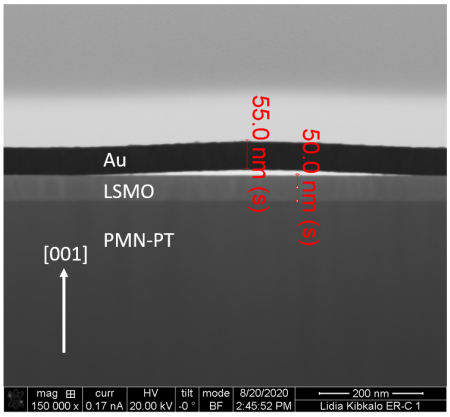

Figure 8.6: Bright field SEM image shows the continuous 500 Å thick LSMO layer deposited on PMN-PT substrate and coated with 550 Å Au layer.

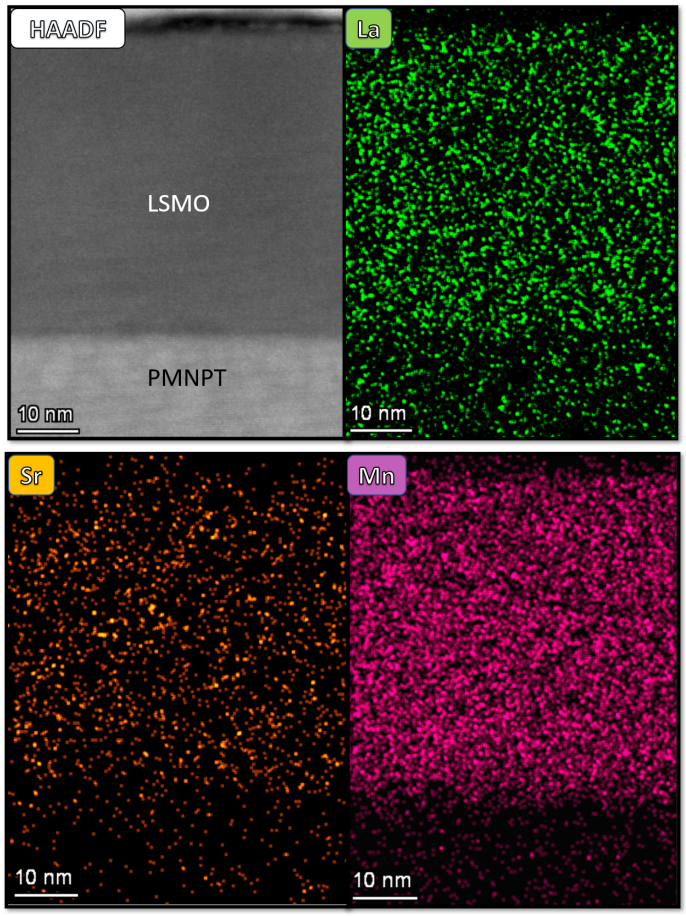

Figure 8.8: STEM-EDX maps of La (green), Sr(orange) and Mn(pink) in LSMO/PMN-PT(001) heterostructure.

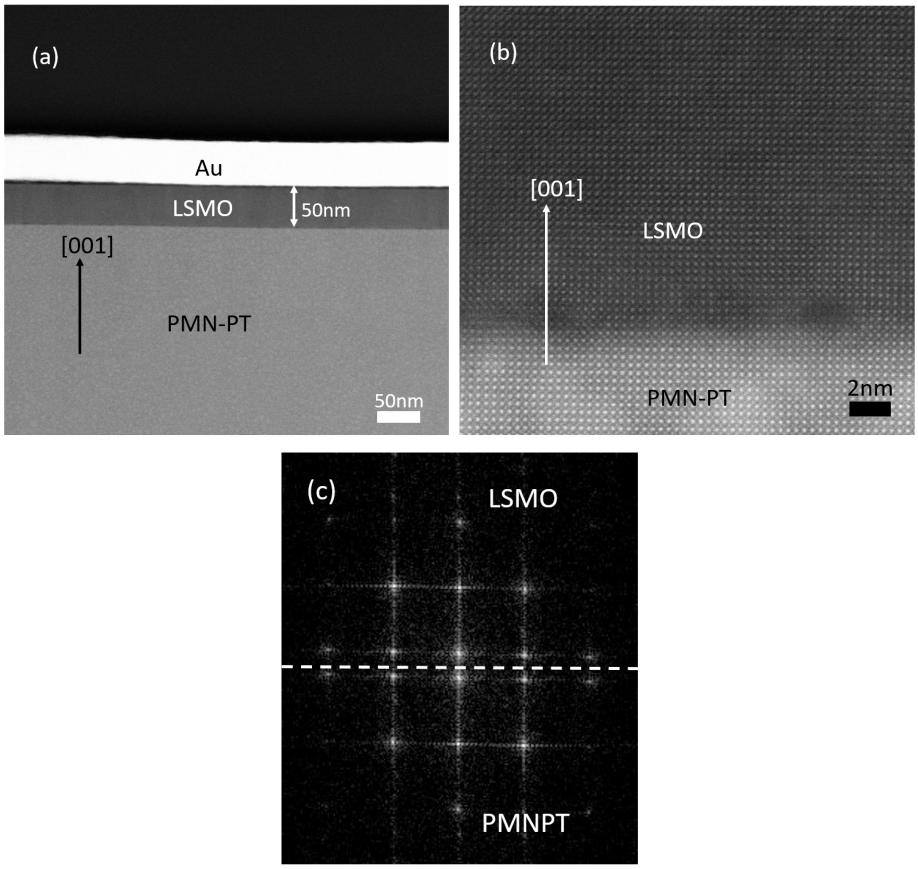

Figure 8.7: (a) HAADF STEM image shows the overview of the LSMO/PMN-PT(001) heterostructure. **(b)** High-resolution HAADF STEM image of the interface region showing the lattice match between the LSMO and PMN-PT. The dark contrast regions at the interface indicate the presence of dislocations that formed due to lattice mismatch between the LSMO and PMN-PT. Note the Mn_3O_4 particles are not visible in the 500 Å thick LSMO layer. **(c)** Composite image of two FFTs taken from LSMO and PMN-PT showing the epitaxial interface.

The EDS maps (fig. 8.8) recorded together with STEM image reveal homogeneous LSMO film. In La and Sr map one observes some signal in PMN-PT region also. This is because the peak for La and Ti are very close.Thus, on selecting La in EDS map, the signal from Ti is also induced and one sees intensity in PMN-PT. For Sr-map, it is a processing artifact.

8.4 Off-axis electron holography

The magnetic field of the LSMO layer was quantitatively measured by off-axis EH. The measurements were carried out using magnetic field free mode of the transmission electron microscope operated in 300 kV using an image-C_S-corrected FEI Titan 80-300 TEM [107]. The LSMO specimen and its temperature was controlled using a double-tilt liquid nitrogen cooled TEM holder (Gatan model 636) from room temperature down to 94 K. Electron holograms are created and recorded using a single electron biprism and a direct electron counting detector (Gatan K2 IS). The specimen was aligned in a way that the biprism was perpendicular to the LSMO layer, thus the reference region was taken from the vacuum region adjacent to the specimen edge. Beside the specimen hologram, a reference hologram was recorded from the empty vacuum region, in order to remove the imaging distortions [62].The specimen was slightly tilted away from the main zone axis to avoid strong diffracting conditions [64, 108]. Electron holograms were recorded in magnetic field free conditions using a direct electron counting camera. The data processing was performed by Dr.Qianqian Lan from ER-C-1. Fig. 8.9 (a, b) show the specimen and the reference holograms of the LSMO specimen recorded at 200 K with fringe spacing of 0.86 nm. The Fourier transform (fig. 8.9 (c)) recorded from the specimen hologram shows the center and two conjugate side bands.

One of the two sidebands is then digitally selected and its inverse Fourier transform is calculated which provides a real-space complex wave image that contains both amplitude and phase information [109]. The phase, ϕ of the electron wave function can then be directly calculated by evaluating the arctangent of the ratio of the imaginary and real parts of the resulting real space complex wave function. The obtained phase shift was evaluated modulo 2π, which means that 2π discontinuities unrelated to specimen features appear at the positions where the phase shift exceeds this amount. The phase image(fig. 8.11) was unwrapped using suitable algorithms to remove wrapping errors. Considering that neither the electrostatic potential , V, nor magnetic induction component perpendicular to the optical axis, $B_\perp$, varies along the electron beam direction with a sample of thickness, t and length of the sample, x (fig. 8.10), the equation 4.21 can be written as

$$\phi(x) = C_E V(x) t(x) - \frac{e}{\hbar} \int_{AB} \int_{CD} B_\perp \cdot dA \tag{8.1}$$

where, C_E is an interaction constant and ABCD is the surface defined by the paths

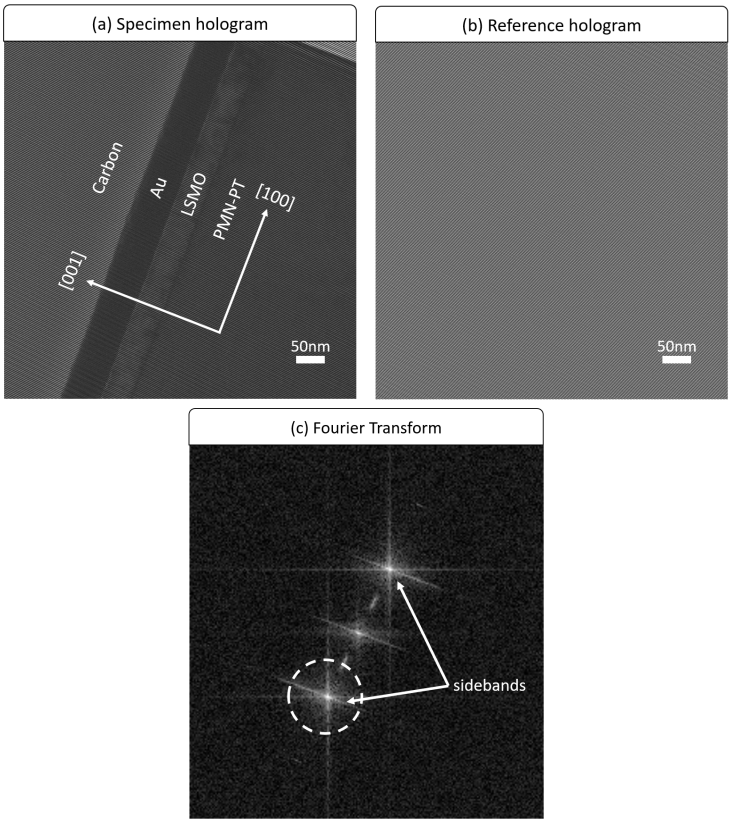

Figure 8.9: Off-axis EH measurement of the cross-sectional 500 Å LSMO layer. **(a)** Specimen and **(b)** reference hologram recorded at 200 K. **(c)** Fourier transform of the specimen hologram. Dashed circle mark the size of the virtual aperture used to process the phase information.

of the object and reference beams as shown in Fig. 8.10. Further simplifying it

$$\phi(x) = C_E V(x) t(x) - eB_\perp x \frac{t}{\hbar} \tag{8.2}$$

Taking the specimen thickness t and composition to be constant, the derivative of phase can be written as

$$\frac{d\phi(x)}{dx} = eB_\perp \frac{t}{\hbar} \tag{8.3}$$

Equation 8.3 shows that the slope of the phase is proportional to the perpendicular component of the magnetic field within the specimen i.e., regions of constant slope correspond to uniform magnetic field in the specimen [108].

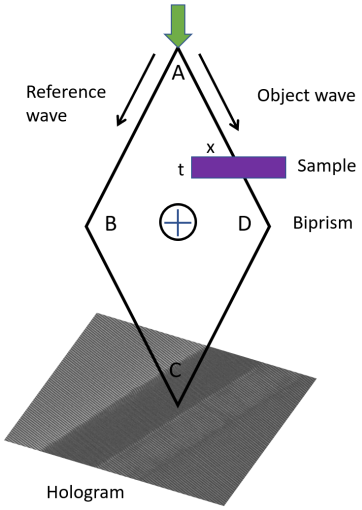

Figure 8.10: Schematic of path integral in off-axis electron holography used to recover the phase information. Inspired from [108].

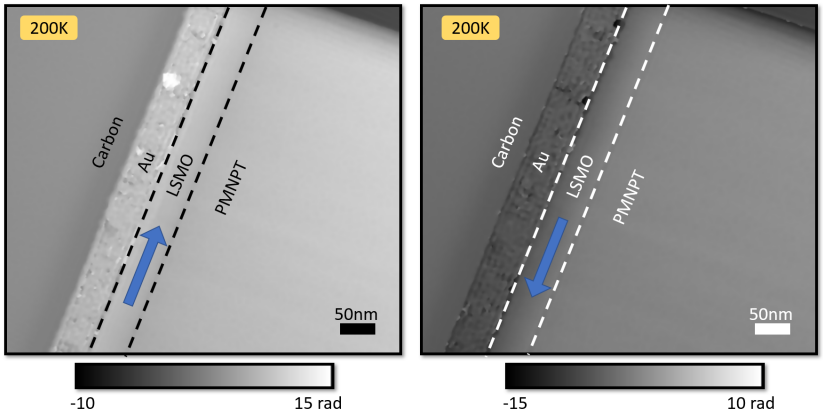

Figure 8.11: A pair of reconstructed phase images of LSMO/PMN-PT(001) heterostructure recorded at 200 K. They were obtained by sequentially magnetizing the lamella parallel and antiparallel to the interface by tilting the specimen away from main zone axis **Left:** -65° (parallel) and **Right:** +65° (antiparallel) and applying a 1.4 T field. Blue arrow depicts the direction of saturating field.

The obtained phase shift contains both the electrostatic and magnetic contributions. Since one is interested in characterizing the magnetic fields in the specimen, it becomes crucial to remove the contribution of mean inner potential from the measured phase shift to interpret the magnetic contribution. To do this, pairs of electron holograms were recorded that differ only in the (opposite) directions of the magnetization in the specimen as shown in fig. 8.11. The magnetic and mean inner

potential contributions to the phase can then be calculated by taking half the difference and half the sum of the reconstructed total phase images. As the magnetic phase shift is directly proportional to the in-plane magnetic induction, it can be visualized by applying a cosine multiple of the magnetic phase as shown in fig. 8.12 (c). The phase shift in Au layer appears to be higher than LSMO in fig. 8.12 (b), which is an artifact of the processing. Au diffracts heavily and due to large atomic number the electron wave doesn't really go through it. The information from the Au layer is mostly a noise. Since it is not magnetic, therefore, its phase shift cannot be higher than LSMO and in principle should be zero as no magnetic phase shift exists there.

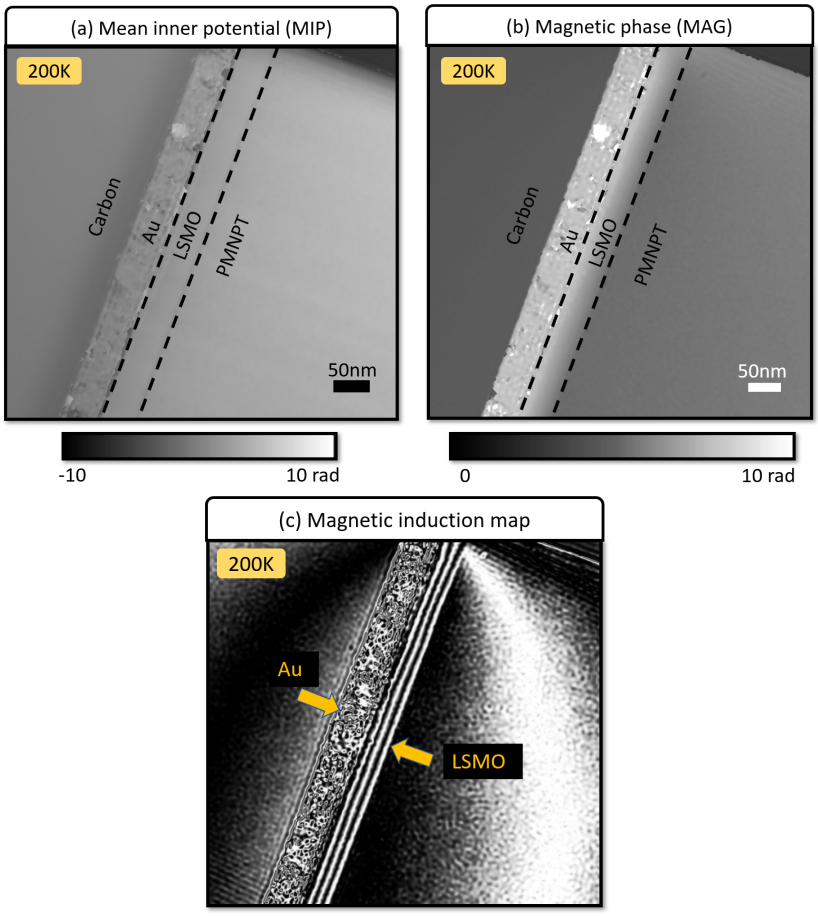

Figure 8.12: (a) Mean inner potential (MIP) and **(b)** magnetic phase shift maps of the LSMO layer recorded at 200 K. **(c)** Magnetic induction map obtained by applying a cosine function on the phase shift. The contour spacing is 1.57 radian.

In general, as the electron wave propagates through a magnetic field in LSMO, it experiences a Lorentz force, thereby inducing a phase shift which is given by the

enclosed magnetic flux integrated along the beam direction. This magnetic field in LSMO introduces a phase shift perpendicular to the field direction. The phase shift is a slope function. Based on the assumption that the magnetic field does not vary along the beam direction, the magnetic flux lines and density can be visualized by contour lines by applying a cosine function on the slope which is shown by magnetic induction map in fig. 8.12c.

The off-axis EH experiments were carried-out at three different temperatures, namely at 94 K, 200 K and 295 K, respectively (fig. 8.13). The FCC curve was recorded with applied field of 50 mT, but for EH experiments, the sample was first saturated with applied magnetic field of 1.4 T and then the remanent magnetization of LSMO was recorded in the magnetic field free conditions.

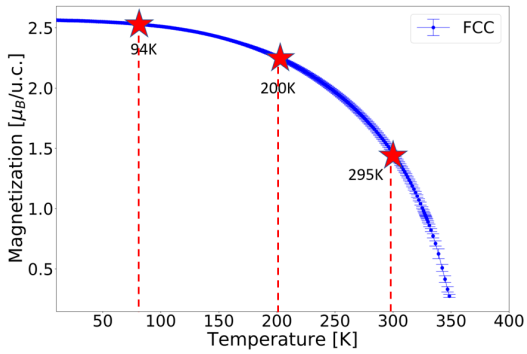

Figure 8.13: FCC curve of LSMO/PMN-PT (001) heterostructure with applied field of 50 mT. Red stars mark the temperatures at which off-axis EH experiments were carried out in magnetic field free conditions. The value of magnetization shown in this plot are obtained from SQUID-MPMS measurements.

The magnetic phase shift measurements obtained at different temperatures are shown in fig. 8.14 with their corresponding induction maps are presented side-by-side. The magnetic induction lines arranged parallel with the LSMO layer and were created by displaying the cosine of a multiple of the magnetic phase image. These induction maps were 4 times amplified that gives a contour spacing of $2\pi/4 = 1.57$ radians for all three temperatures. However the density of the induction line decreases as the temperature increases confirming a similar behavior of the magnetic properties in the cross-sectional LSMO specimen as observed in the magnetometry measurements of the bulk sample (fig. 8.13). The experimental magnetic phase shift was further analyzed by taking a line profiles across the maps (red arrows in fig. 8.14) recorded at different temperatures as shown in depicted in fig. 8.15. The analyses shows that the calculated magnetic phase change at 94 K, 200 K and 295 K are 3 radians, 2.5 radians and 1.4 radians through 500 Å LSMO layer, respectively. As discussed above, the constant shape of the slope in line profiles suggest a uniform magnetic field in the whole layer along the growth direction (fig. 8.15). The magnetic phase gradient at 295 K is very low compared to other two temperatures revealing a reduction of magnetization. The magnetic phase gradient is

linearly proportional to the magnetization of the LSMO, thus one observes reduction of magnetic phase gradient as the temperature approaches the room temperature. This result is in good agreement with the macroscopic magnetization measurements see chapter 6 fig. 6.7. The phase shift profile at 295 K shows a ramp for Au, which is an artefact. Since Au is not magnetic, it cannot have a magnetic phase shift. In contrast to PNR measurements, one does not observe presence of any interlayer in this experiment. However, one has to mention that due to the limitation of spatial resolution at these experimental conditions, it is difficult to resolve features with less than 100Å thickness. From previous results (chapter 6, 7), one knows that the thickness of interlayer is less than 100Å, thus not visible in EH experiments. To probe the presence of interlayer, further experiments are required.

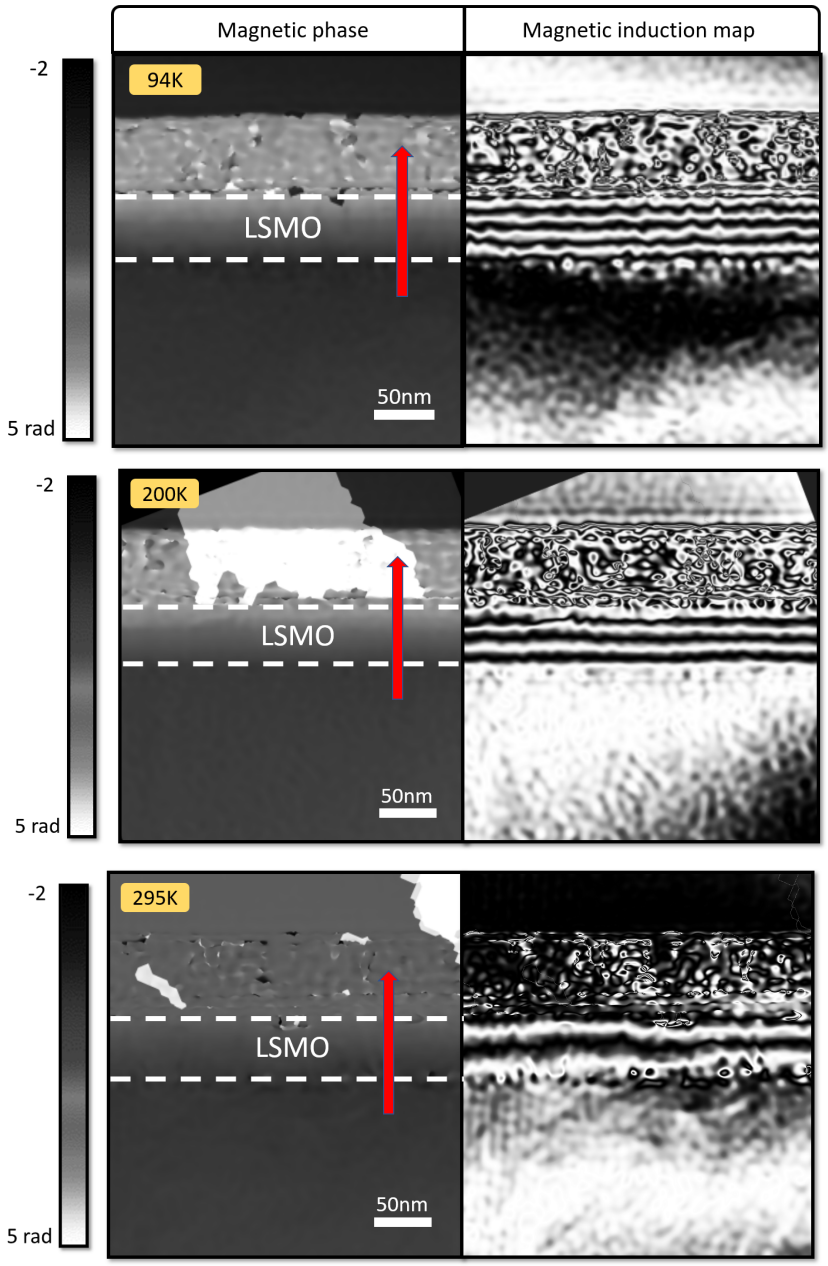

Figure 8.14: Magnetic phase shift maps of the heterostructure and the corresponding magnetic induction maps depicting the uniform magnetic field in LSMO parallel to the substrate at 94 K, 200 K and 295 K. The contour spacing is 1.57 radians for all temperatures. The red arrow indicate the location of the analysis presented in fig. 8.15.

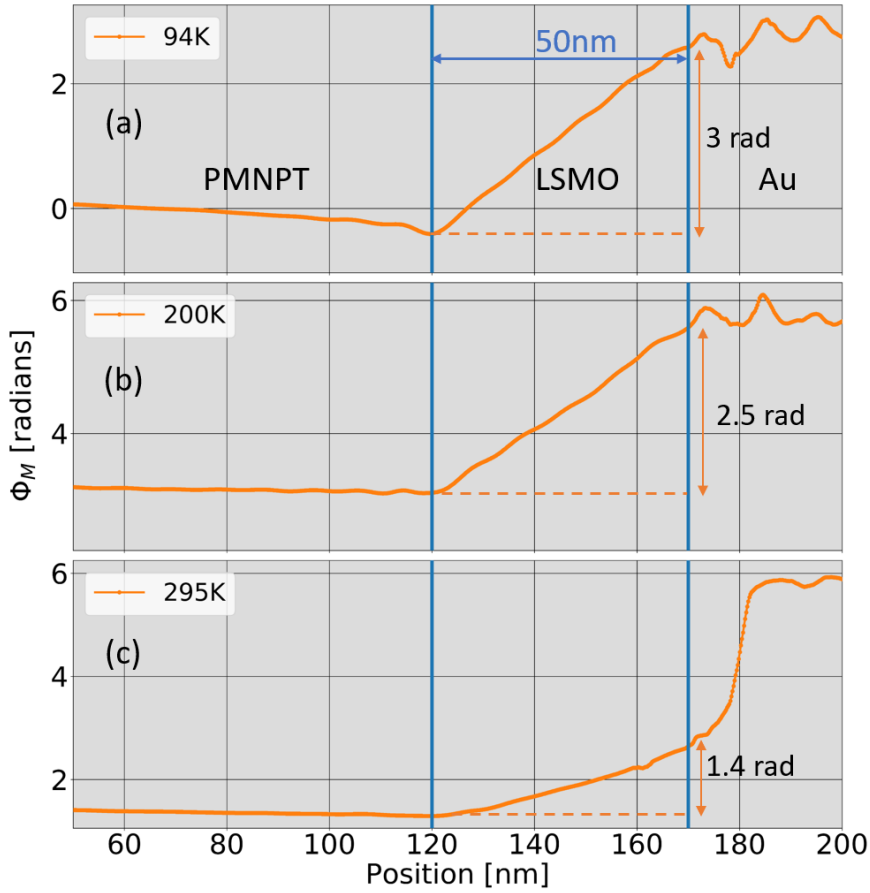

Figure 8.15: Line profile of magnetic phase shifts taken along the red arrow in Fig. 8.14 depicting the presence of a uniform magnetic field in LSMO through the whole layer (perpendicular to the substrate) at **(a)** 94 K with magnetic phase change of 3 radians **(b)** 200 K with magnetic phase change of 2.5 radians and **(c)** 295 K with magnetic phase change of 1.4 radians.

8.5 Conclusion

500 Å thick LSMO layer was successfully grown on PMN-PT(001) substrate with good crystalline and ferromagnetic properties. The STEM measurements show single crystalline and epitaxial LSMO film with dislocations at the interface that formed due to lattice mismatch between the film and the substrate. The FCC measurements of the bulk sample show reduction in the amount of Mn_3O_4 particles. Also, in STEM measurements the Mn_3O_4 particles are not clearly visible which agrees well with the FCC results as formation of these particles is intrinsic property of Mn-excess LSMO

films which can vary from sample to sample. One still observes presence of NRM effect at 300 K M-H curve. The temperature dependent study of remanent magnetization in LSMO with off-axis EH shows homogeneously magnetized LSMO layer. Due to the structural damage of the voltage exposed sample, it was not possible to prepare FIB specimen for off-axis EH experiment. Therefore, only on the virgin LSMO/PMN-PT(001) heterostructure was studied. The presence of homogeneous remanent magnetic field in LSMO layer is consistent with the PNR measurements. Due to the limitation of spatial resolution, one is unable to probe the presence of interlayer as it is only about few angstroms thick. The remanent magnetic field in LSMO layer reduces as a function of temperature which is in good agreement with the macroscopic magnetic measurements.

9 Experimental Results IV: Growth of $BaTiO_3$ thin film

This chapter discusses the calibration of growth parameters for $BaTiO_3$ (BTO) thin film using HOPSS. The BTO thin films were then integrated with LSMO film with the aim to study ME coupling with this artificial multiferroic heterostructure. The LSMO/BTO heterostructure was studied structurally and magnetically. Also, ferroelectric properties of BTO were studied.

9.1 Motivation

$BaTiO_3$ (BTO) is a typical ferroelectric material which is non-volatile in nature compared to Pb-based or Bi-based ferroelectrics and thus, can be used for semiconductor fabrication facilities without having any environmental issues. The idea of LSMO/BTO was first predicted by Burton *et al.* [110] who demonstrated using first principle calculations, that by choosing the x-doping level near the magnetic phase transition in $La_{1-x}Sr_xMnO_3$ ($x \approx 0.5$), one can change the magnetic order at the interface from FM to AFM by switching the ferroelectric polarization of BTO. Based on this idea, Dr.Markus Schmitz [70, 111] used BTO as a ferroelectric substrate and deposited LSMO film on BTO to study ME coupling in LSMO/BTO. He was able to demonstrate manipulation of magnetism in LSMO as function of temperature and electric fields. BTO substrate showed structural phase transitions leading to structural distortions. The only problem with using BTO as a substrate is the structural phase transitions which result in different magnetic and electronic properties for every structural distortion. With structural distortion, the FE domain state also changes making the understanding of ME coupling complex and asymmetric. Therefore, it becomes crucial to find a way where one can prevent structural distortions along and obtain single domain properties. These problems can be solved by growing a thin film of BTO. Choi *et al.* [112], reported stable tetragonal phase of BTO thin film of thickness 500 Å in the temperature range of 298 K - 973 K.

9.2 $BaTiO_3$ on $SrTiO_3$ (001)

For initial deposition of BTO layers, the parameters were taken from Prof. Michael Faley and his student Sheng Cheng from PGI-5. They helped for the initial process

of growth as they use the same HOPSS system for their thin film growth.

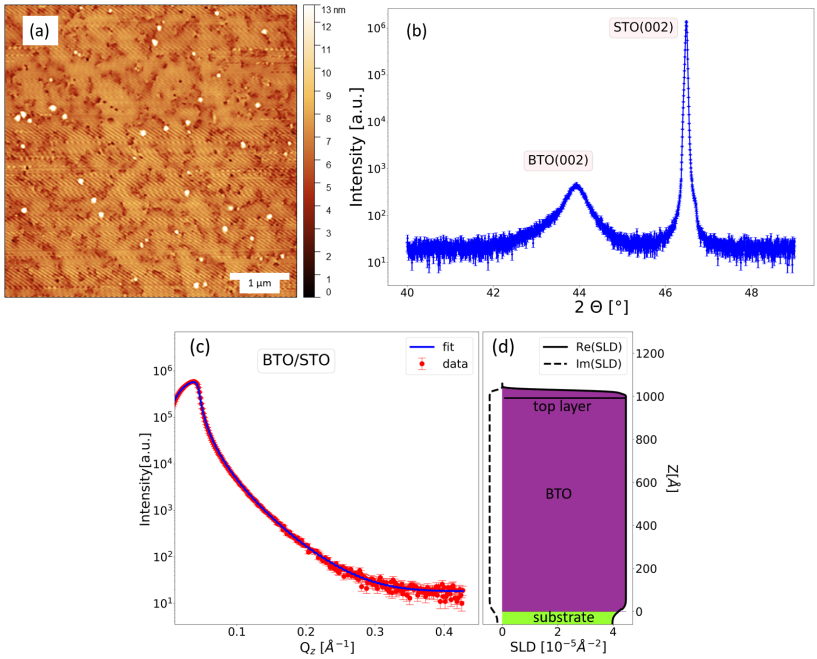

Figure 9.1: (a) Topographic image obtained from AFM, **(b)** X-ray diffraction scan of BTO layer deposited on STO(001) substrate, **(c)** XRR measurement showing at least 1000 Å thick BTO layer and **(d)** SLD profile deduced from the XRR measurement.

For the calibration of growth parameters for BTO layer, $SrTiO_3$, STO(001) with dimensions of 10×10×0.5 mm substrate was used. The STO substrate was first washed with acetone and ethanol with ultrasonication for three times. It was then annealed for 7200 s at 1000 °C in the sputter chamber with oxygen pressure of 1.2 mbar . The BTO target was pre-sputtered with RF power of 100 W for 7200 s. Pre-sputtering helps to get rid of any contaminant present on the surface of the target. For newly bought targets, one should pre-sputter the target overnight to get rid of any organic contaminants sticking on the target surface. For the growth of BTO, the temperature was reduced to 750 °C and the target was then positioned over the substrate to start the deposition. The deposition time for this sample was 9000 s and after the deposition, sample was annealed in oxygen atmosphere at 450 °C for 1800 s. The sample was cooled at the rate of 5 K/min and then it was taken out of the sputter chamber.

Fig. 9.1 shows the structural characterizations performed on this sample. The AFM topography (fig. 9.1 (a)) shows the presence of some islands and holes with the surface roughness of 23 Å. The lattice mismatch between BTO (a = 4.01 Å) and STO (a = 3.905 Å) is about -2.6% which means BTO experiences in-plane compressive strain imparted from STO. From the XRD scan (fig. 9.1 (b)), the

deduced out-of-plane lattice parameter is c= 4.11 ± 0.003 Å. Assuming a constant volume of BTO unit cell , one can calculate the in-plane lattice parameter which comes out to be 3.96 ± 0.002 Å, thus film is partially relaxed while retaining -1.4% strain which causes this increase in out-of-plane parameter. One should perform Reciprocal Space Mapping (RSM) to confirm. The XRD scan depicts that BTO is in single phase which is tetragonal. The tetragonal phase can possess both c- and a-domain. If there was presence of both domains one would have observed another Bragg reflection near (002) peak at slightly higher angle and since this is not the case one can say BTO is in single phase with c-domains and is epitaxially oriented along [001] direction. To determine the thickness of as-deposited BTO layer, XRR (fig. 9.1 (c)) measurement was performed where one observed no oscillations. Based on the expected model, the fitting was performed using GenX which gave the SLD profile (fig. 9.1 (d)) with BTO layer thickness of atleast 1000 Å, a toplayer of thickness 19 Å and roughness of 15 Å. Since the thickness of BTO layer is too high to be resolved by the X-ray reflectometer, that's the reason of observing no oscillations. Therefore based on fitting the thickness of BTO layer is atleast 1000 Å or possibly higher. Based on these results, some changes in parameters were made as follows: deposition time was reduced to 4500 s to reduce the thickness and the growth temperature was raised to 850 °C and the post-annealing temperature was raised to 700 °C. The rest of the parameters were kept same. The structural characterization of this sample is shown in fig. 9.2.

Topographic scan from AFM (fig. 9.2 (a)) depicts the surface of the film consisting of holes. The RMS roughness of $\sigma_{rms} = 7.37 \pm 0.08$ Å is obtained from the AFM scan. The XRD scan (fig. 9.2 (b)) depicts epitaxial growth of BTO along [001] direction and the calculated out-of-plane lattice parameter is $c = 4.20 \pm 0.004$ Å. Using this value of c, the in-plane lattice parameter comes out to be $a = 3.908 \pm 0.002$ Å which is very close to the in-plane lattice parameter of the substrate STO, $a = 3.905$ Å. This indicates that the film is nearly epitaxial along in-plane direction also. It is known that with increase in the film thickness, the strain starts relaxing whereas for lower thicknesses [112], it is possible to achieve coherently strained and epitaxial films. The thickness deduced from XRR measurement(fig. 9.2 (c)) is $95^{+4.2}_{-2.4}$ Å with the roughness of 7.4 ± 0.2 Å which matches well with the AFM roughness. However, one observes reduced SLD of $3.97 \times 10^{-5}\text{Å}^{-2}$ (fig. 9.2 (d)) for BTO layer compared to the theoretical value of $4.44 \times 10^{-5}\text{Å}^{-2}$. This is probably due to the presence of holes as one can see from the AFM scan and also the presence of defects/oxygen vacancies is plausible which will affect the SLD of BTO layer. After the deposition of these sample, there was a problem with the plasma in the sputter chamber due to which plasma was unstable. The sputter system was opened up and Frank Gossen repaired some electrical connections and checked for any leak. Once the system was repaired, the sample preparation was resumed but one observed change in the deposition rate of the BTO layer. It changed from 1Å/45s to 1Å/12s after fixing the plasma problem. Since, there was some problem with the electrical connection, its possible that the deposition from the BTO target was not uniform due to which the increase in deposition rate is observed.

This sample was deposited at 850 °C with 1.2 mbar of oxygen pressure for 3600 s.

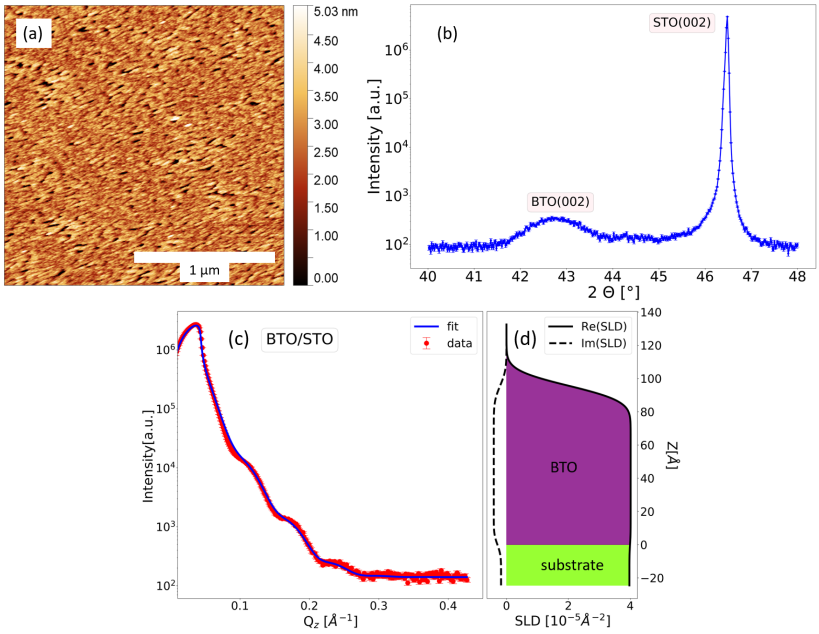

Figure 9.2: (a) Topographic image obtained from AFM, **(b)** X-ray diffraction scan of BTO layer deposited on STO(001) substrate, **(c)** XRR measurement showing 95 Å thick BTO layer and **(d)** SLD profile deduced from the XRR measurement. The XRR fitting parameters are mentioned in supplementary material in table. S6.

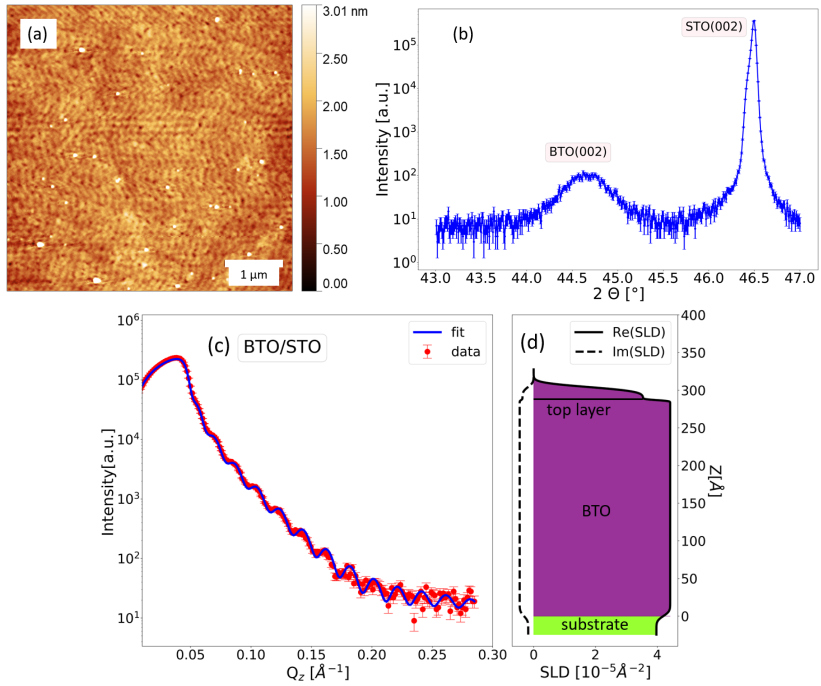

Figure 9.3: (a) Topographic image obtained from AFM, **(b)** X-ray diffraction scan of BTO layer deposited on STO(001) substrate, **(c)** XRR measurement showing 300 Å thick BTO layer and **(d)** SLD profile deduced from the XRR measurement. The XRR fitting parameters are mentioned in supplementary material in table. S7.

The sample was then post-annealed like previous samples. From the topographic AFM scan in fig. 9.3 (a), one observes presence of a few holes and islands on the surface of the film giving RMS roughness of $\sigma_{rms} = 2.89 \pm 0.17$ Å. The XRD scan (fig. 9.3 (b)) gives $c = 4.05 \pm 0.003$ Å for single crystalline BTO layer. XRR measurement (fig. 9.3 (c)) gives thickness of $286^{+6.2}_{-0.7}$ Å for BTO layer and $17.3^{+0.4}_{-3.3}$ Å thickness of top layer with reduced SLD (fig. 9.3 (d)) and roughness of $4.71^{+0.3}_{-3.1}$ Å. With such low roughness, one can say the film is smooth and flat.

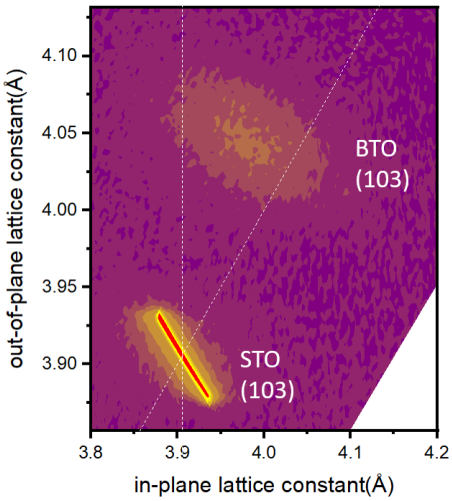

Figure 9.4: Reciprocal space map (RSM) of BTO/STO sample to determine the strain status, performed by Dr. Gregor Mussler and Dr. Alexander Shkurmanov from PGI-9.

Reciprocal space maps (RSM) can provide information about the strain in heterostructures by measure the in-plane lattice constant of the film and the substrate. If the film is fully strained, then the peak of in-plane lattice parameter of substrate will be in-line with the film peak. However, in our case the film is partially relaxed as one can see from the broadening of BTO peak. The RSM was performed along (103) reflection which gives in-plane lattice parameter $a = 3.982 \pm 0.002$ Å and out-of-plane parameter $c = 4.046 \pm 0.002$ Å for BTO film. The value of c agrees well with the XRD measurement.

9.2.1 Ferroelectric properties of $BaTiO_3$ thin film

Ferroelectric properties of BTO were probed using PFM from PGI-6. The PFM image is recorded after applying bias to study the ferroelectric nature of BTO deposited on STO(001) as shown in fig. 9.5. The bias was applied from -5 V to 5 V on different areas on the scan as depicted in fig. 9.5 (b). This means that the FE polarization will align along the applied voltage i.e., FE polarization will point downwards for -5 V and upwards for +5 V as can be seen from fig. 9.5 (c). One can observe the 180 ° phase reversal of the FE polarization based on the applied voltage. The amplitude image (fig. 9.5 (d))shows maximum at the domain boundary between the poled regions in BTO film.

The amplitude for both types of domains stays constant as can be seen from the amplitude image. This is a proof of a homogeneous poling process of the BTO film. There is prominence of domain boundaries in the amplitude image due to change in

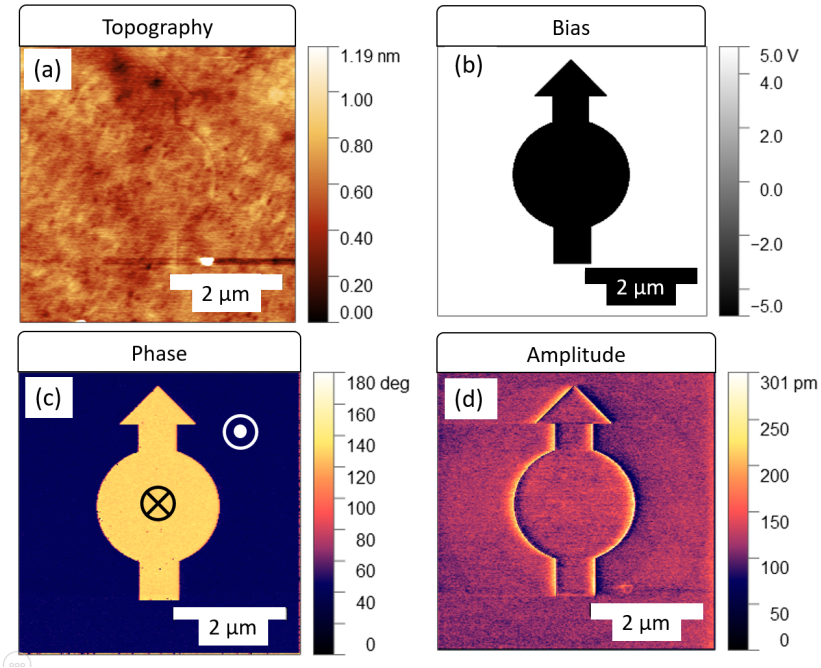

Figure 9.5: PFM imaging with applied bias depicting **(a)** topography, **(b)** bias applied over the scan area, **(c)**, corresponding phase image and the **(d)** amplitude image of BTO.

the polarization direction [113]. The FE polarization switching in PFM image is not a sufficient proof for the intrinsic ferroelectricity. However, the retention of switched polarization in a system can distinguish between a FE and a non-FE system [114]. Therefore, another measurement was performed after removing the applied bias to check the status of FE polarizations in BTO thin film.

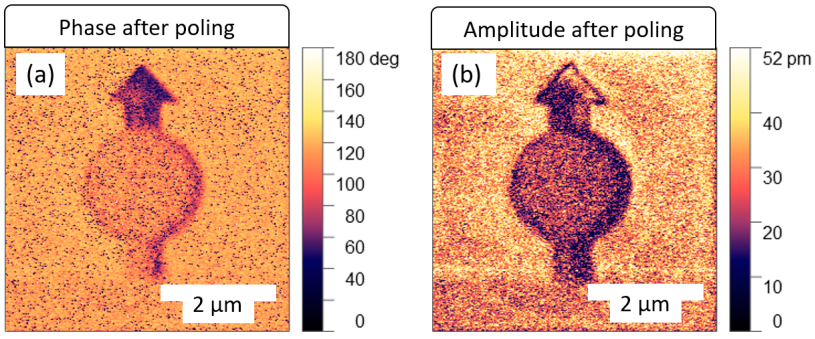

Figure 9.6: PFM imaging after removing the bias depicting **(a)** phase and **(b)** amplitude.

From the fig. 9.6, one can see that after removing the bias, one observes a partial retention of FE polarizations. A fraction of domains were able to retain their switched state. This indicates that the BTO is FE in nature. One has to mention that PFM is a microscopic technique localized to the probed region of interest. Therefore, one should also measure the polarization hysteresis of the BTO film and also check the leakage current in the film. BTO as thin film is strongly prone to leakage currents caused by the presence of oxygen vacancies.

9.3 LSMO/BTO/Nb:STO(001)

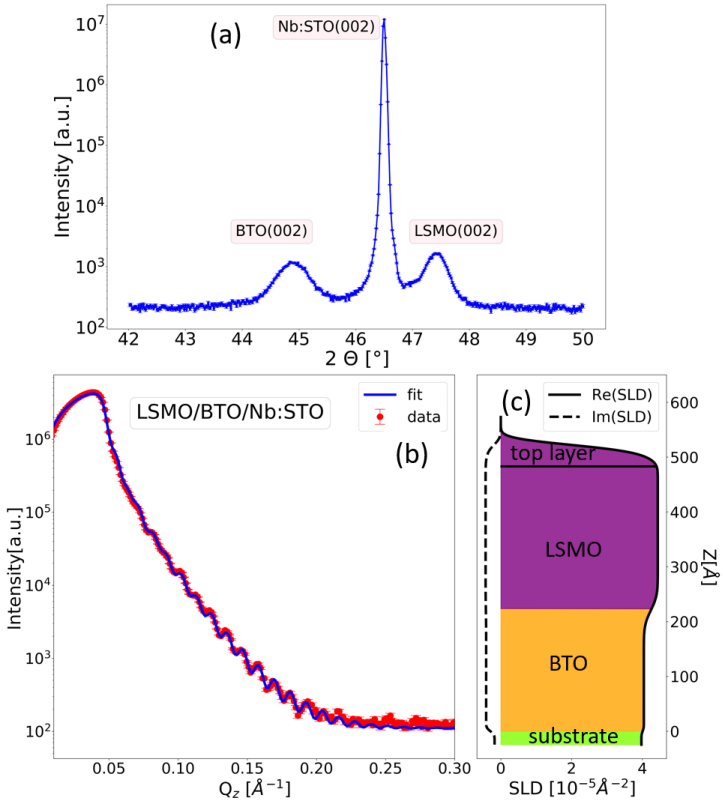

Figure 9.7: (a) XRD scan of LSMO/BTO/Nb:STO(001) heterostructure and **(b, c)** XRR scan with SLD profile. The XRR fitting parameters are mentioned in supplementary material in table. S8.

In the next, LSMO layer was deposited on single crystalline BTO thin film. As the main goal was to grow a FM/FE heterostructure where one could apply voltage to the sample to study magnetoelectric coupling effects, Nb doped STO (Nb:STO (001)) is chosen as the substrate to serve as bottom electrode. The Nb:STO substrate was annealed at 1000 °C, same as earlier and the growth temperature used

was 900 °C. The BTO film was deposited for 2700 s with the oxygen pressure of 1.17 mbar. After the growth, the sample was post-annealed. For depositing LSMO over BTO layer, the sample was transferred from the sputter chamber to OMBE chamber. Since the substrate size used for this sample was 5×5 mm compared to usual 10×10 mm, so a different sample holder had to be used for OMBE. This sample holder contains 2 slots: one for 5×5 mm and other for 10×10 mm sample.

Fig. 9.7 shows the recorded XRD and XRR scan for this sample. The calculated value of out-of-plane lattice parameters for LSMO and BTO are $c_{LSMO} = 3.83 \pm 0.002$Å and $c_{BTO} = 4.03 \pm 0.003$Å. From the XRD scan, one can see that both the layers are in single phase and are epitaxially oriented along [001] direction. From the XRR scan, the model used contains BTO layer, LSMO layer and the top layer. The thicknesses and roughness deduced from the measurement are BTO thickness: $220^{+8.2}_{-0.1}$ Å with a roughness of $21^{+11.1}_{-0.7}$ Å, LSMO thickness: $284^{+12.2}_{-9.2}$ Å with a roughness of $12^{+4.6}_{-0.7}$ Å and top layer thickness:18 Å with reduced SLD. From the roughness parameters one can see that the interface of LSMO and BTO is not very smooth.

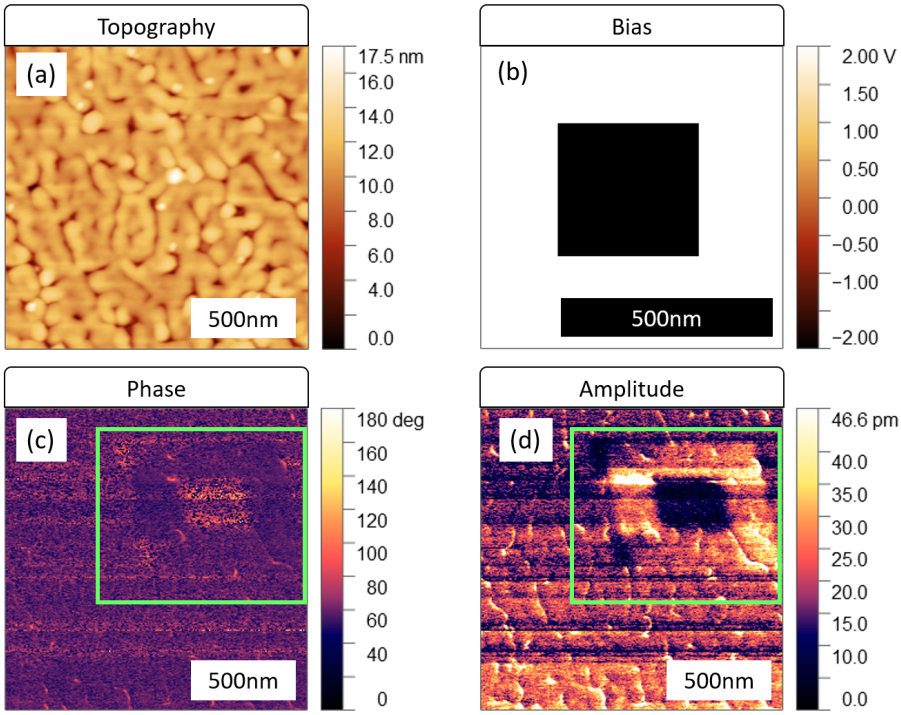

Figure 9.8: PFM scan showing **(a)** topography, **(b)** applied bias , **(c)** phase and **(d)** amplitude of the LSMO/BTO/Nb:STO(001) heterostructure. The area marked in green square shows the region where bias was applied.

The PFM scan shown in fig. 9.8 depicts presence of holes and islands on the film surface. A bias of ±2V was applied to the sample and after removing the bias,

one was able to observe switching of ferroelectric polarizations as can be seen in the phase and amplitude image marked with green square. For fig.9.8 c and d, the mapped area is larger than the region where bias was applied. The larger area was mapped to observe the switched FE domains. One can apply higher bias than ±2 V to observe stronger switching behaviour of FE domains and for better visibility. The retention of switched ferroelectric domains represents the intrinsic ferroelectricity of BTO layer. With these measurements, one can say that, it is possible to grown LSMO/BTO heterostructure with BTO possessing ferroelectric properties. However, one still needs to check for the presence of leakage currents. Since the sample growth was performed using two different deposition methods (Sputtering and OMBE), it is possible that during the transfer of the sample from sputter chamber to OMBE chamber, the surface of BTO became rough, hence the interface roughness. In future, one can try to grown both LSMO and BTO layers in sputtering and check the structural properties.

9.4 Magnetometry measurements

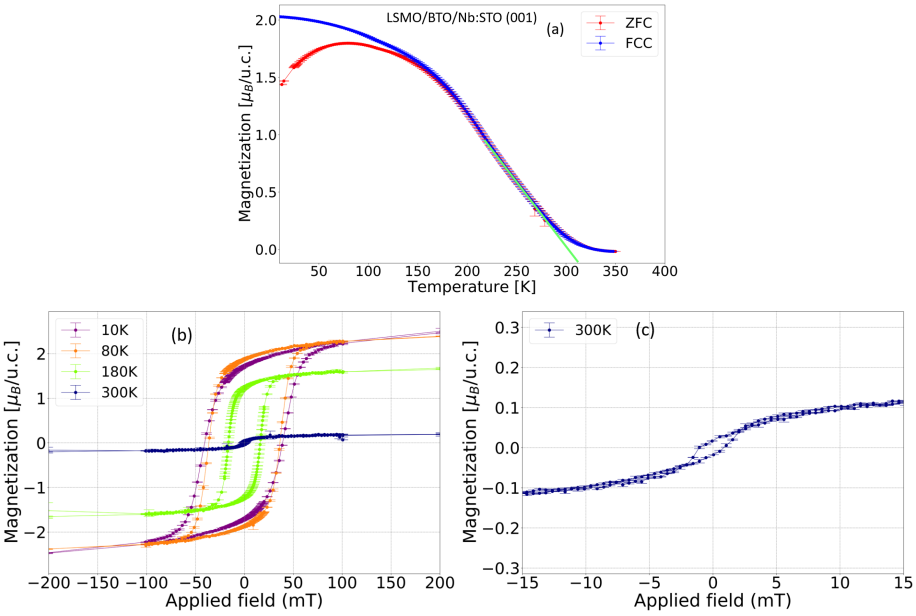

Figure 9.9: (a) M-T curve measured at 50 mT **(b)**M-H curve measured at different temperatures **(c)** zoom-in on 300 K curve for LSMO/BTO/Nb:STO (001) heterostructure.

Magnetization as a function of temperature (fig. 9.9 (a)) was recorded for LSMO/BTO /Nb:STO (001) heterostructure which shows no structural phase transition of BTO. The calculated Curie temperature is $T_C = 308 \pm 2$ K. One observe a reduction in

magnetization at low temperature regime of ZFC curve, which indicates pinning of some magnetic moments in LSMO. Since XRR results show a high roughness at LSMO/BTO interface which could produce defects in the LSMO layer, thereby causing reduction in magnetization of LSMO. The magnetization hysteresis curves (fig. 9.9 (b) and (c)) depict stable ferromagnetic state of LSMO. The sample was checked for presence of exchange bias but no exchange bias was observed.

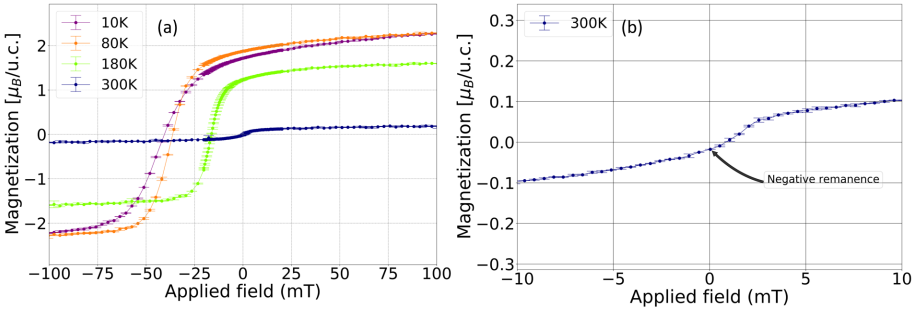

Figure 9.10: (a) Half-cycle of M-H curve plotted where magnetic field goes from +2.5 T to -2.5 T **(b)**Presence of negative remanence observed for 300 K measurement.

Owing to the results obtained in previous LSMO/PMN-PT(001) samples, this sample was also checked for presence of any negative remanence effect. The results are shown in fig.9.10. One observes NRM for 300 K curve and not for the rest low temperature curves. This behavior is consistent with the results obtained for LSMO/PMN-PT(001) samples. The presence of NRM can arise due to the presence of defects/oxygen vacancies as mentioned in the previous LSMO/PMN-PT(001) samples. However, after observing the presence of NRM in LSMO/BTO/Nb:STO (001) sample, a question arises if this NRM effect is some kind of intrinsic property of LSMO film. To confirm this, one must grow LSMO film on different substrates and check the nature of hysteresis loop at different temperatures.

9.5 Conclusion

Using HOPSS system it was possible to calibrate the growth parameters for BTO film and was able to achieve good quality BTO thin film. Ferroelectric properties of BTO films were examined using PFM, where one could observe the retention nature of the ferroelectric domains in BTO. To ensure the ferroelectric properties of whole BTO layer, a polarization hysteresis (P-E) and leakage current measurements are required. One was able to grow LSMO/BTO/Nb:STO (001) heterostructure using HOPSS and OMBE. It is possible to grow both layers in HOPSS. The magnetic properties of this heterostructure confirmed stable structure of BTO with no structural phase transitions and LSMO showed stable ferromagnetic state. The interface roughness between LSMO/BTO is probably due to transfer of sample from one system to another. This interface roughness results in the pinning of some magnetic

moments in LSMO which can be seen from ZFC curve. This heterostructure also shows presence of NRM effect for 300 K M-H curve. This behaviour is similar to the results obtained for LSMO/PMN-PT(001) heterostructure.

10 Summary and Conclusion

LSMO layers were successfully grown on PMN-PT(001) substrate. Structural properties reveal single crystalline and epitaxial growth of LSMO layers with a thickness of 110 Å, 300 Å and 500 Å. The ME measurements demonstrate presence of strain and charge-mediated coupling. The impact of strain-mediated coupling is found to be dominant along the hard axis [100] of LSMO whereas charge-mediated coupling becomes prominent along the easy axis [110] of LSMO at 300 K. The voltage is applied along [001] direction for all the ME measurements. The strain-mediated coupling results in butterfly pattern, though the presence of asymmetry of this butterfly loop indicated contribution from another effect. Since PMN-PT is piezoelectric as well as FE system, both strain and switching of FE polarization comes into play. On measuring along easy axis of LSMO in remanence at 300 K, polarization hysteresis like loop was observed demonstrating the dominance of charge-coupling. To decouple the effect from both mechanism, a simple mathematical model was constructed using literature data to qualitatively estimate the strain and charge contributions. This model was then used to fit the ME curve and a reasonable fit was obtained with 72% strain and 28% charge contribution for a 300 K measurement with applied magnetic field of 10 mT. The temperature dependent ME measurements showed change in strain-mediated behavior from butterfly loop at 300 K to linear at 80 K measurements. This change is attributed to the polarization hardening at low temperature, thus, polarization cannot follow the electric field, leading to linear strain-coupling. The magnetic depth profile was probed as a function of voltage by PNR, which revealed presence of interlayer with reduced NSLD and MSLD. Also, the rocking curve broadened up due to surface corrugation which made the PNR fitting a bit difficult. This interlayer was examined by STEM and EDS which showed Mn-excess in the form of particles with triangular cross-sections. The stoichiometry of these particles was confirmed by FCC measurement, where a jump in magnetization was observed near the Curie temperature, $T_C = 43$ K, of Mn_3O_4. The nucleation of Mn_3O_4 becomes easier in LSMO matrix, due its good chemical compatibility when the LSMO grows under large strain. The off-axis electron holography was performed on 500 Å thick LSMO/PMN-PT(001) as a function of temperature which revealed uniform remanent magnetic field in LSMO layer. The magnetic phase gradient reduced as a function of temperature depicting the reduction in magnetization with increasing temperature which is consistent with macroscopic magnetization measurements.

The second system LSMO/BTO/Nb:STO (001) was studied where BTO layer acts as a FE component and Nb:STO is a conductive substrate. The growth of BTO was calibrated using HOPSS and its structural and FE properties were studied using X-rays and PFM, respectively. As-grown BTO films were single crystalline and epitaxial and the PFM measurements confirmed the FE properties of BTO

layer. It was possible to switch the FE polarization in BTO layer with the application of ±5 V in PFM. Then the sample was transferred to OMBE chamber where LSMO layer was deposited on BTO/Nb:STO(001). The complete heterostructure LSMO/BTO/Nb:STO (001), showed good crystalline and magnetic properties. For future, it would be possible to test this structure for ME coupling.

These measurements showcase that it is possible to achieve non-volatile ME coupling in LSMO/PMN-PT(001) heterostructure which is an important aspect for magnetic storage devices. The obtained asymmetric butterfly loops at 300 K with applied magnetic field as well as in remanence shows that the magnetization does not returns to its initial state after the removal of the bias. Thus it is possible to have 2 distinct states with slightly higher or lower magnetization and change between them. However, it is not possible to apply a voltage pulse to such system as used by most of the memory devices. One needs to ramp the voltage slowly across the structure otherwise it can result in deterioration of the system. As it is not possible to switch the direction of magnetization with applied voltage, it is not possible to develop structure where giant magnetoresistance (GMR) or tunneling magnetoresistance (TMR) effect can be realized.

11 Outlook

This thesis investigates the two potential candidates for artificial multiferroic heterostructures where magnetism can be manipulated by application of voltage. Both systems comprise of a ferromagnetic (FM) and a ferroelectric (FE) component. LSMO/PMN-PT(001) heterostructure displays interesting nature of magnetoelectric (ME) coupling which was influenced by different parameters like temperature and direction of the easy and hard axis of the FM. One observed a combination of strain and charge-mediated ME coupling with their strength based on these parameters.

In future studies, it would be interesting to study the temperature dependent Polarization versus Electric field (P-E) behavior of PMN-PT(001) to understand the polarization switching. In addition, one can perform reciprocal space mapping on PMN-PT(001) as a function of temperature and voltage to see the switching of FE domains. This can help in understanding the change in ME coupling from butterfly loop to linear as a function of temperature. One observes some off-specular scattering in the 2D maps obtained from the PNR measurements at ILL. This off-specular scattering may arise from nuclear or magnetic ordering in LSMO due to switching of FE domains in PMN-PT, which can be investigated by performing GISANS. The system studied in this thesis possesses multi-domain structure of FE domains and the single domain configuration can be achieved by applying voltage to PMN-PT(111) substrate. Also, the easy axis of bulk LSMO lies along [111] and thus, might result in significant changes in magnetization. Growing LSMO on PMN-PT(111) and studying its ME coupling behavior may help to give some clarification on charge-mediated ME coupling as the FE polarization switching in PMN-PT takes place along [111] directions. In the virgin state, the FE domains in PMN-PT are randomly oriented, therefore, for achieving single domain state one should pole the substrate while thermally annealing it above the FE Curie temperature of PMN-PT. By depositing LSMO layer on different orientation of PMN-PT substrates and applying voltage would give a comprehensive picture of strain and FE domain evolution in this system.

The second system LSMO/BTO/Nb:STO(001), where BTO layer is the FE component, should be easier to manipulate with voltage, once this system is tested to confirm no leakage currents exist. Also, surface etching is required for Nb:STO substrate in order to have TiO_2 terminated surface to get uniform conductivity. Since, here a BTO thin film is used, it is possible to achieve ME coupling by applying smaller voltages than for LSMO/PMN-PT. Both systems exhibit a strong approach towards low energy consumption devices where magnetic states can be manipulated with an applied electric field.

During the course of this thesis work an interesting effect of Negative remanence (NRM) was observed in both systems. This raises the question of whether this effect is a result of strain and defects/oxygen vacancies in the system or probably some intrinsic property of LSMO itself. A systematic study is required to understand this effect. It would be interesting to grow LSMO on different substrates which provide tensile and compressive strain to study NRM in detail.

Supplementary material

S.1 PNR at 300K at NCNR, NIST

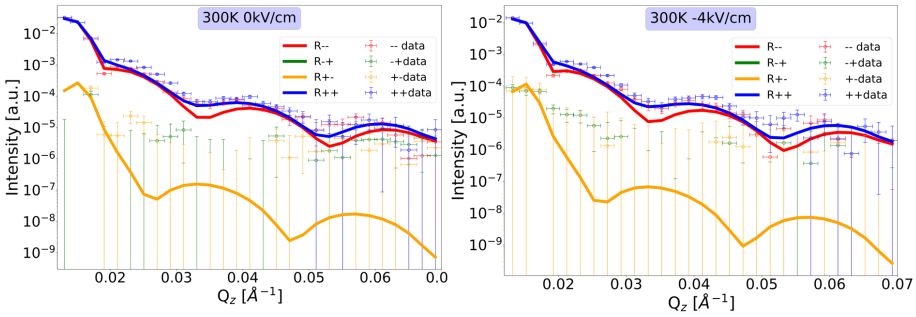

Figure S1: PNR curves recorded at 300,K with applied electric field of 0 kV/cm and -4 kV/cm

Fig. S1 shows the PNR curves measured at 300 K with applied electric field of 0 kV/cm and -4 kV/cm. As can be seen from the above figure, the fitting is not good for these set of curves. The magnetic signal is quite low at 300 K due to which splitting between R++ and R– channels is not at all visible and after application of voltage, other artifacts were induced which made the data fitting difficult.

S.2 Remote beamtime at ILL

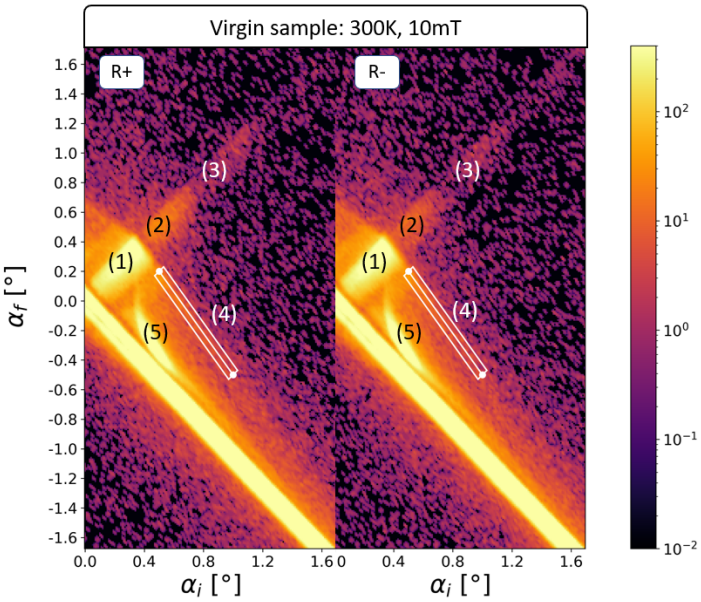

Figure S2: 2D $\alpha_i - \alpha_f$ maps of PNR curves recorded at 300,K with applied magnetic field of 10 mT on a LSMO/PMN-PT(001) sample in its virgin state. The marked (1) is total reflection plateau, (2),(3) are the thickness oscillations, (4) is the off-specular feature and (5) is Yoneda peak.

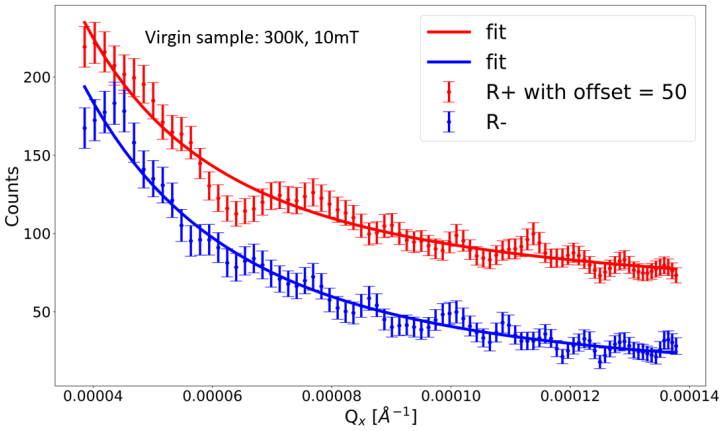

Figure S3: Line profile extracted from the line cut (white box) performed on 2D map of R+ and R- channel at 300 K with applied field of 10 mT as shown in fig. S2. The line profile is fitted using a Lorentzian.

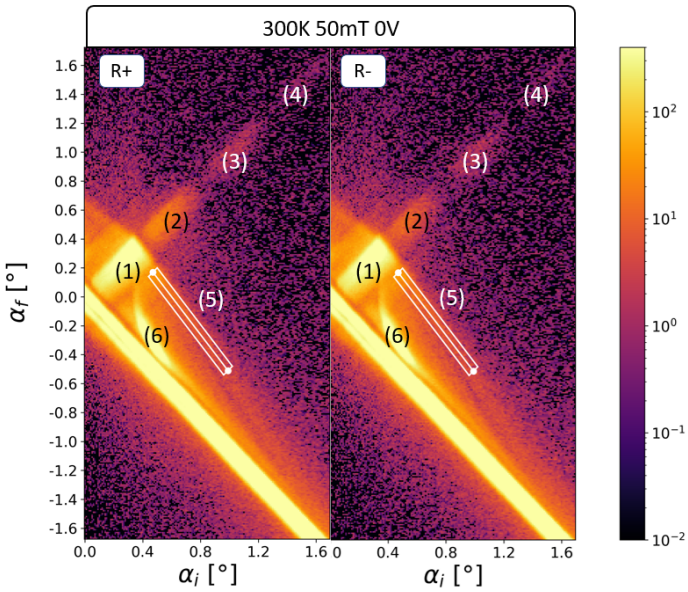

Figure S4: 2D $\alpha_i - \alpha_f$ maps of PNR curves recorded at 300,K with applied magnetic field of 50 mT on a LSMO/PMN-PT(001) sample in its virgin state. The marked (1) is total reflection plateau, (2),(3), (4) are the thickness oscillations,(5) is the off-specular feature and (6) is Yoneda peak .

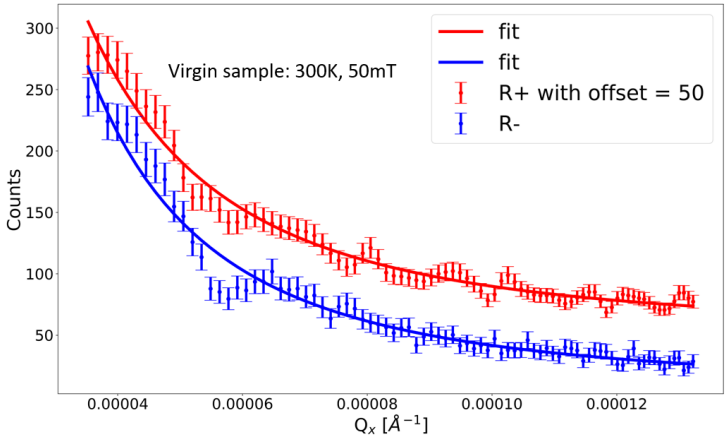

Figure S5: Line profile extracted from the line cut (white box) performed on 2D map of R+ and R- channel at 300 K with applied field of 50 mT as shown in fig. S4. The line profile is fitted using a Lorentzian.

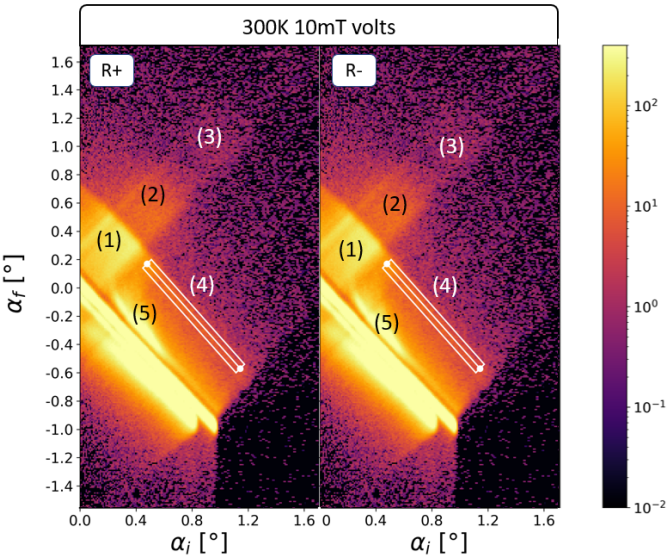

Figure S6: 2D $\alpha_i - \alpha_f$ maps of PNR curves recorded at 300,K with applied magnetic field of 10 mT on a LSMO/PMN-PT(001) sample after its exposure and removal of voltage. The marked (1) is total reflection plateau, (2),(3) are the thickness oscillations,(4) is the off-specular feature and (5)is Yoneda peak.

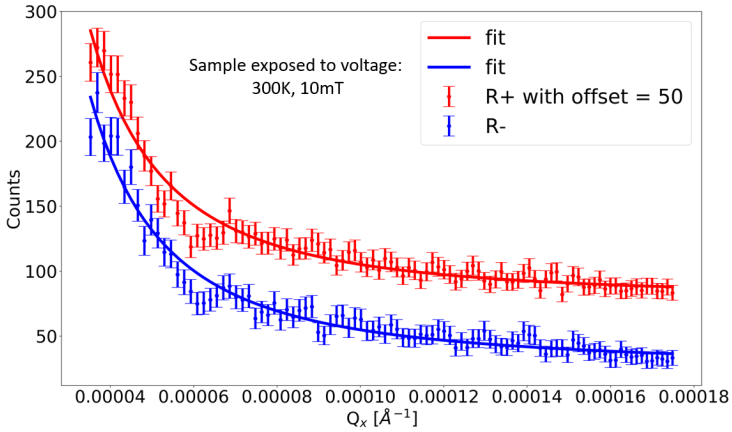

Figure S7: Line profile extracted from the line cut (white box) performed on 2D map of R+ and R- channel at 300 K with applied field of 10 mT after exposure to voltage as shown in fig. S6. The line profile is fitted using a Lorentzian.

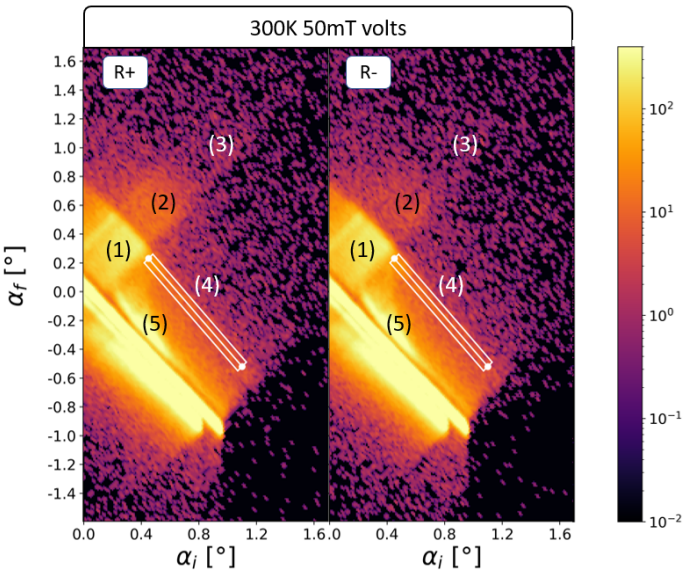

Figure S8: 2D $\alpha_i - \alpha_f$ maps of PNR curves recorded at 300,K with applied magnetic field of 50 mT on a LSMO/PMN-PT(001) sample after its exposure and removal of voltage. The marked (1) is total reflection plateau, (2),(3) are the thickness oscillations,(4) is the off-specular feature and (5)is Yoneda peak.

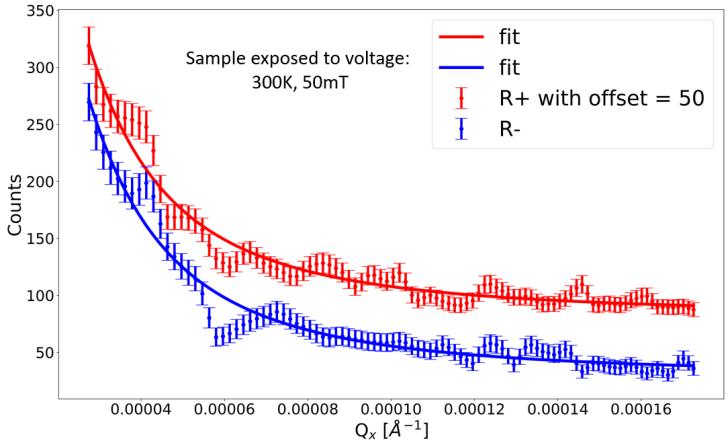

Figure S9: Line profile extracted from the line cut (white box) performed on 2D map of R+ and R- channel at 300 K with applied field of 50 mT after exposure to voltage as shown in fig. S6. The line profile is fitted using a Lorentzian.

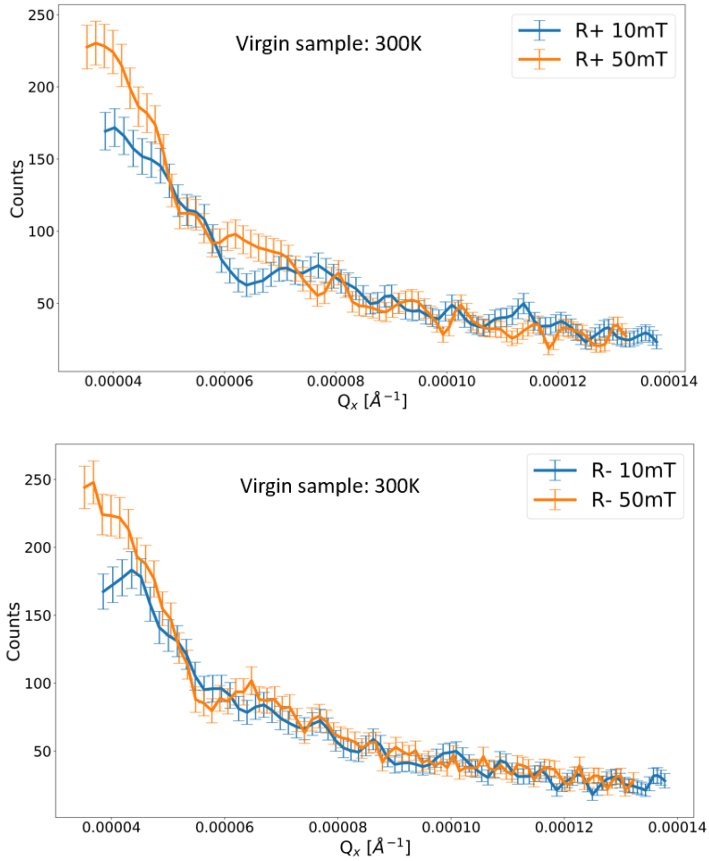

Figure S10: Line profile of R+ and R- channel plotted together for applied magnetic fields of 10 mT and 50 mT for the sample in a virgin state.

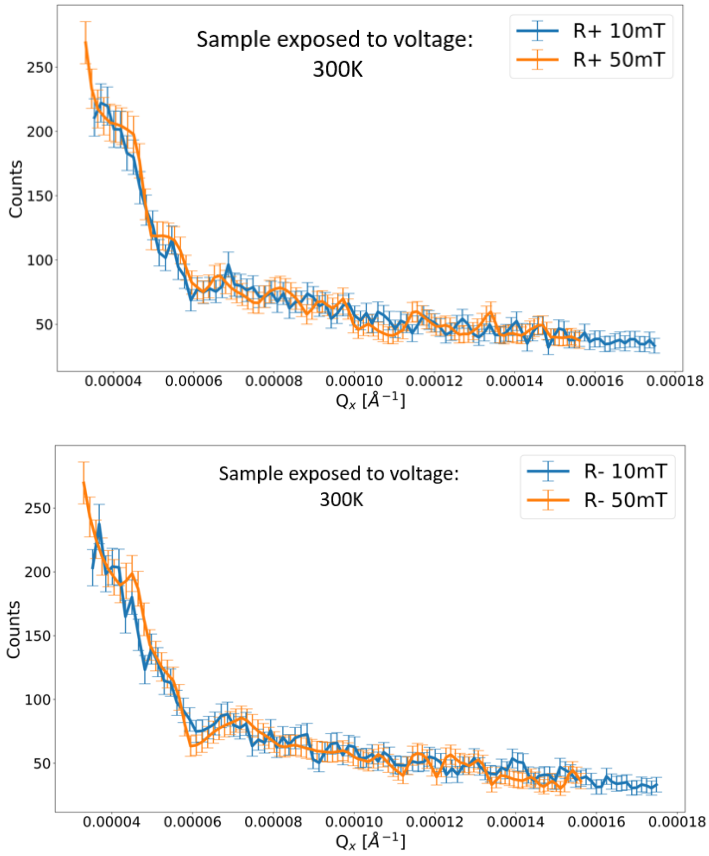

Figure S11: Line profile of R+ and R- channel plotted together for applied magnetic fields of 10 mT and 50 mT for the sample that has been exposed to voltage.

PNR experiments were performed by mail-in experiment at ILL with reflectometer SUPERADAM. Two samples were sent, one in the virgin state and other after applying the voltage. The aim of the experiment was to investigate presence of any off-specular magnetic scattering as a function of voltage but due to time constraint and instrument limitation, it was not possible to perform full polarization analysis over the complete detector area. 2D detector maps of half-polarized PNR curves were recorded at 300 K and 80 K at 10 mT and 50 mT on the two samples. These measurements were performed by Dr. Alexei Vorobiev at ILL. Fig. S2, S4, S6, S8 and S12 show the presence of thickness oscillations along with Yoneda peak and off-specular feature. Line cuts are performed along the off-specular feature of scattering and line profile as shown in the fig. S3, S5, S7 and S9 . A Lorentzian fitting is used to fit these line profiles which gives an average correlation length of $5.7 \pm 1.5\,\mu$m. There is no change observed in correlation lengths for before and after voltage sample.

The line profiles of off-specular scattering R+ and R- at two applied magnetic fields: 10 mT and 50 mT are plotted together. For the virgin sample the intensity is higher at 50 mT. For the sample on which a voltage has been applied, one observes no difference.

It is not possible to determine the origin of this off-specular scattering, i.e. whether it originates from interfacial roughness or from bulk nuclear or magnetic scattering length density fluctuations, as the measurements were not performed with polarization analysis. Fig. S6 and S8 depict broadening of total reflection plateau and the thickness oscillations after the sample was exposed to voltage. These results are consistent with PNR experiments performed at NIST. These results make a good basis to perform GISANS on LSMO/PMN-PT(001) samples to investigate these off-specular features.

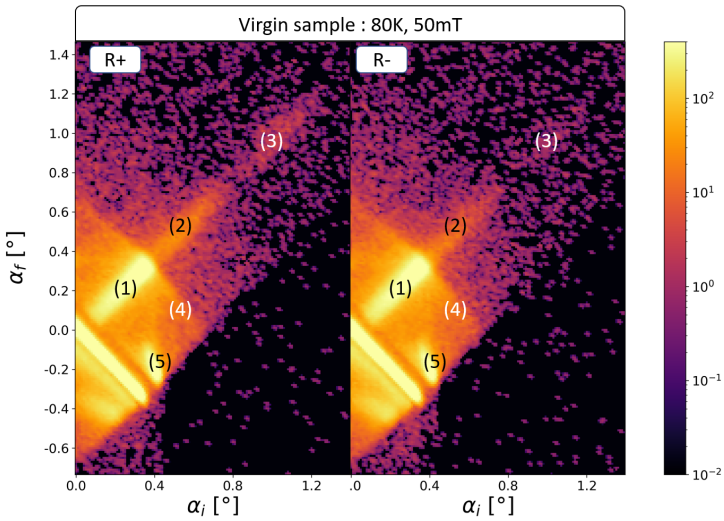

Figure S12: 2D $\alpha_i - \alpha_f$ maps of PNR curves recorded at 80,K with applied magnetic field of 50 mT on a LSMO/PMN-PT(001) sample in its virgin state. The marked (1) is total reflection plateau, (2),(3) are the thickness oscillations,(4) is the off-specular feature and (5)is Yoneda peak.

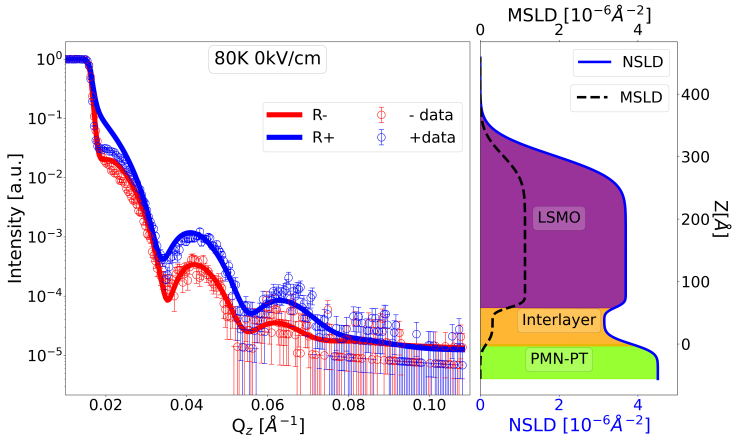

Figure S13: PNR fit for relfectivity measured at 80 K with applied magnetic field of 50 mT at 0 V. The parameters used here for fitting are taken from PNR fitting performed for NIST measurements.

Parameter	Value [Å]
LSMO thickness	$242.9^{+9.2}_{-5.2}$
LSMO σ	$31.6^{+6.6}_{-3.8}$
LSMO magnetization	$2.5^{+0.3}_{-5E-3}$
Substrate σ	$10.7^{+8.8}_{-0.7}$
Interlayer thickness	$59.5^{+2.7}_{-12.2}$
Interlayer σ	$6.6^{+6.3}_{-3.5}$
Interlayer magnetization	$0.8^{+0.4}_{-0.2}$

Table S1: Parameters used for fitting PNR curve shown in fig. S13

.

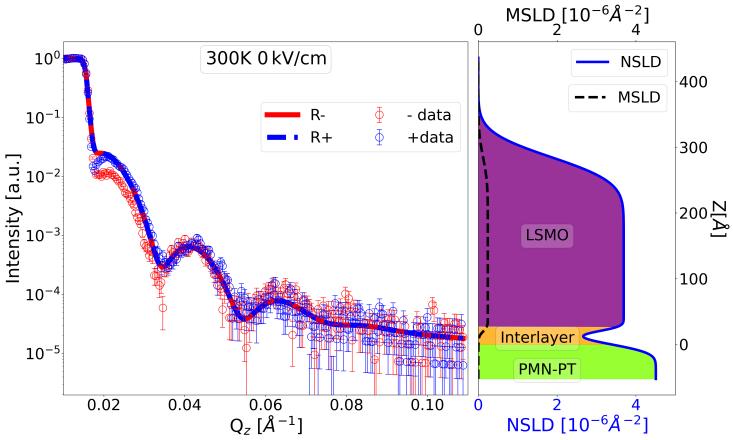

Figure S14: PNR fit for relfectivity measured at 300 K with applied magnetic field of 10 mT at 0 V. The parameters used here for fitting are taken from PNR fitting performed for NIST measurements.

Parameter	Value [Å]
LSMO thickness	$265.2^{+2.5}_{-1.4}$
LSMO σ	$30.2^{+2.5}_{-2.9}$
LSMO magnetization	$0.5^{+0.2}_{-0.01}$
Substrate σ	$10.5^{+1}_{-0.7}$
Interlayer thickness	$20.6^{+1.7}_{-0.5}$
Interlayer σ	$5.9^{+5.1}_{-1.3}$
Interlayer magnetization	$0.03^{+0.2}_{-0.1}$

Table S2: Parameters used for fitting PNR curve shown in fig. S14

.

The fitting model used for PNR curves shown in fig. S13 and S14 is similar to the model used to fit the PNR curves recorded at NIST. The simulation fits reasonably well for higher Q-range but not for the lower Q-range. There should be splitting present near $Q_z = 0.02\,Å^{-1}$ according to simulation and physical parameters of the LSMO/PMN-PT. The difference between experimental data and simulation is unknown. Probably its coming from some faceting on substrate along the direction of neutron beam scattering. Different models were tried to fit these PNR curves but this was the best fit achieved.

S.3 LSMO growth with OMBE

Growth rates

Element	Temperature [°C]	Frequency change [Hz/s]
La	1501	-0.11
Sr	484	-0.038
Mn	791.2	-0.091

Table S3: Growth rates used for LSMO deposition on PMN-PT(001).

Growth procedure

$$
\begin{aligned}
Plasma &= 350\,W/0.15\,sccm \\
Total\,pressure &= 5.8 \times 10^{-6}\,mbar \\
Growth\,duration &= 6450\,s \\
Substrate\,annealing &= 730\,°C\;for\;5400\,s \\
Growth\,temperature &= 730\,°C \\
Post\,annealing &= 200\,°C\;for\;1800\,s \\
Cooling &= to\,room\,temperature\,with\,2\,K/min
\end{aligned}
$$

S.4 Parameters for XRR simulations for LSMO/PMN-PT(001)

Parameter	Value [Å]
LSMO thickness	$295.2^{+4.4}_{-3.6}$
LSMO σ	$11.3^{+2.2}_{-1.6}$
Top layer thickness	$27.9^{+2.6}_{-2.7}$
Top layer σ	$11.3^{+2.2}_{-1.6}$
Substrate σ	$10.7^{+1.5}_{-1.5}$

Table S4: Parameters used for fitting XRR curve shown in fig. 6.4c.

Parameter	Value [Å]
LSMO thickness	$111.1^{+0.7}_{-0.7}$
LSMO σ	$2.5^{+0.3}_{-0.2}$
Substrate σ	$6.2^{+0.5}_{-0.5}$

Table S5: Parameters used for fitting XRR curve shown in fig. 7.2b.

S.5 Parameters for XRR simulations for BTO/STO(001)

Parameter	Value [Å]
BTO thickness	$95.6^{+4.2}_{-2.4}$
BTO σ	$7.4^{+0.2}_{-0.2}$

Table S6: Parameters used for fitting XRR curve shown in fig. 9.2c.

Parameter	Value [Å]
BTO thickness	$286.7^{+6.2}_{-0.7}$
BTO σ	$1.2^{+4.9}_{-4E-14}$
Top layer thickness	$17.3^{+0.4}_{-3.3}$
Top layer σ	$4.71^{+0.3}_{-3.1}$

Table S7: Parameters used for fitting XRR curve shown in fig. 9.3c.

S.6 Parameters for XRR simulations for LSMO/BTO/Nb:STO(001)

Parameter	Value [Å]
BTO thickness	$220.3^{+8.2}_{-10.9}$
BTO σ	$21.3^{+11.3}_{-0.8}$
LSMO thickness	$284.1^{+12.7}_{-9.2}$
LSMO σ	$12.4^{+4.6}_{-0.7}$
Top layer thickness	$18.5^{+1.3}_{-1.9}$
Top layer σ	$10^{+0.3}_{-0.1}$

Table S8: Parameters used for fitting XRR curve shown in fig. 9.7b.

Acknowledgements

I would like to convey my thanks to lots of people who supported me and made my PhD experience interesting and fun-filled.

Prof. Dr. Thomas Brückel for giving me this opportunity to work at JCNS, for his guidance and support, for fruitful discussions and for reviewing my thesis. I want to really thank him for supporting me to travel to different conferences and to USA to carry out my beamtime experiments.

Prof. Rafal E. Dunin-Borkowski for giving me the opportunity to work with different transmission electron microscopes and learn about different techniques at ER-C and for the second review of this thesis.

I would like to thank **both my professors** for trusting me and giving me this opportunity to be a bridge student between the 2 institutes: JCNS and ER-C. It was a great opportunity for me to meet a lot of interesting people and learn different things from them.

Dr. Emmanuel Kentzinger for his great guidance and support throughout my thesis work and for a many fruitful discussions. I really appreciate his openness to new ideas. Working with him during beamtimes was always fun and I learned a lot about neutron scattering from him. He is a very friendly and warm person which made it easier me for to discuss things without any hesitation and talk freely.

Dr. Andras Kovács for helping and guiding me with electron microscopy experiments. With many fruitful discussions with him, I was able to learn a lot about advanced electron microscopy methods. He helped me a lot in the analysis of electron holography results. Without his support and encouragement, it would have been difficult to learn and understand the advanced electron microscopy techniques.

Dr. Anirban Sarkar for training me in growth of thin films using OMBE and for many fruitful discussions. It was always fun performing experiments with him.

Patrick Schöffmann for being there with me at professional as well as personal front. I always enjoyed us working as a team and trying to find out a solution of a problem. His support and encouragement pushed to work harder towards the problems. I want to thank him for helping and training me with thin film growth on OMBE and for cheering me up when I was in stress.

Dr. Qianqian Lan for helping me with electron holography experiments at ER-C.

Dr. Lei Jin for training me to use TEM, helping with STEM experiments and for fruitful discussions.

Prof. Dr. Michael Faley for helping with BTO growth in HOPSS.

Dr. Oleg Petracic for fruitful discussions about magnetoelectric coupling and MPMS.

Frank Gossen and **Berthold Schmitz** for technical assistance in all ways.

Lidia Kibkalo for preparation of FIB samples.

Dr. Randolf Beerwerth for analysis and simulation of the reflectometry measurements at GALAXI.

Dr. Brian Kirby and **Dr. Alexander Grutter** for help and assistance during beamtime at NCNR, NIST and for fruitful discussions.

Dr. Alexei Vorobiev for performing remote PNR experiments at ILL, Grenoble, France.

Dr. Markus Waschk for helping with thin film growth at OMBE and for fruitful discussions.

Dr. Jürgen Schubert for performing RBS measurement and analysis.

Dr. Gregor Mussler and **Dr Alexander Shkurmanov** for performing RSM measurements and analyis.

Dr. Margret Giesen for allowing me to use AFM/PFM from PGI-6.

Barbara Daegener for her friendly and warm welcome to the institute and lots of administrative help.

Dr. Ulrich Rücker for help with XRR and GALAXI.

Annika Stellhorn for being a great friend and for cooking and baking with me.

Mohammed Ait Haddouch, **Nileena Nandakumaran**, **Mathias Strothmann** and **Dr.Asmaa Qdemat** for all the fun and enjoyment during my thesis work.

My family for their support, encouragement and patience. At last I would like to thank all other colleagues at JCNS and ER-C for great support and help. Also, For all the cake we had at ER-C group meetings, for fun-filled PhD days at JCNS and conferences.

List of publications

- **T. Bhatnagar-Schöffmann**, E. Kentzinger, A. Sarkar, P. Schöffmann, L. Jin, Q. Lan, A. Kovács, B. Kirby, A. Grutter, R. Beerwerth, M. Waschk, A. Stellhorn, U. Rücker, R.E. Dunin-Borkowski, Th. Brückel. Differentiation between strain and charge mediated magnetoelectric coupling in $La_{0.7}Sr_{0.3}MnO_3/Pb(Mg_{1/3}Nb_{2/3})_{0.7}Ti_{0.3}O_3(001)$. *New Journal of Physics, IOP Publishing,* ***2021****, 23, 063043.*

- P. Schöffmann, A. Sarkar, M. Hussein Hammed, **T. Bhatnagar-Schöffmann**, S. Pütter, B. Kirby, A. Grutter, E. Kentzinger, A. Stellhorn, J. Barthel, A. Gloskovski, M. Müller, Th. Brückel. Investigation of strain and charge contributions to the magnetoelectric coupling in Fe_3O_4/PMN-PT(001) and Fe_3O_4/PMN-PT(011) artificial multiferroic heterostructures. *in preparation* (2021).

- N. Nandakumaran, L. Barnsley, A. Feoktystov, S. A. Ivanov, D. L. Huber, L. S. Fruhner, V. Leffler, S. Ehlert, E. Kentzinger, **T. Bhatnagar-Schöffmann**, U. Rücker, M. T. Wharmby, A. Cervellino, R. E. Dunin-Borkowski, Th. Brückel, M. Feygenson. Unravelling Magnetic Nanochain Formation in Dispersion for In-Vivo Applications. *Advanced Materials,* ***2021****, 2008683.*

- T. Köhler, A. Feoktystov, O. Petracic, E. Kentzinger, **T. Bhatnagar-Schöffmann**, M. Feygenson, N. Nandakumaran, J. Landers, H. Wende, A. Cervellino, U. Rücker, A. Kovacs, R. E. Dunin-Borkowski, Th. Brückel. *Nanoscale, The Royal Society of Chemistry,* ***2021****, 13, 6965-6976.*

Bibliography

[1] J. Daughton, "Magnetoresistive random access memory (mram)," 2000.

[2] T. Banerjee, *Oxide Spintronics*. Jenny Stanford Publishing, 2019.

[3] E. Y. Tsymbal, E. R. A. Dagotto, C.-B. Eom, and R. Ramesh, *Multifunctional Oxide Heterostructures*. Oxford Scholarship, 2012.

[4] I. E. Dzyaloshinskii, "On the magneto-electrical effects in antiferromagnets," *Sov. Phys. JETP*, no. 10, p. 628, 1960.

[5] T. Kimura, T. Goto, H. Shintani, K. Ishizaka, T. Arima, and Y. Tokura, "Magnetic control of ferroelectric polarization," *Nature*, vol. 426, no. 6962, pp. 55–58, 2003.

[6] C. A. F. Vaz, J. Hoffman, C. H. Ahn, and R. Ramesh, "Magnetoelectric coupling effects in multiferroic complex oxide composite structures," *Advanced Materials*, vol. 22, no. 26-27, pp. 2900–2918, 2010.

[7] H. Y. Hwang, Y. Iwasa, M. Kawasaki, B. Keimer, N. Nagaosa, and Y. Tokura, "Emergent phenomena at oxide interfaces," *Nature Materials*, vol. 11, no. 2, pp. 103–113, 2012.

[8] A. Bhattacharya and S. J. May, "Magnetic oxide heterostructures," *Annual Review of Materials Research*, vol. 44, no. 1, pp. 65–90, 2014.

[9] C. Song, B. Cui, F. Li, X. Zhou, and F. Pan, "Recent progress in voltage control of magnetism: Materials, mechanisms, and performance," *Progress in Materials Science*, vol. 87, pp. 33 – 82, 2017.

[10] H. Bluhm, T. Brückel, M. Morgenstern, G. von Plessen, and C. Stampfer, *Electrons in Solids*. De Gruyter, 2019.

[11] J. G. Bednorz and K. A. Müller, "Possible high t_c superconductivity in the ba-la-cu-o system," *Z. Physik B - Condensed Matter*, no. 64, pp. 189–193, 1986.

[12] A.-M. Haghiri-Gosnet and J.-P. Renard, "CMR manganites: physics, thin films and devices," *Journal of Physics D: Applied Physics*, vol. 36, pp. R127–R150, apr 2003.

[13] M.-H. Phan and S.-C. Yu, "Review of the magnetocaloric effect in manganite

materials," *Journal of Magnetism and Magnetic Materials*, vol. 308, no. 2, pp. 325 – 340, 2007.

[14] M. Fiebig, "Revival of the magnetoelectric effect," *Journal of Physics D: Applied Physics*, vol. 38, pp. R123–R152, apr 2005.

[15] E. Vervew, "Electronic conduction of magnetite (Fe_3O_4) and its transition point at low temperatures.," *Nature*, no. 144, pp. 327–328, 1939.

[16] G. D. Barrera, J. A. O. Bruno, T. H. K. Barron, and N. L. Allan, "Negative thermal expansion," *Journal of Physics: Condensed Matter*, vol. 17, pp. R217–R252, jan 2005.

[17] M. Imada, A. Fujimori, and Y. Tokura, "Metal-insulator transitions," *Rev. Mod. Phys.*, vol. 70, pp. 1039–1263, Oct 1998.

[18] K. Momma and F. Izumi, " VESTA3 for three-dimensional visualization of crystal, volumetric and morphology data," *Journal of Applied Crystallography*, vol. 44, pp. 1272–1276, Dec 2011.

[19] S. Blundell, *Magnetism in Condensed Matter*. Oxford Master Series in Physics, Oct. 2001.

[20] K. Rabe, C. H. Ahn, and J.-M. Triscone, *Physics of Ferroelectrics*. Springer Berlin Heidelberg, July 2017.

[21] R. Whatmore, *Ferroelectric Materials*, pp. 1–1. Cham: Springer International Publishing, 2017.

[22] R. Cohen, "Origin of ferroelectricity in perovskite oxides," *Nature*, vol. 358, pp. 136–138, Mar. 1992.

[23] W. Cochran, "Crystal stability and the theory of ferroelectricity," *Advances in Physics*, vol. 9, no. 36, pp. 387–423, 1960.

[24] P. W. Anderson *Fizika Dielektrikov (Ed: G. I. Skanavi), Acad. Nauk, SSSR, Moscow*, 1960.

[25] L. B. Kong, H. Huang, and S. Li, "Fundamentals of ferroelectric materials," *Wiley-VCH Verlag GmbH & Co. KGaA*, 2018.

[26] D. J. Franzbach, *Field Induced Phase Transitions in Ferroelectric Materials*. PhD thesis, TU Darmstadt, 2014.

[27] Y. Shen, J. Cai, H.-C. Ding, X.-W. Shen, Y.-W. Fang, W.-Y. Tong, X.-G. Wan, Q. Zhao, and C.-G. Duan, "Role of lone-pairs in driving ferroelectricity of perovskite oxides: An orbital selective external potential study," *Advanced Theory and Simulations*, vol. 2, no. 6, p. 1900029, 2019.

[28] E. Nakamura, M. Adachi, Y. Akishige, K. Deguchi, J. Harada, T. Ikeda,

M. Okuyama, E. Sawaguchi, Y. Shiozaki, K. Toyoda, T. Yamada, K. Gesi, T. Hikita, Y. Makita, T. Shigenari, I. Tatsuzaki, and T. Yagi, *Oxides ,Landolt-Börnstein: Numerical Data and Functional Relationships in Science and Technology*, vol. 16. Springer, Berlin, 1981.

[29] A. Mayeen and N. Kalarikkal, "2 - development of ceramic-controlled piezoelectric devices for biomedical applications," in *Fundamental Biomaterials: Ceramics* (S. Thomas, P. Balakrishnan, and M. Sreekala, eds.), Woodhead Publishing Series in Biomaterials, pp. 47 – 62, Woodhead Publishing, 2018.

[30] K. Uchino, "3 - relaxor ferroelectric-based ceramics," in *Advanced Piezoelectric Materials* (K. Uchino, ed.), Woodhead Publishing Series in Electronic and Optical Materials, pp. 111 – 129, Woodhead Publishing, 2010.

[31] M. A. Helal, M. Aftabuzzaman, S. Tsukada, and S. Kojima, "Role of polar nanoregions with weak random fields in pb-based perovskite ferroelectrics," *Scientific Reports*, vol. 7, no. 1, p. 44448, 2017.

[32] V. Bokov and I. Mylnikova, "Electrical and optical properties of single crystals of ferroelectrics with a diffused phase transition," *SOVIET PHYSICS-SOLID STATE*, vol. 3, pp. 613–623, 1961.

[33] M. Eremenko, V. Krayzman, A. Bosak, H. Y. Playford, K. W. Chapman, J. C. Woicik, B. Ravel, and I. Levin, "Local atomic order and hierarchical polar nanoregions in a classical relaxor ferroelectric," *Nature Communications*, vol. 10, no. 1, p. 2728, 2019.

[34] J. C. Ho, K. S. Liu, and I. N. Lin, "Study of ferroelectricity in the pmn-pt system near the morphotropic phase boundary," *Journal of Materials Science*, vol. 28, pp. 4497–4502, 1993.

[35] Z.-G. Ye, Y. Bing, J. Gao, A. A. Bokov, P. Stephens, B. Noheda, and G. Shirane, "Development of ferroelectric order in relaxor (1-x)$Pb(Mg_{1/3}Nb_{2/3})O_3$–x$PbTiO_3$ ($0 \leq x \leq 0.15$)," *Phys. Rev. B*, vol. 67, p. 104104, Mar 2003.

[36] S. W. Choi, R. T. R. Shrout, S. J. Jang, and A. S. Bhalla, "Dielectric and pyroelectric properties in the $Pb(Mg_{1/3}Nb_{2/3})O_3$-$PbTiO_3$ system," *Ferroelectrics*, vol. 100, no. 1, pp. 29–38, 1989.

[37] B. Noheda, D. E. Cox, G. Shirane, J. Gao, and Z.-G. Ye, "Phase diagram of the ferroelectric relaxor (1-x)$PbMg_{1/3}Nb_{2/3}O_3$-x$PbTiO_3$," *Phys. Rev. B*, vol. 66, p. 054104, Aug 2002.

[38] S. Kim, S. Noda, T. Abe, Y. Yokoi, Y. Nakahira, C. Moriyoshi, and Y. Kuroiwa, "Electric-field-induced structural changes for cubic system of lead-free and lead-based perovskite-type oxides," *Japanese Journal of Applied Physics*, vol. 59, p. SPPA05, jul 2020.

[39] R. von Helmolt, J. Wecker, B. Holzapfel, L. Schultz, and K. Samwer, "Giant negative magnetoresistance in perovskite like $La_{2/3}Ba_{1/3}MnO_x$ ferromagnetic films," *Phys. Rev. Lett.*, vol. 71, pp. 2331–2333, Oct 1993.

[40] A. Weiss, "John b. goodenough: Magnetism and the chemical bond. interscience publishers. new york, london 1963. 393 seiten, 89 abbildungen. preis: Dm 95 s.," *Berichte der Bunsengesellschaft für physikalische Chemie*, vol. 68, no. 10, pp. 996–996, 1964.

[41] J. Velev, J. D. Burton, M. Zhuravlev, and E. Tsymbal, "Predictive modelling of ferroelectric tunnel junctions," *npj Computational Materials*, vol. 2, p. 16009, 05 2016.

[42] D. N. Astrov, "The magnetoelectric effect in antiferromagnets," *Sov. Phys. JETP*, no. 11, pp. 708–709, 1960.

[43] D. N. Astrov, "Magnetoelectric effect in chromium oxide," *Sov. Phys. JETP*, no. 13, pp. 729–733, 1961.

[44] T. Moriya, "Anisotropic superexchange interaction and weak ferromagnetism," *Phys. Rev.*, vol. 120, pp. 91–98, Oct 1960.

[45] S. Fusil, V. Garcia, A. Barthélémy, and M. Bibes, "Magnetoelectric devices for spintronics," *Annual Review of Materials Research*, vol. 44, no. 1, pp. 91–116, 2014.

[46] C. Thiele, K. Dörr, O. Bilani, J. Rödel, and L. Schultz1, "Influence of strain on the magnetization and magnetoelectric effect in La0.7A0.3MnO3/PMN-PT(001) (a=sr, ca)," *PHYSICAL REVIEW B 75, 054408 2007*, 2007.

[47] Z. Feng, D. Lin, H. Luo, S. Li, and D. Fang, "Effect of uniaxial stress on the electromechanical response of <001>-oriented $Pb(Mg_{1/3}Nb_{2/3})O_3$-$PbTiO_3$ crystals," *Journal of Applied Physics*, vol. 97, no. 2, p. 024103, 2005.

[48] M. Buzzi, *Spin Dynamics in Ferroic Materials*. PhD thesis, Philosophisch-Naturwissenschaftlichen Fakultät der Universität Basel, 2015.

[49] H. J. A. Molegraaf, J. Hoffman, C. A. F. Vaz, S. Gariglio, D. van der Marel, C. H. Ahn, and J.-M. Triscone, "Magnetoelectric effects in complex oxides with competing ground states," *Advanced Materials*, vol. 21, no. 34, pp. 3470–3474, 2009.

[50] S. Zhang, Y. G. Zhao, P. S. Li, J. J. Yang, S. Rizwan, J. X. Zhang, J. Seidel, T. L. Qu, Y. J. Yang, Z. L. Luo, Q. He, T. Zou, Q. P. Chen, J. W. Wang, L. F. Yang, Y. Sun, Y. Z. Wu, X. Xiao, X. F. Jin, J. Huang, C. Gao, X. F. Han, and R. Ramesh, "Electric-field control of nonvolatile magnetization in $Co_{40}Fe_{40}B_{20}/Pb(Mg_{1/3}Nb_{2/3})_{0.7}Ti_{0.3}O_3$ structure at room temperature," *Phys. Rev. Lett.*, vol. 108, p. 137203, Mar 2012.

[51] C. A. F. Vaz, J. Hoffman, Y. Segal, J. W. Reiner, R. D. Grober, Z. Zhang, C. H. Ahn, and F. J. Walker, "Origin of the magnetoelectric coupling effect in $PbZr_{0.2}Ti_{0.8})O_3/La_{0.8}Sr_{0.2}MnO_3$ multiferroic heterostructures," *Phys. Rev. Lett.*, vol. 104, p. 127202, Mar 2010.

[52] L. Gerhard, T. K. Yamada, T. Balashov, A. F. Takács, R. J. H. Wesselink, M. Däne, M. Fechner, S. Ostanin, A. Ernst, I. Mertig, and W. Wulfhekel, "Magnetoelectric coupling at metal surfaces," *Nature Nanotechnology*, vol. 5, no. 11, pp. 792–797, 2010.

[53] M. K. Niranjan, C.-G. Duan, S. S. Jaswal, and E. Y. Tsymbal, "Electric field effect on magnetization at the Fe/MgO(001) interface," *Applied Physics Letters*, vol. 96, no. 22, p. 222504, 2010.

[54] T. Maruyama, Y. Shiota, T. Nozaki, K. Ohta, N. Toda, M. Mizuguchi, A. A. Tulapurkar, T. Shinjo, M. Shiraishi, S. Mizukami, Y. Ando, and Y. Suzuki, "Large voltage-induced magnetic anisotropy change in a few atomic layers of iron," *Nature Nanotechnology*, vol. 4, no. 3, pp. 158–161, 2009.

[55] D. S. Sivia, *Elementary Scattering Theory*. Oxford Scholarship, 2011.

[56] C. Cohen-Tannoudji, B. Diu, and F. Laloe, *Quantum Mechanics, Volume 2: Angular momentum, Spin and Approximation methods*. Wiley-VCH, 2019.

[57] T. Brückel, S. Förster, G. Roth, and R. Zorn, *Neutron Scattering Lectures*, vol. 147. Forschungszentrum Jülich GmbH, 2017.

[58] C. E. Bonet, *Size induced electronic and magnetic changes in nanometric rare earth alloys.* PhD thesis, Universidad de Cantabria, Mar. 2014.

[59] C. Kittel, *Introduction to solid state physics, eighth edition*. John Wiley and Sons, 2005.

[60] D. B. Williams and C. B. Carter, *Transmission Electron Microscopy*. Springer Nature.

[61] M. A. Asadabad and M. J. Eskandari, "Electron diffraction," in *Modern Electron Microscopy in Physical and Life Sciences* (M. Janecek and R. Kral, eds.), ch. 1, Rijeka: IntechOpen, 2016.

[62] R. E. Dunin-Borkowski, A. Kovács, T. Kasama, M. R. McCartney, and D. J. Smith, *Handbook of Microscopy*, ch. Electron Holography. Springer, 2019.

[63] A. Kovács and R. E. Dunin-Borkowski, "Chapter 2 - magnetic imaging of nanostructures using off-axis electron holography," vol. 27 of *Handbook of Magnetic Materials*, pp. 59 – 153, Elsevier, 2018.

[64] H. Lichte and M. Lehmann, "Electron holography—basics and applications," *Reports on Progress in Physics*, vol. 71, p. 016102, dec 2007.

[65] R. Dunin-Borkowski, M. McCartney, D. J. Smith, and S. Parkin, "Towards quantitative electron holography of magnetic thin films using in situ magnetization reversal," *Ultramicroscopy*, vol. 74, no. 1, pp. 61 – 73, 1998.

[66] M. Waschk, *Interface phenomena in $La_{1/3}Sr_{2/3}FeO_3$ / $La_{2/3}Sr_{1/3}MnO_3$ heterostructures and a quest for p-electron magnetism*. PhD thesis, RWTH Aachen, 2017.

[67] W. S. Knodle and R. Chow, "10 - molecular beam epitaxy: Equipment and practice," in *Handbook of Thin Film Deposition Processes and Techniques (Second Edition)* (K. Seshan, ed.), pp. 381 – 461, Norwich, NY: William Andrew Publishing, second edition ed., 2001.

[68] J. R. Arthur, "Molecular beam epitaxy," *Surface Science*, vol. 500, pp. 189–217, Mar. 2002.

[69] Y. Horio, *Low-Energy Electron Diffraction*, pp. 349–353. Singapore: Springer Singapore, 2018.

[70] M. Schmitz, *Strain and electric field mediated manipulation of magnetism in $La_{(1-x)}Sr_xMnO_3/BaTiO_3$ heterostructures*. PhD thesis, RWTH Aachen, 2015.

[71] Jülich Centre for Neutron Science, "GALAXI: Gallium anode low-angle x-ray instrument, 2, a61," *Journal of large-scale research facilities JLSRF*, vol. 2, no. A61, 2016.

[72] P. Schöffmann, *Stoichiometric control and magnetoelectric coupling in artificial multiferroic heterostructures*. PhD thesis, RWTH Aachen University, 2021.

[73] L. Chaurette, N. Cheng, and B. Stuart, "Atomic force microscopy," 2016.

[74] R. Proksch, A. Research, and S. Kalinin, "Piezoresponse force microscopy with asylum research afms,"

[75] M. McElfresh, "Fundamentals of magnetism and magnetic measurements featuring quantum design's magnetic property measurement system.," *Quantum Design*, 1994.

[76] P. Borisov, A. Hochstrat, V. V. Shvartsman, and W. Kleemann, "Superconducting quantum interference device setup for magnetoelectric measurements," *Review of Scientific Instruments*, vol. 78, no. 10, p. 106105, 2007.

[77] M. Mayer, "Rutherford backscattering spectrometry (rbs)," *Lectures given at the workshop on Nuclear data for science and technology: Material analysis.*, 2003.

[78] L. R. Doolittle, "Algorithms for the rapid simulation of rutherford backscattering spectra," *Nuclear Instruments and Methods in Physics*

Research Section B: Beam Interactions with Materials and Atoms, vol. 9, no. 3, pp. 344 – 351, 1985.

[79] Ernst Ruska-Centre for Microscopy and Spectroscopy with Electrons (ER-C) et al., "Fei titan g2 80-200 crewley," *Journal of large-scale research facilities*, vol. 2, no. A43, 2016.

[80] "https://www.nist.gov/ncnr/polarized-beam-reflectometer-pbr; accessed on 26.11.20."

[81] T. Bhatnagar-Schöffmann, E. Kentzinger, A. Sarkar, P. Schöffmann, Q. Lan, L. Jin, A. Kovács, A. J. Grutter, B. J. Kirby, R. Beerwerth, M. Waschk, A. Stellhorn, U. Rücker, R. E. Dunin-Borkowski, and T. Brückel, "Differentiation between strain and charge mediated magnetoelectric coupling in $La_{0.7}Sr_{0.3}MnO_3/Pb(Mg_{1/3}Nb_{2/3})_{0.7}Ti_{0.3}O_3(001)$," *New Journal of Physics*, vol. 23, no. 6, p. 063043, 2021.

[82] A. Steffen, *Self-purifying $La_{2/3}Sr_{1/3}MO_3$ epitaxial films: Observation of surface precipitation of Mn_3O_4 particles for excess of Mn ratios.* PhD thesis, RWTH Aachen, 2016.

[83] A. Miniotas, A. Vailionis, E. B. Svedberg, and U. O. Karlsson, "Misfit strain induced lattice distortions in heteroepitaxially grown $La_xCa_{1-x}MnO_3$ thin films studied by extended x-ray absorption fine structure and high-resolution x-ray diffraction," *Journal of Applied Physics*, vol. 89, no. 4, pp. 2134–2137, 2001.

[84] T. A. Miller, R. W. Chhajlany, L. Tagliacozzo, B. Green, S. Kovalev, D. Prabhakaran, M. Lewenstein, M. Gensch, and S. Wall, "Terahertz field control of in-plane orbital order in la0.5sr1.5mno4," *Nature Communications*, vol. 6, no. 1, p. 8175, 2015.

[85] F. Li, S. Zhang, Z. Xu, X. Wei, J. Luo, and T. Shrout, "Piezoelectric activity of relaxor-pbtio3 based single crystals and polycrystalline ceramics at cryogenic temperatures: Intrinsic and extrinsic contributions," *Applied Physics Letters*, vol. 96, pp. 192903 – 192903, 06 2010.

[86] P. Wang, C. Jin, Y. C. Wang, S. S. Liu, X. Y. Wang, D. X. Zheng, W. C. Zheng, and H. L. Bai, "Differentiation of non-volatile strain and ferroelectric field effects in (011)- and (001)-$La_{0.67}Sr_{0.33}MnO_3/Pb(Mg_{1/3}Nb_{2/3})_{0.7}Ti_{0.3}O_3$ heterostructures," *Journal of Applied Physics*, vol. 127, no. 24, p. 244102, 2020.

[87] D. Li, D. Zheng, J. Gong, W. Zheng, C. Jin, and H. Bai, "Self-poling-induced magnetoelectric effect in highly strained epitaxial $BiFeO_3/La_{0.67}Sr_{0.33}MnO_{3-\delta}$ multiferroic heterostructures," *ACS Applied Materials & Interfaces*, vol. 9, no. 28, pp. 24331–24338, 2017. PMID: 28649827.

[88] E. M. Sabolsky, S. Trolier-McKinstry, and G. L. Messing, "Dielectric and piezoelectric properties of ⟨001⟩ fiber-textured $0.675Pb(Mg_{1/3}Nb_{2/3})O_3$–$0.325PbTiO_3$ ceramics," *Journal of Applied Physics*, vol. 93, no. 7, pp. 4072–4080, 2003.

[89] T. Wu, P. Zhao, M. Bao, A. Bur, J. L. Hockel, K. Wong, K. P. Mohanchandra, C. S. Lynch, and G. P. Carman, "Domain engineered switchable strain states in ferroelectric (011) $[Pb(Mg_{1/3}Nb_{2/3})O_3]_{(1-x)}$-$[PbTiO_3]_x$ (PMN-PT, x≈0.32) single crystals," *Journal of Applied Physics*, vol. 109, no. 12, p. 124101, 2011.

[90] Q. Guo, X. Xu, F. Wang, Y. Lu, J. Chen, Y. Wu, K. Meng, Y. Wu, J. Miao, and Y. Jiang, "In-plane electric field controlled ferromagnetism and anisotropic magnetoresistance in an LSMO/PMN-PT heterostructure," *Nanotechnology*, vol. 29, p. 224003, apr 2018.

[91] K. Steenbeck and R. Hiergeist, "Magnetic anisotropy of ferromagnetic $La_{0.7}$ (Sr, Ca)$_{0.3}MnO_3$ epitaxial films," *Applied Physics Letters*, vol. 75, no. 12, pp. 1778–1780, 1999.

[92] S. K. Chaluvadi, F. Ajejas, P. Orgiani, O. Rousseau, G. Vinai, A. Y. Petrov, P. Torelli, A. Pautrat, J. Camarero, P. Perna, and L. Mechin, "Room temperature biaxial magnetic anisotropy in $La_{0.67}Sr_{0.33}MnO_3$ thin films on srtio3 buffered mgo (001) substrates for spintronic applications," *Applied Physics Letters*, vol. 113, no. 5, p. 052403, 2018.

[93] S. Kumari, N. Mottaghi, C.-Y. Huang, R. Trappen, G. Bhandari, S. Yousefi, G. Cabrera, M. S. Seehra, and M. B. Holcomb, "Effects of oxygen modification on the structural and magnetic properties of highly epitaxial$La_{0.7}Sr_{0.3}MnO_3$ (LSMO) thin films," *Scientific Reports*, vol. 10, no. 1, p. 3659, 2020.

[94] N. Mottaghi, R. B. Trappen, S. Kumari, C.-Y. Huang, S. Yousefi, G. B. Cabrera, M. Aziziha, A. Haertter, M. B. Johnson, M. S. Seehra, and M. B. Holcomb, "Observation and interpretation of negative remanent magnetization and inverted hysteresis loops in a thin film of $La_{0.7}Sr_{0.3}MnO_3$," *Journal of Physics: Condensed Matter*, vol. 30, p. 405804, sep 2018.

[95] B. Boucher, R. Buhl, and M. Perrin, "Magnetic structure of Mn_3O_4 by neutron diffraction," *Journal of Applied Physics*, vol. 42, no. 4, pp. 1615–1617, 1971.

[96] E. J. Moon, P. V. Balachandran, B. J. Kirby, D. J. Keavney, R. J. Sichel-Tissot, C. M. Schlepütz, E. Karapetrova, X. M. Cheng, J. M. Rondinelli, and S. J. May, "Effect of interfacial octahedral behavior in ultrathin manganite films," *Nano Letters*, vol. 14, no. 5, pp. 2509–2514, 2014. PMID: 24697503.

[97] A. Tebano, C. Aruta, S. Sanna, P. G. Medaglia, G. Balestrino, A. A.

Sidorenko, R. De Renzi, G. Ghiringhelli, L. Braicovich, V. Bisogni, and N. B. Brookes, "Evidence of orbital reconstruction at interfaces in ultrathin $La_{0.67}Sr_{0.33}MnO_3$ films," *Phys. Rev. Lett.*, vol. 100, p. 137401, Apr 2008.

[98] M. Huijben, L. W. Martin, Y.-H. Chu, M. B. Holcomb, P. Yu, G. Rijnders, D. H. A. Blank, and R. Ramesh, "Critical thickness and orbital ordering in ultrathin $La_{0.7}Sr_{0.3}MnO_3$ films," *Phys. Rev. B*, vol. 78, p. 094413, Sep 2008.

[99] P. A. Kienzle, B. B. Maranville, K. V. O'Donovan, J. F. Ankner, N. F. Berk, and C. F. Majkrzak *NCNR,NIST*, 2017.

[100] G. Pospelov, W. Van Herck, J. Burle, J. M. Carmona Loaiza, C. Durniak, J. M. Fisher, M. Ganeva, D. Yurov, and J. Wuttke, "*BornAgain* : software for simulating and fitting grazing-incidence small-angle scattering," *Journal of Applied Crystallography*, vol. 53, pp. 262–276, Feb 2020.

[101] D. Mukherjee, N. Bingham, M. Hordagoda, M.-H. Phan, H. Srikanth, S. Witanachchi, and P. Mukherjee, "Influence of microstructure and interfacial strain on the magnetic properties of epitaxial $Mn_3O_4/La_{0.7}Sr_{0.3}MnO_3$ layered-composite thin films," *Journal of Applied Physics*, vol. 112, no. 8, p. 083910, 2012.

[102] J. Pattanayak, S. R. V, and H. S. Maiti, "Electrical resistivity measurements on the Mn_2O_3-Mn_3O_4 phase transformation.," *J Mater Sci Lett*, vol. 8, pp. 1405–1407, 1989.

[103] T. Suzuki and T. Katsufuji, "Magnetodielectric properties of spin-orbital coupled system Mn_3O_4," *Phys. Rev. B*, vol. 77, p. 220402, Jun 2008.

[104] Z. Bi, E. Weal, H. Luo, A. Chen, J. L. MacManus-Driscoll, Q. Jia, and H. Wang, "Microstructural and magnetic properties of $(La_{0.7}Sr_{0.3}MnO_3)_{0.7}$:$(Mn_3O_4)_{0.3}$ nanocomposite thin films," *Journal of Applied Physics*, vol. 109, no. 5, p. 054302, 2011.

[105] A. Pomar, Z. Konstantinović, N. Bagués, J. Roqueta, L. López-Mir, L. Balcells, C. Frontera, N. Mestres, A. Gutiérrez-Llorente, M. Šćepanović, N. Lazarević, Z. V. Popović, F. Sandiumenge, B. Martínez, and J. Santiso, "Formation of self-organized Mn_3O_4 nanoinclusions in $LaMnO_3$ films," *Frontiers in Physics*, vol. 4, p. 41, 2016.

[106] H. Jian, Z. Zhang, Y. Wang, X. Tang, J. Yang, L. Hu, L. Chen, X. Zhu, and Y. Sun, "Preparation of $La_{0.7}Sr_{0.3}Mn_1{+}xO_y$ ($1{\leq}x{\leq}4$) thin films by chemical solution deposition: Dual epitaxy and possible spinodal growth," *Journal of Alloys and Compounds*, vol. 561, pp. 95 – 100, 2013.

[107] C. Boothroyd and A. Kovacs, "FEI Titan 80-300 TEM," *Journal of large-scale research facilities*, vol. A41, p. 2, 2016.

[108] M. McCarteney and D. J. Smith, "Electron holography and lorentz

microscopy of magnetic thin films and multilayers," *Scanning Microscopy*, vol. 11, pp. 335–344, 1997.

[109] F. AU Zheng, A. AU Kovács, T. AU Denneulin, J. AU Caron, T. AU Weßels, and R. E. AU Dunin-Borkowski, "Magnetic field mapping using off-axis electron holography in the transmission electron microscope," *JoVE*, no. 166, p. e61907, 2020.

[110] J. D. Burton and E. Y. Tsymbal, "Prediction of electrically induced magnetic reconstruction at the manganite/ferroelectric interface," *Phys. Rev. B*, vol. 80, p. 174406, Nov 2009.

[111] M. Schmitz, A. Weber, O. Petracic, M. Waschk, P. Zakalek, S. Mattauch, A. Koutsioubas, and T. Brückel, "Strain and electric field control of magnetism in $La_{(1-x)}Sr_x$ MnO_3 thin films on ferroelectric $BaTiO_3$ substrates," *New Journal of Physics*, vol. 22, p. 053018, may 2020.

[112] K. J. Choi, M. Biegalski, Y. L. Li, A. Sharan, J. Schubert, R. Uecker, P. Reiche, Y. B. Chen, X. Q. Pan, V. Gopalan, L.-Q. Chen, D. G. Schlom, and C. B. Eom, "Enhancement of ferroelectricity in strained $BaTiO_3$ thin films," *Science*, vol. 306, no. 5698, pp. 1005–1009, 2004.

[113] "https://www.jpk.com/app-technotes-img/afm/pdf/jpk-tech-piezoresponse-force-microscopy.14-1.pdf.." [Online; accessed on 11.03.2021].

[114] Z. Guan, Z.-Z. Jiang, B.-B. Tian, Y.-P. Zhu, P.-H. Xiang, N. Zhong, C.-G. Duan, and J.-H. Chu, "Identifying intrinsic ferroelectricity of thin film with piezoresponse force microscopy," *AIP Advances*, vol. 7, no. 9, p. 095116, 2017.

List of Figures

List of Tables

Band / Volume 238
Single-Trap Phenomena in Nanowire Biosensors
Y. Kutovyi (2021), 171 pp
ISBN: 978-3-95806-544-4

Band / Volume 239
Single crystal growth and neutron scattering studies of novel quantum materials
X. Wang (2021), VI, 145 pp
ISBN: 978-3-95806-546-8

Band / Volume 240
Structure and Dynamics of Magnetocaloric Materials
N. A. Maraytta (2021), vii, 146 pp
ISBN: 978-3-95806-557-4

Band / Volume 241
Novel insights into the transcriptional regulation of cell division in *Corynebacterium glutamicum*
K. J. Kraxner (2021), V, 83 pp
ISBN: 978-3-95806-560-4

Band / Volume 242
Interplay of proximity effects in superconductor/ferromagnet heterostructures
A. Stellhorn (2021), ix, 219 pp
ISBN: 978-3-95806-562-8

Band / Volume 243
Silencing and counter-silencing of the Lsr2-like protein CgpS in *Corynebacterium glutamicum*
J. Wiechert (2021), IV, 265 pp
ISBN: 978-3-95806-569-7

Band / Volume 244
Molecular Layer Functionalized Neuroelectronic Interfaces:
From Sub-Nanometer Molecular Surface Functionalization to Improved Mechanical and Electronic Cell-Chip Coupling
N. R. Wolf (2021), IV, 101, xx pp
ISBN: 978-3-95806-570-3

Band / Volume 245
Surface Acoustic Waves in Strain-Engineered Thin (K,Na)NbO_3 Films:
From Basic Research to Application in Molecular Sensing
S. Liang (2021), VI, 125 pp
ISBN: 978-3-95806-571-0

Band / Volume 246
Tailoring neuroelectronic interfaces via combinations of oxides and molecular layers
X. Yuan (2021), 113 pp
ISBN: 978-3-95806-572-7

Band / Volume 247
Stoichiometric control and magnetoelectric coupling in artificial multiferroic heterostructures
P. Schöffmann (2021), vii, 176 pp
ISBN: 978-3-95806-575-8

Band / Volume 248
A Unified Framework for Functional Renormalisation Group Calculations and its Application to Three Dimensional Hubbard Models
J. Ehrlich (2021), xvi, 213 pp
ISBN: 978-3-95806-582-6

Band / Volume 249
Photoemission electron microscopy of magneto-ionic effects in $La_{0.7}Sr_{0.3}MnO_3$
M. Wilhelm (2021), 134 pp
ISBN: 978-3-95806-592-5

Band / Volume 250
Development of a Multiplexer System and Measurement of the Neutron Yield for a Low-Energy Accelerator-Driven Neutron Source
M. Rimmler (2021), v, 200 pp
ISBN: 978-3-95806-600-7

Band / Volume 251
Resolving interface effects in voltage controlled magnetic heterostructures using advanced neutron scattering and electron microscopy methods
T. Bhatnagar-Schöffmann (2021), ix, 171 pp
ISBN: 978-3-95806-604-5

Schlüsseltechnologien / Key Technologies
Band / Volume 251
ISBN 978-3-95806-604-5

Mitglied der Helmholtz-Gemeinschaft

JÜLICH
Forschungszentrum